Check for updates

Recent advances in two-dimensional nanomaterials for photocatalytic reduction of CO_2: insights into performance, theories and perspective

Deyu Qin,[ab] Yin Zhou,[ab] Wenjun Wang, [iD][ab] Chen Zhang, [iD] *[ab] Guangming Zeng, [iD] *[ab] Danlian Huang, [iD][ab] Longlu Wang, [iD][c] Han Wang, [iD][ab] Yang Yang,[ab] Lei Lei, [iD][ab] Sha Chen[ab] and Donghui He[ab]

Global warming and energy shortage are two major stumbling blocks on the road of human social progress, and have gradually aroused a sense of crisis. Artificial photosynthesis is a two-pronged solution to both problems. However, due to the harsh reaction conditions and low efficiency, traditional semiconductors cannot achieve this. Two-dimensional (2D) materials with larger specific surface areas, lower carrier migration distances, more active surface atoms, and higher elastic strain tolerance play a critical role in the solar to chemical energy conversion scheme, and provide a novel methodology for the synthesis of fine chemicals. This review details the principles of photocatalytic reduction of CO_2, and highlights the reduction pathways and product selectivity *via* experimental methods and theoretical calculations. The state-of-the-art achievements of 2D materials in the field of photocatalytic reduction of CO_2 are summarized, mainly including material structure, characteristics, and modification strategies to improve the performance of CO_2 reduction. And the research on the combination of 2D materials and single atoms is emphasized. Moreover, bottlenecks and challenges in the design and application of 2D materials, as well as prospects of the future development direction, will be highlighted in order to seek new breakthroughs by exploring new materials design solutions.

1. Introduction

Global warming has plagued humans for many years, and CO_2, as the main greenhouse gas, is the main factor leading to global

warming. In February 2019, the concentration of CO_2 in the atmosphere was 410.6 PPM (parts per million). According to the Intergovernmental Panel on Climate Change (IPCC), the concentration of CO_2 will reach 590 PPM by the end of the 21st

[a]College of Environmental Science and Engineering, Hunan University, Changsha 410082, P. R. China. E-mail: zhangchen@hnu.edu.cn; zgming@hnu.edu.cn

[b]Key Laboratory of Environmental Biology and Pollution Control (Hunan University), Ministry of Education, Changsha 410082, P. R. China

[c]College of Electronic and Optical Engineering & College of Microelectronics, Nanjing University of Posts and Telecommunications, Nanjing, 210023, P. R. China
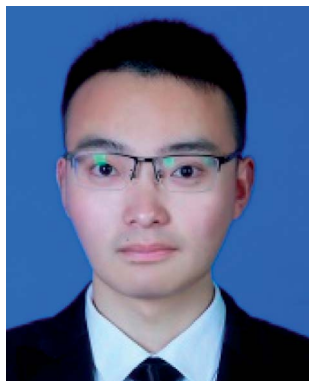
Deyu Qin received his B.S. in environmental engineering from the Anhui University of Technology in 2019. He is currently a postgraduate student under the supervision of Chen Zhang at the College of Environmental Science and Engineering, Hunan University, China. His current research includes fabrication of nano materials and their catalysis applications in energy and environment.

Chen Zhang is currently an associate professor of Environmental Science and Engineering at Hunan University. He obtained his PhD in Environmental Engineering from Hunan University in 2017. The research interests of his group include fabrication of nano materials and their catalysis applications in energy and environment, and thermo-chemical conversion of biomass into clean energy and value-added chemicals.

century, and the temperature of the earth will rise by 1.9 °C.[1] The main source of CO_2 gas in the earth is the combustion of fossil fuels, which accounts for 40% of the total anthropogenic carbon emissions.[2–4] Developing new energy technologies is conducive to the vigorous development of optimization tools for energy and pollution issues, such as wind energy, hydropower, and nuclear energy, but these new energy sources presently cannot fully replace fossil fuels. Hence, the reduction of CO_2 into valuable fuels and chemicals will be a multiple efficacy approach for dealing with the energy crunch and mitigating the greenhouse effect.[5,6]

In nature, the way of CO_2 conversion is mainly plant photosynthesis. There are also some researches on the artificial reduction of CO_2, among which the research methods mainly include biological, electrochemical, and photocatalytic methods.[7–11] Artificial photosynthesis and photocatalysis has been paid wide spread attention in recent years with the ideal concept of harvesting and storing sustainable solar energy and mimicking the natural photosynthetic process.[12] On the one hand, photocatalysis is highly efficient and can reduce CO_2 to various products, including C_1 (CO, CH_3OH, HCOOH, CH_4, etc.), C_2 (C_2H_4, CH_3CH_2OH, CH_3CHO, etc.), and a small amount of C_3 (CH_3CH_2CHO, $CH_3CH_2CH_2OH$, etc.) products. On the other hand, photocatalysis is a low energy consumption process, and light energy is inexhaustible.[13] Except for photocatalytic materials, there is almost no secondary pollution to the environment.[14,15] The selection of photocatalyst is the core subject in the field of photocatalysis, which directly determines the photocatalytic performance. In the process of photocatalytic reduction of CO_2, different photocatalytic species have different photoexcitation capabilities, which will lead to different reduction product yield and selectivity. In 1979, Inoue and co-workers used semiconductors WO_3, TiO_2, ZnO, CdS, GaP, and SiC powders to photoelectrocatalytic reduction of CO_2 to form organic matter for the first time.[16] Since then, various photocatalysts are used in the study of CO_2 reduction. TiO_2 has been a major research object for a long time, and various methods have been used to make up for the inherent energy band structure and photoelectric performance defects of TiO_2 materials.[17–19] With further research, many new materials have begun to emerge in the field of photocatalysis, such as Ag_3PO_4, CdS,

ZnO, etc.[20–23] But it is worth noting that there is no perfect photocatalyst, the photocatalytic activity may be limited by poor visible light utilization, low specific surface area, carrier recombination and low photocatalytic efficiency.

In 2004, with the successful separation of graphene by Novoselov and Geim, the application of 2D materials attracted widespread attention.[24] Through the analysis of data from Web of Science, there is a rapid growth of publications on the research of 2D materials in the field of photocatalytic reduction of CO_2 (Fig. 1). The 2D materials are defined as a free-form crystal with a plane size of more than 100 nm and a thickness of only one or a few atomic layers.[25] 2D materials have a large specific surface area, which provide many active sites.[26] In addition, the ultrathin thickness of 2D materials reduces the distance that photogenerated carriers reach the surface of the material, thereby greatly inhibiting the recombination of charge carriers.[27] Moreover, reducing the dimension of the material can change the energy band structure. By adjusting the positions of the conduction band (CB) and the valence band (VB), the visible light response and photocatalytic performance of the material can be improved. It is worth noting that 2D materials often have a higher elastic strain tolerance, thus, the energy band structure of materials can also be effectively adjusted by elastic strain engineering.[28] Besides, during the formation of some 2D materials, terminating groups or dangling bonds will be formed on the surface, which is conducive to the adsorption of CO_2 molecules by the material, thereby effectively improving the yield of chemical products.[29,30] Therefore, 2D materials has huge application potential in the field of photoreduction of CO_2.

Although some literature has been published in this field,[31–33] the introduction of 2D materials is not comprehensive or fails to focus on the application research of photocatalytic reduction of CO_2. At the same time, they often underestimate the introduction of CO_2 photoreduction theory and product selectivity, so the elaboration of the reduction mechanism is not thorough and complete. In addition, as an important theoretical research tool, density functional theory (DFT) deserves further elaboration, and

Guangming Zeng obtained his PhD in 1988 from Wuhan University. He has taught courses and performed research on Environmental Science and Health at Hunan University since 1988. He is one of the 2017 Highly Cited Researchers in the world issued by Clarivate Analytics. His current research interests include focus on the synthesis and application of functional nanomaterials in the environment and energy field.
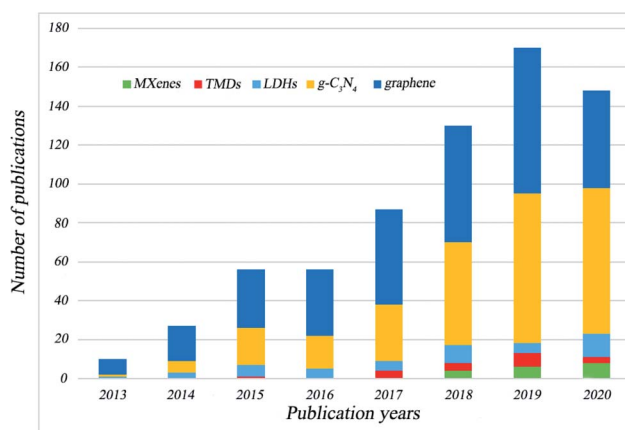
Fig. 1 Publications per year about typical 2D materials in the field of photocatalytic reduction of CO_2. The data are based on the search results from Web of Science (September, 2020).

This journal is © The Royal Society of Chemistry 2020

J. Mater. Chem. A, 2020, **8**, 19156–19195 | **19157**

this is rarely mentioned in previously published reviews. Therefore, we presented a critical review about the recent advances in 2D materials for CO_2 photoreduction and related theories. Herein, the basic principles of CO_2 photoreduction are introduced, including the basic steps of photocatalysis, the conditions required for CO_2 photocatalysis and the challenges it faces. After that, this review highlights the main pathways of CO_2 reduction, product selectivity, and DFT calculations. Then, several typical 2D materials (such as MXenes, layered double hydroxides (LDHs), transition metal dichalcogenides (TMDs), graphene, *etc.*) are summarized, including their structures, properties, and applications in CO_2 photocatalytic reduction. The research progress of 2D materials as single-atom carriers is emphasized. This review also enumerates some methods to improve the photocatalytic performance of materials, which includes elemental doping, morphology control, vacancy engineering, and heterojunction engineering. In the last part, based on its current status, the conclusions and perspectives of development in this field are introduced.

2. Basic principles of CO_2 photoreduction

The essence of CO_2 photoreduction is the energy conversion process, in which solar energy is converted into chemical energy

Fig. 2 The schematic diagram of photocatalytic reduction of CO_2 with H_2O.

by photocatalyst and stored in various photocatalytic products. This process involves three crucial steps: (i) the photocatalyst absorbs photons with energy greater than or equal to the bandgap energy, and charge carriers generate; (ii) the photogenerated carriers separate and transfer from the interior to the surface of the photocatalyst; (iii) the photogenerated electrons reduce CO_2 into value-added fuels and chemicals, and holes oxidize sacrificial reagents.[30,34] After the above three steps, the reduction products of CO_2 are desorbed from the surface of the photocatalyst to facilitate subsequent reaction (Fig. 2).

In the third step above, the reduction of CO_2 with H_2O is a very complicated process, which is generally considered to involve two mechanisms. The first mechanism involves the single electron transfer process. Single electron activates CO_2 molecules, leading to the formation of CO_2^{*-} intermediates.[35] This process requires a negative equilibrium potential of -1.9 V *versus* normal hydrogen electrode (NHE). The band structure of many semiconductor materials does not meet the requirements,[36,37] and there is not enough driving force to perform this single electron transfer process, so this process is thermodynamic unfavorable. In addition, there is large recombination energy between the linear CO_2 molecule and the CO_2^{*-} radical anion, therefore this step is generally considered to be a rate-limiting step. In addition to this mechanism, another route is a multiple proton-coupled electron transfer process that bypasses the formation of CO_2^{*-} intermediates.[16] As the number of transferred electrons and protons increases, different reduction products are formed, such as CO, HCOOH, HCHO, CH_3OH, CH_4, *etc.* (Table 1). For the formation process of multi-carbon products (CH_3CH_2OH, C_2H_6, C_2H_4, *etc.*), in addition to the supply of electrons and protons, the difficulty of C–C coupling is a more important factor restricting product yield and selectivity. In order to form multi-carbon products, stable intermediates must be guaranteed to participate in C–C coupling reactions.[38,39]

It is worth noting that in addition to the above CO_2 reduction mechanism, the situation will be different when CO_2 is reduced by H_2 and CH_4 (Table 2).[41] Through the reverse water gas shift reaction, CO_2 can be reduced to CO by H_2. There are two mechanisms involved in the conversion of CO_2 to CO. One mechanism is that hydrogen does not participate in the formation reaction of intermediates, but only acts as a reducing agent. Another mechanism is that formate acts as an
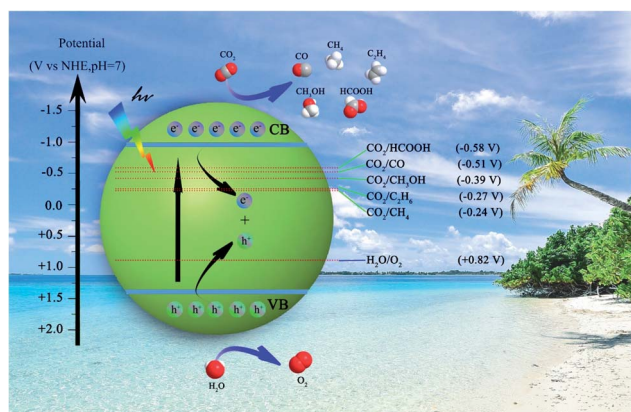
Table 1 Possible products of carbon dioxide and water reduction and the corresponding reduction potential (*versus* NHE at pH 7 in aqueous solution)[30,31,40]

Product	Reaction	E^0 (V *vs.* NHE)	Equation
Hydrogen	$2H_2O + 2e^- \rightarrow 2OH^- + H_2$	-0.41	1
Carbon monoxide	$CO_2 + 2H^+ + 2e^- \rightarrow CO + H_2O$	-0.51	2
Formic acid	$CO_2 + 2H^+ + 2e^- \rightarrow HCOOH$	-0.58	3
Oxalic acid	$2CO_2 + 2H^+ + 2e^- \rightarrow H_2C_2O_4$	-0.87	4
Methanol	$CO_2 + 6H^+ + 6e^- \rightarrow CH_3OH + H_2O$	-0.39	5
Methane	$CO_2 + 8H^+ + 8e^- \rightarrow CH_4 + 2H_2O$	-0.24	6
Ethanol	$2CO_2 + 12H^+ + 12e^- \rightarrow C_2H_5OH + 3H_2O$	-0.33	7
Ethane	$2CO_2 + 14H^+ + 14e^- \rightarrow C_2H_6 + 4H_2O$	-0.27	8

19158 | *J. Mater. Chem. A*, 2020, **8**, 19156–19195

This journal is © The Royal Society of Chemistry 2020

Table 2 The reaction process in which CO_2 is reduced by H_2 and CH_4 and the required $\Delta H_{298\ K}$ (kJ mol^{-1})[45]

Reaction	$\Delta H_{298\ K}$ (kJ mol^{-1})	Equation
$CO_2 + H_2 \rightarrow CO + H_2O$	41.2	9
$CO_2 + 4H_2 \rightarrow CH_4 + 2H_2O$	−252.9	10
$CO_2 + 3H_2 \rightarrow CH_3OH + H_2O$	−49.5	11
$CO_2 + CH_4 \rightarrow 2CO + 2H_2$	247	12

intermediate.[42] The process of converting CO_2 and H_2 into CH_4 is called the Sabatier reaction. Whether CO acts as an intermediate in this reaction determines two different reduction mechanisms. The mechanism of the hydrogenation of CO_2 to CH_3OH is similar to that of CO_2 methanation.[43] On the one hand, CO_2 can be converted to CO first, and then CO can be converted to CH_3OH. On the other hand, the entire process can also be without the participation of CO. Moreover, CH_4 and CO_2 can react to form a mixture of CO and H_2, a process known as a dry reforming of methane.[44] CH_4 is first decomposed into C and H_2, and then C and O combine to form CO.

Reducing CO_2 to valuable chemicals is a challenging process, and the challenges are mainly reflected in the yield and selectivity of the product. Firstly, the dissociation energy of C=O is higher than 750 kJ mol^{-1}, so CO_2 molecule is extremely stable in thermodynamics. The conversion of CO_2 molecules requires a large amount of energy input. Secondly, competing hydrogen evolution reaction (HER) may occur when water is used as a reducing agent, and this process will consume H$^+$ and electrons to produce H_2. It is worth noting that CO_2 has low solubility in water, so the reduction of water to H_2 is more likely to occur than the reduction of CO_2, which will greatly reduce the production of hydrocarbons. Thirdly, the carbon atom in CO_2 is at the highest oxidation state, therefore, various products are formed during the CO_2 reduction process. Thermodynamically, CO_2 tends to be reduced to methanol and methane due to less potential energy required, in terms of kinetics, CO_2 is more inclined to be reduced to CO and formic acid due to the lower number of electrons required.[46–48]

In order to effectively carry out the reduction of CO_2, the following conditions must be satisfied. Photocatalyst must have appropriate band structure. On the one hand, band position of the photocatalyst needs to match the potential required for CO_2 reduction. The CB edge potential is more negative than the reduction potential required for CO_2 reduction, and the VB edge potential is more positive than the oxidation potential of reducing agent. On the other hand, wider bandgap tends to imply a lower visible light absorption range. Thus, the bandgap should be as close as possible to the potential required for the redox reaction. For the photocatalytic reduction of carbon dioxide, the ideal band gap of a photocatalyst is 1.75–3.0 eV.[32] The large amount of CO_2 adsorption on the material is the basis for achieving excellent photocatalytic reduction performance. When enough CO_2 molecules are adsorbed on the surface of the photocatalyst, photogenerated electrons and CO_2 can be combined quickly to reduce the recombination of carriers, thus obtaining a higher yield. The surface area and surface energy of

materials are important factors affecting the adsorption of CO_2 molecules. A larger surface area can provide more adsorption sites and accommodate more CO_2 molecules. The surface energy of the material can be changed by adjusting the chemical properties of the surface or exposing the high-energy facets.[34] In addition, photogenerated electrons and holes should be rapidly transferred to the surface of the material, thus reducing the recombination rate. Photogenerated electrons and holes can recombine in just 10^{-9} s, whereas redox reaction time is generally between 10^{-8} s and 10^{-3} s,[49] so it is necessary to take appropriate measures to reduce carrier recombination. Finally, the reduced products should be easily desorbed from the photocatalyst to facilitate subsequent adsorption of the reactants. On the one hand, the products occupy the adsorption space of the reactants, and on the other hand, the products adsorbed on the surface may undergo side reactions.

After a series of reaction conditions are suitable, CO_2 molecules will undergo a complex reduction process under the catalysis of the photocatalyst. During the reduction process, different products, by-products and intermediates will be generated. Therefore, exploring the reduction pathways of CO_2 is of great significance to control the yield and selectivity of the target product.

3. Possible reaction pathways and product selectivity

3.1 CO_2 adsorption modes

The adsorption and activation of CO_2 molecules are the core steps in the whole reduction process. The adsorption of CO_2 molecules on the photocatalyst surface is an essential initial step in this process. As a linear molecule, CO_2 can be physiosorbed on the photocatalyst surface, but in the subsequent activation process, the chemical adsorption of CO_2 molecules is more important.[30] There are three main coordination modes of CO_2 molecules on the surface of photocatalyst. Firstly, the O atom in the CO_2 molecule serves as an electron donor, and provides
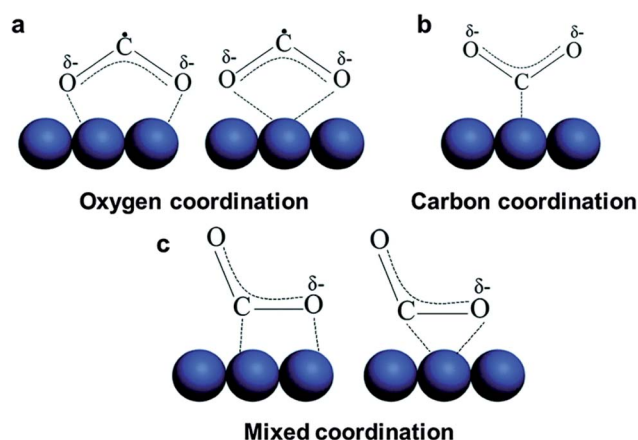

Fig. 3 Schematic diagram reflects three different coordination modes of CO_2 molecule. Reproduced with permission from ref. 30. Copyright 2016 Royal Society of Chemistry.

This journal is © The Royal Society of Chemistry 2020

J. Mater. Chem. A, 2020, **8**, 19156–19195 | **19159**

a lone pair electron to the surface Lewis acid center. This method is called oxygen coordination, and there are two different bidentate bonding structures (Fig. 3a). Secondly, the C atom acts as an electron acceptor. When the Lewis acid takes electrons from the Lewis base center, it forms something like carbonic acid. This method is called carbon coordination (Fig. 3b). Thirdly, the O and C atoms in the CO_2 molecule receive and supply electrons at the same time, which is called mixed coordination. This coordination also has two different bidentate bonding structures (Fig. 3c).[50] It is worth noting that different coordination modes will affect the formation of certain intermediates during the reduction process, resulting in different reduction pathways. For example, it is well known that oxygen coordination tends to form $HCOO^-$, while carbon coordination is beneficial to the formation of carboxy intermediates (*COOH),[51] which affects the selectivity of the products.

3.2 Reaction pathways

3.2.1 Formation of C_1 products. The formation of $HCOO^-$ and HCOOH mainly involves three different pathways. In the first path, CO_2 is inserted into a metal–hydrogen bond or protonated by H^+ to form an intermediate. Then, the O atoms in the intermediate and the photocatalyst are connected by monodentate or bidentate, and HCOOH is formed by proton–electron transfer (Fig. 4a). The second path involves a CO_2^{*-} radical, which can form $HCOO^-$ through O coordination and C coordination with the participation of HCO_3^-.[52] In addition, *COOH intermediates will lead to the formation of HCOOH (Fig. 4b).[53] Baruch *et al.*[54,55] discovered the third path of CO_2 reduction by studying the mechanism of CO_2 reduction by Tin electrode. The CO_2 molecule will initially react with Sn^{II} oxyhydroxide to form surface-bound carbonate, and then surface-bound carbonate will form $HCOO^-$ through the transfer of two electrons and one proton (Fig. 4c).

CO formation involves an important *COOH intermediate. This intermediate generates *CO through H^+/e^- transfer. Then,

CO* is desorbed from the surface of the material. The formation of *COOH has two different paths. One of the paths is that the adsorbed CO_2 molecules generate *COOH through simple H^+/e^- transfer. In this process, because the COOH binding is weak, it is not conducive to the direct conversion of CO_2 molecules to *COOH, so there is a second path. The CO_2 molecule is converted into CO_2^{*-} radical by the reduction of single electron, and CO_2^{*-} radical receives another proton to form a *COOH intermediate (Fig. 4d).[53,55,56]

There are many formation pathways of HCHO, CH_3OH, and CH_4. In the entire reduction route, HCHO and CH_3OH can be intermediates of the final product, and can also be directly desorbed as products, so the role of CH_3OH and HCHO directly affects the formation of CH_4. The first path originates from *CO intermediates. The *HCO, *H_2CO, and *H_3CO intermediates are gradually formed through the continuous hydrogenation of *CO intermediates. The strength of the binding mode of HCHO and CH_3OH determines whether the intermediate product will desorb. If the binding mode of HCHO and CH_3OH is weak, it will lead to the formation of HCHO and CH_3OH. Conversely, CH_4 is formed by further hydrogenation of *H_3CO (Fig. 5a).[57] The second path is to convert *CO intermediate into *COH intermediate, then the combination of *COH with couple of electron and proton generates important *C intermediates. As the core special in this path, *C is gradually hydrogenated to generate *CH, *CH_2, and *CH_3. Finally, *CH_3 can be combined with ·OH or H^+ to generate CH_3OH or CH_4, respectively. The selectivity of CH_3OH and CH_4 depends on the oxophilicity of the surface (Fig. 5b).[56] The third path is clearly different from the above two paths. This path starts with CO_2^{*-} special. The CO_2^{*-} combines with couple of electron and proton to generate a bidentate coordinated HCO_2^* intermediate. H_2OCO^* and *CHO are gradually produced by hydrogenation or reduction. After that, the *CHO intermediate is converted to glyoxal through the dimerization process, and the glyoxal can be further hydrogenated to generate CH_2OHCHO and CH_3CHO. As
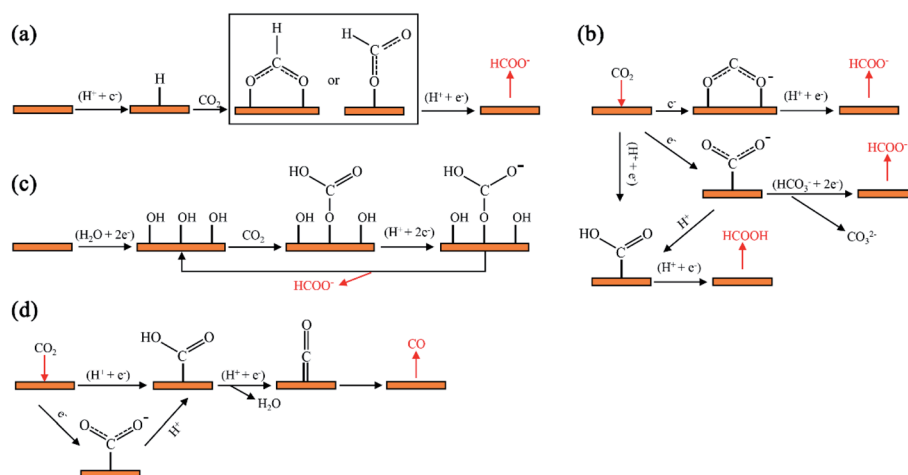

Fig. 4 (a)–(c) Possible reduction pathways for HCOOH and $HCOO^-$ formation. Reproduced with permission from ref. 53, copyright 2015 American Chemical Society. (d) Possible reduction pathways for CO formation. Reproduced with permission from ref. 54, copyright 2015 American Chemical Society.
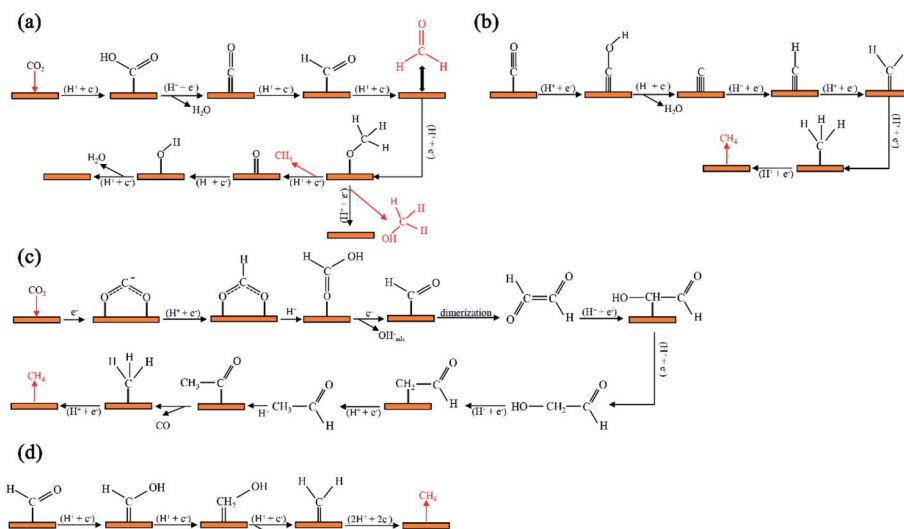
19160 | *J. Mater. Chem. A*, 2020, **8**, 19156–19195

This journal is © The Royal Society of Chemistry 2020

Fig. 5 Possible reduction pathways for HCHO, CH_3OH, and CH_4 formation. Reproduced with permission from ref. 57, copyright 2010 Royal Society of Chemistry; reproduced with permission from ref. 56, copyright 2013 Wiley-VCH; reproduced with permission from ref. 58, copyright 2013 Wiley-VCH; reproduced with permission from ref. 59, copyright 2019 American Chemical Society.

the subsequent reaction proceeds, the *CH_3 intermediate is formed, which is then converted to CH_4 by electron–proton transfer (Fig. 5c).[50,58] Recently, Ju and co-workers studied Fe–N–C single-site catalysts for electrochemical reduction of CO_2, and the results showed that the reduction pathway is different from

the above three. This path is special because the *CHO intermediate can generate *CH_2OH through two-step electron–proton transfer. On the one hand, *CH_2OH can continue to combine with the couple of electron and proton, thus releasing H_2O molecules to generate *CH_2, and then CH_4 is generated by
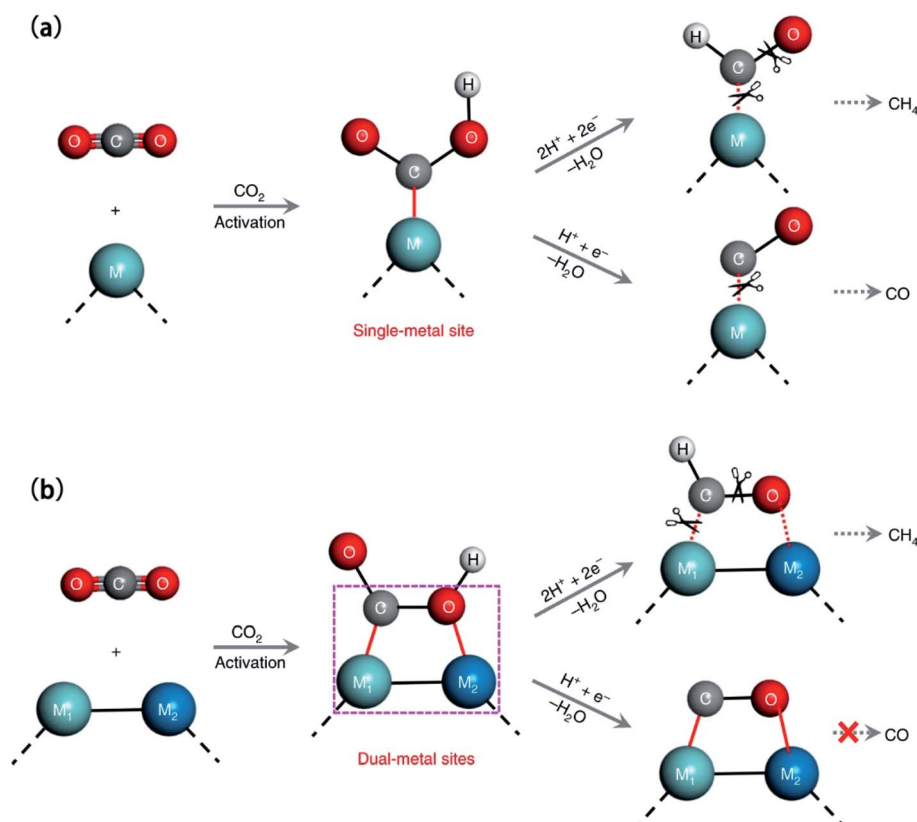

Fig. 6 A reaction mechanism of photocatalytic CO_2 reduction on (a) single metal site, and (b) dual-metal sites. Reproduced with permission from ref. 60. Copyright 2019 Springer Nature.

two-step electron–proton transfer. On the other hand, the *CH_2OH intermediate can also be directly hydrogenated and desorbed to form CH_3OH (Fig. 5d).[59]

In addition to the C_1 pathway described above, there is a new concept called dual-metal site. Dual-metal site photocatalyst has distinctive CO_2 coordination mode. Recently, Li and co-workers introduced S vacancies in 2D $CuIn_5S_8$ layers (Vs-$CuIn_5S_8$) for photocatalytic reduction of CO_2.[60] For $CuIn_5S_8$ without S vacancies, compared with C–O bonds, M–C and M–O bonds were weaker and more prone to break, resulting in the formation of CO and CH_4 after protonation (Fig. 6a). But when the S vacancies was introduced, the S vacancies on the surface of $CuIn_5S_8$ caused low coordination environment and electron accumulation around Cu and In metal atoms. The C and O atoms in the CO_2 molecule were bonded to two metal sites respectively, and forming a stable M–C–O–M intermediate. At this time, the M–C and M–O bonds were more difficult to break, and the C atom tended to be protonated, which caused the C atom to be saturated. Subsequently, the C–O and C–M bonds in the M–CH_3–O–M intermediate became weaker and fractured, leading to the formation of CH_4 (Fig. 6b). The selectivity of CH_4 was close to 100%.

3.2.2 Formation of C_2 products. The reduction path of C_2 products is more complicated. Common C_2 products mainly include ethanol, acetaldehyde, ethylene, acetic acid, and acetate. Garza et al.[61] reported the formation pathway of C_2 products on Cu surface. In this route, *CO is first converted into *CHO and *COCHO, where *COCHO plays a pivotal role in the entire reduction route and determines whether the subsequent reaction follows the ethanol route or the ethylene route. In the ethanol path, it can gradually hydrogenate and generate glyoxal, ethylene glycol, acetaldehyde, and ethanol along the way. In the ethylene pathway, in addition to the final formation of ethylene, the isomerization of the *OCH_2COH intermediate will also lead to the formation of acetic acid (Fig. 7a). Yoshio Hori et al.[62] summarized another reduction pathway for C_2 products. The C* was converted to *CH by electron–proton transfer. After the two CH_2* were coupled, C_2H_4 was formed by dimerization, or C_2H_4 was generated by CO insertion of *CH_2 (Fig. 7b). In addition, Yang et al.[247] discovered that the *$C_2O_2^-$ intermediates were formed in two different coordination modes during the C_2 reduction process, which were converted to *COCOH by hydrogenation, then converted to ethylene or acetaldehyde by the transfer of five H^+/e^-, and converted to ethanol by the transfer of seven H^+/e^- (Fig. 7c).[55,63]

3.2.3 Formation of C_3 products. The production of C_3 products is more difficult than that of C_1 and C_2 products, so the research on the reduction mechanism of C_3 products is relatively less. Yoshio Hori's research found that C–C coupling between C_2 intermediates and C_1 intermediates would lead to the formation of C_3 products.[62] For example, CH_3CH* and *CO combine to form CH_3CH_2CO* intermediates, and then through electron–proton transfer to form CH_3CH_2CHO and $CH_3CH_2CH_2OH$ (Fig. 8).[55,62]

3.3 Product selectivity

The selectivity of products has always been a hot issue in the field of CO_2 photoreduction. By effectively controlling the selectivity of the reduction product, the yield of the target

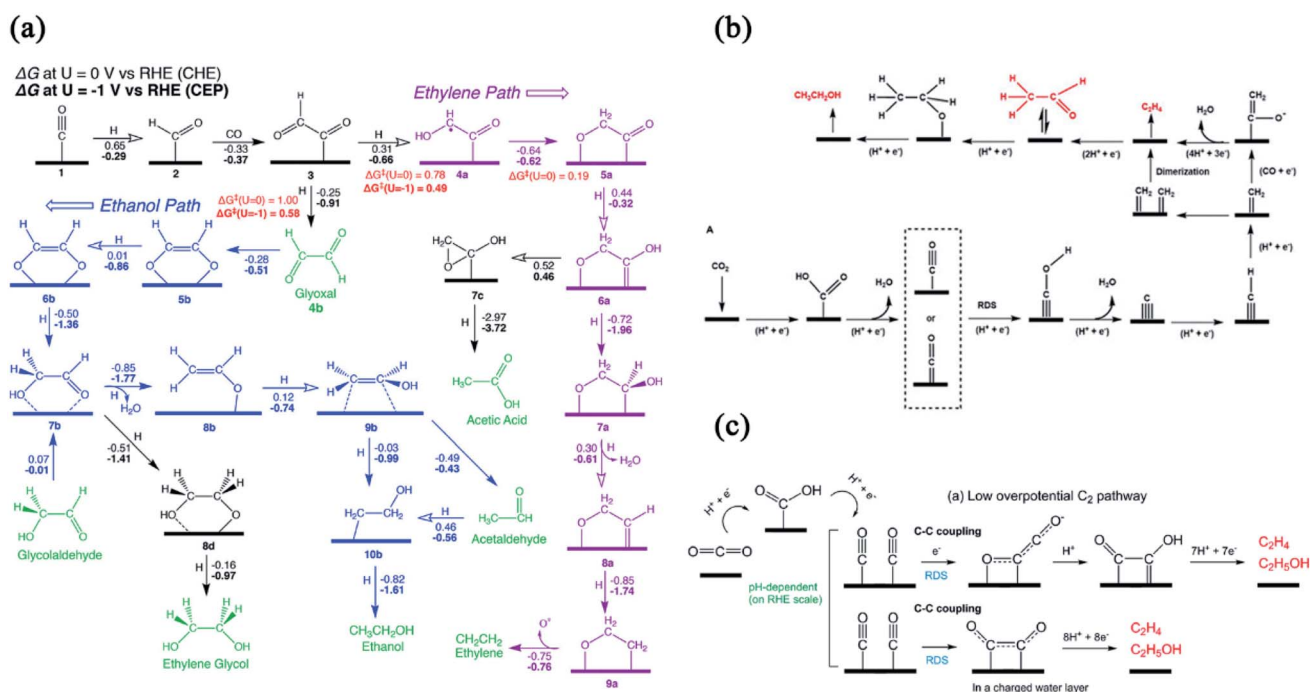**Fig. 7** Possible reduction pathways for C_2 products formation. Reproduced with permission from ref. 61, copyright 2018 American Chemical Society; reproduced with permission from ref. 55, copyright 2017 Elsevier; reproduced with permission from ref. 63, copyright 2017 American Chemical Society.
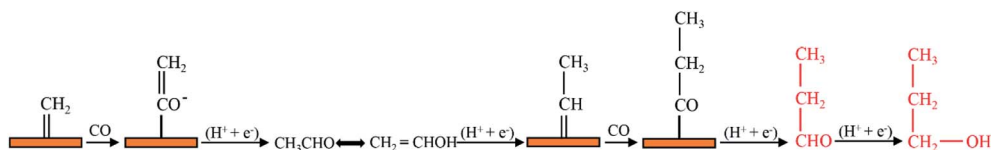
19162 | J. Mater. Chem. A, 2020, **8**, 19156–19195

This journal is © The Royal Society of Chemistry 2020

Fig. 8 Possible reduction pathways for CH_3CH_2CHO and $CH_3CH_2CH_2OH$ products formation. Reproduced with permission from ref. 62. Copyright 1997 American Chemical Society.

product can be greatly increased, so it has the vital practical significance.[64] The selectivity of the product can be controlled from the following aspects: photoexcitation process, energy band structure of photocatalyst, supply of electrons and protons, mass transfer of CO_2, and reduction reaction.

3.3.1 Photoexcitation process. For conventional semi-conductor photocatalysts, the process of generating electrons by photoexcitation is closely related to the inherent band structure of the material. Certain semiconductor materials will only be sensitive to incident light in a certain wavelength region. Therefore, it is difficult for semiconductor photocatalysts to achieve high selectivity of CO_2 photoreduction from the perspective of incident light. But the plasmonic nanoparticle photocatalyst changed this situation. Plasmonic nanoparticle photocatalysts have light excitation characteristics that are significantly different from semiconductor photocatalysts. Noble metal nanoparticles (such as Au, Ag, *etc.*) will undergo localized surface plasmon resonances (LSPR) and exhibit strong visible spectrum absorption. The electron oscillation induced by the plasmonic relaxes to produce energetic hot electrons. Such energetic electrons can activate the adsorbents on the surface of the catalyst, and the excess electrons can be used for photoreduction.[65] The plasmonic nanoparticle photocatalyst makes it more feasible to influence the product selectivity by controlling the light excitation process. For example, in Wang's study,[66] by controlling the different wavelengths and intensities of incident light, Au nanoparticles showed different selectivity for the generation of CH_4 and C_2H_6. In addition, plasmon photocatalysts often form a composite system with traditional semiconductor photocatalysts for the photoreduction of CO_2. Through the ingenious design of the composite system, the high selectivity of the product can be achieved. Zeng *et al.*[67] supported Au nanoparticles on photonic crystals composed of TiO_2 nanotubes (Au-PMTiNTs), and the CO_2 reduction products showed different selectivity under different light conditions. Under the irradiation of AM1.5G simulated sunlight, the CH_4 showed extremely high selectivity (89.3%). When the Au-PMTiNTs was illuminated by LED light ($\lambda > 420$ nm) first and then by AM1.5G light source, CO and CH_2O were the main reduction products, and CH_4 generation was not detected. The reason for this phenomenon is that semiconductors and plasmons have different light excitation properties. By reasonably controlling the wavelength of the incident light, the electron transfer inside the composite material is changed, which in turn affects the selectivity of the final product.

3.3.2 Energy band structure of photocatalyst. The band structure of the photocatalyst directly affects its redox ability. As shown in Fig. 2, the different CB positions of the photocatalyst

correspond to different reduction potentials, and different reduction potentials thermodynamically determine whether special products can be produced. Therefore, adjusting the energy band structure of the photocatalyst through an appropriate method can thermodynamically adjust the selectivity of the reduction product. Li *et al.*[68] loaded CdSe quantum dots (QDs) on 2D polymerized C_3N_4 nanosheets for highly selective CO_2 photoreduction reactions. Since the quantum confinement effect of 0D QDs can change the CB energy level of the material, the CB energy level can be at an optimal position by controlling the size of the QDs. When the particle size was 2.2 nm, the bottom of the CB (E_{CB}) was just between the potential required to generate H_2 and CH_3OH. The energy of the CB can be enough to produce CH_3OH, but not enough to produce H_2, thus effectively inhibiting the HER reaction. In addition, the energy levels required to produce CO and CH_4 were far away from E_{CB}, so CH_3OH, as the main product of CO_2 reduction, had a selectivity of 73%. In addition to the thermodynamic selectivity, the overpotential of the original material is changed by adjusting the energy level, thereby generating a greater driving force in kinetics, which is also a means to promote the selectivity of specific products. Xing *et al.*[69] used fluorination to upswept the Ti^{3+} impurity level of mesoporous single crystal TiO_{2-x}. F atoms captured electrons from Ti^{3+}, and the upward bending of Ti^{3+} impurity level increased the overpotential from 0.39 to 0.48 eV, which drove the rapid reduction of CO to CH_4, thus improving the CH_4 selectivity kinetically. The fluorination of raw materials increased the selectivity of CH_4 from 25.7% to 85.8%.

3.3.3 Supply of electrons and protons. In the process of CO_2 photoreduction, the formation of reduction products requires the constant supply of electrons and protons, and different reduction products correspond to different numbers of electrons and proton consumption. The density of electrons and protons on the surface of the catalyst will affect the selectivity of the reduction products to a certain extent. The photocatalyst will generate photogenerated electrons and holes under the irradiation of light of appropriate wavelength, and the holes will oxidize the sacrificial agent to generate protons. Therefore, promoting the separation of photogenerated electrons and holes can effectively increase the density of surface electrons and protons. There are many strategies to promote the separation of photogenerated electrons and holes, such as constructing heterojunctions,[70] loading metal elements,[71] constructing electric fields,[72] and so on. For protons, in addition to being restricted by the number of holes, they can also be supplemented in other ways. For example, Zhao *et al.*[73] introduced Cu and H atoms into the lattice of Pt and used the composite as a co-catalyst for C_3N_4. In the process of product formation, due

This journal is © The Royal Society of Chemistry 2020

J. Mater. Chem. A, 2020, **8**, 19156–19195 | **19163**

to the limited adsorption capacity of Pt atoms to H, the number of protons adsorbed by Pt was not enough to continue the conversion of CO to CH_4. However, the H in the Pt lattice diffused from the bulk to the surface of the material, and participated in the reduction reaction in the form of chemical adsorption. Sufficient proton supply makes the conversion of CO to CH_4 possible, thereby promoting the selectivity of CH_4. In addition to the number of protons, protons need to efficiently combine with CO_2 molecules to achieve high proton utilization. Only when protons bind to specific sites in the CO_2 molecule can the reduction reaction proceed along a specific reduction pathway. Wang and co-workers loaded Pt on In_2O_3 nanorods for selective CO_2 photoreduction.[74] In order to obtain CH_4 with high selectivity, the proton should bond to the C in the CO_2 molecule, not the O. In this reaction, protons first bonded with the coordinated unsaturated O on the surface of pristine In_2O_3. The C in the CO_2 molecule must capture the proton from the O on the surface of pristine In_2O_3. However, due to the lower electronegativity of C, this process is difficult to occur. When Pt was loaded, the proton first formed a Pt–H bond with Pt, and the electronegativity of C was higher than that of Pt, so C in the CO_2 molecule can easily obtain H, which was more conducive to the generation of CH_4.

3.3.4 Mass transfer of CO_2.

When an aqueous solution is used as a hole sacrificial agent, the catalyst, H_2O and CO_2 constitute a three-phase system. In this system, the mass transfer of CO_2 is a very important step in the CO_2 reduction process. In general, if the concentration of CO_2 molecules on the catalyst surface is too low relative to H^+, the catalyst surface is more likely to undergo HER reaction rather than CO_2 reduction reaction. Therefore, promoting the mass transfer process of CO_2 molecules in aqueous solution is an effective means to inhibit the HER reaction. Li et al.[75] loaded Pt on polymeric C_3N_4 nanosheets with a hydrophobic surface to explore the effect of CO_2 mass transfer process on the HER reaction. Pt has a strong electron capture ability and HER reaction promotion ability. For hydrophilic C_3N_4, only a few electrons on the photocatalyst surface were used in the CO_2 reduction reaction. The selectivity of the C derivative in the product was only 2.5%. Compared with the hydrophilic surface, the hydrophobic surface of the C_3N_4 is more conducive to the mass transfer process of CO_2 molecules, thereby increasing the concentration of CO_2 molecules adsorbed on the surface of the material. In this case, the co-catalytic effect of Pt was more favorable to CO_2 reduction reaction than HER, and the proportion of C derivative increased to 87.9%. Therefore, the design of the photocatalyst to enhance the CO_2 mass transfer process is a very clever means to inhibit the HER reaction. However, it is still difficult to improve the selectivity of specific C derivatives only by controlling mass transfer of CO_2.

3.3.5 Reduction reaction.

After light excitation and photo-generated carrier transfer, CO_2 molecules will be adsorbed by the photocatalyst and then reduced along a specific reaction pathway. In this process, various energies and chemical bonds are involved, which makes the whole process quite complicated. However, through reasonable regulation of some factors in this complex process, the selectivity of the product can be controlled

to a certain extent. The coordination between the CO_2 molecule and the catalyst is the starting point of the entire reaction pathway. Different coordination modes will affect the formation of various products in the subsequent reduction process. Yang et al.[76] introduced O vacancies in Bi_2MoO_6 so that CO_2 molecules formed a new adsorption mode on its surface. In the presence of O vacancies, the C atoms in CO_2 molecules bonded to the O site on the material surface, and the two O atoms in CO_2 molecules bonded to the two surface Bi atoms. For the pristine Bi_2MoO_6, CO_2 molecules were more likely to bond with O atom and single Bi atom on the surface. Therefore, the new coordination mode introduced by the O vacancy made the adsorption of CO_2 on the material more stable. Under the influence of this special coordination mode, the conversion of *CO to *CHO was more thermodynamically feasible, which in turn facilitated the formation of CH_4. In a complete reduction pathway, many different intermediates are involved. The adsorption capacity of the photocatalyst to the intermediate affects whether the subsequent hydrogenation reaction can proceed. If the interaction between the intermediate and the photocatalyst is weak, the intermediate will be desorbed from the photocatalyst surface as a by-product. It is a method to enhance the selectivity of a particular product by reasonably designing the material to change its adsorption capacity to an intermediate. Liu and colleagues successfully synthesized highly graphitized carbon dots containing nitrogen groups (GCDs).[77] In the CO_2 photoreduction experiment, GCDs showed 74.8% electronic selectivity of CH_4. The nitrogen-containing groups on the surface of GCDs can produce strong chemical adsorption to the *CO intermediate, thereby preventing the desorption of the intermediate and inhibiting the formation of CO products. The *CO intermediate can be further reduced to CH_4. For amorphous carbon dots (ACDs), *CO intermediate was more likely to desorption on the surface due to their lack of strong chemical adsorption capacity for *CO intermediates. The reduction of CO_2 is a multi-step reaction process, and the formation of each intermediate corresponds to the different energy barrier. Therefore, the selectivity of the product can be controlled by lowering the energy barrier. Tan et al.[78] increased the metal and hydroxyl defects in Ni Al-LDH by reducing the thickness of the material. In the process of CO_2 reduction by using Ni Al-LDH without defects as a photocatalyst, the conversion of *CH_3 to CH_4 was a potential-determining step for the formation of CH_4, and the introduction of hydroxyl defects reduced the energy barrier of this step from 0.486 eV to 0.329 eV. In addition, the Gibbs free energy barrier decreased from 0.329 eV to 0.127 eV and 0.163 eV after the Ni vacancy and Al vacancy were introduced. The lower Gibbs free energy barrier is more conducive to the formation of CH_4. Under suitable defect conditions, the optimal selectivity of CH_4 reached 70.3%. The formation of various intermediates involves the formation and breaking of various chemical bonds. In some cases, photocatalysts can break certain chemical bonds, thus affecting the selectivity of products. Ouyang et al.[79] synthesized dinuclear cobalt complex $[Co_2(OH)L^1](ClO_4)_3$ for CO_2 photoreduction. After a series of reduction reaction steps, the $[L^1Co^{II}Co^{II}(-COOH)]^{3+}$ intermediate was generated. Under the action of the

19164 | J. Mater. Chem. A, 2020, **8**, 19156–19195

This journal is © The Royal Society of Chemistry 2020

photocatalyst, the C–OH bond in this intermediate was broken. One Co in the dinuclear cobalt complex was bonded to CO, and the other Co was bonded to OH$^-$. After that, CO was released from the intermediate, and the selectivity can reach 98%. During the formation of CO, the cleavage of C–OH is a rate limiting step. Therefore, the photocatalyst promotes the cleavage of C–OH, which means that it promotes the conversion of CO_2 to CO.

In short, through different coordination modes and reaction pathways, CO_2 will be reduced to different intermediates and final products. Through the in-depth study of CO_2 reduction pathways, the high selectivity of target products should be controllable in the future. In the process of studying the reduction pathways and product selectivity, experimental research and theoretical calculation are two indispensable methods, while DFT is an irreplaceable theoretical calculation method at present.

4. DFT calculation of CO_2 photoreduction

DFT was proposed by Hohenberg and Kohn in 1964 to study the ground state properties of multi-particle systems.[80] The DFT originated from the Thomas–Fermi model proposed by Thomas and Fermi in 1927, which explicitly expressed the electron kinetic energy in the form of electron density for the first time, but this model is relatively crude. In DFT, because there are too many wave function variables in the multi-electron system, the wave function is not taken as the basic variable in the research process, and the electron density $\rho(r)$ is directly studied, which greatly reduces the computational difficulty of the molecular electron structure. In the study of photocatalytic reduction of CO_2, DFT has become one of the most commonly used and necessary calculation methods. The DFT calculation can help us better understand the electronic excitation process, energy band structure, adsorption energy (Ea), defects of the photocatalytic material, and so on. In particular, through the calculation, the possible complete path of CO_2 reduction can be analyzed clearly.

DFT calculations can help us analyze the relationship between material microstructure and performance. For example, the doping site of a material can be studied by calculating the formation energy. In the study of CO_2 photoreduction by S-doped graphitic C_3N_4 (g-C_3N_4) nanosheet, Wang and co-workers verified the doping site of S element by DFT calculation.[81] There were three different doping sites, namely N_{Cen}, N_{Aro}, and N_{Tet}. Among them, three heptazine rings in g-C_3N_4 were connected to the N_{Tet} site, which can be ignored. N_{Cen} and N_{Aro} were connected to the C atom with a 3-fold coordination and a 2-fold coordination, respectively. In order to identify the possible doping sites, the formation energy (E_{form}) of the two sites was calculated. The formation energy of N_{Cen} and N_{Aro} sites was −1.59 eV and −2.98 eV, respectively. It can be seen that the doping of N_{Aro} site was more stable, so the doping of N_{Aro} site was considered as the doping mode of the catalyst. In addition to doped sites, vacancies are common research

objects, and DFT calculations can also be used to study the effect of material vacancies on material properties. Yang et al.[82] studied the effect of O vacancies on the performance of Bi_2MoO_6 photocatalytic reduction of CO_2. After comparing the band structure and density of state (DOS) of Bi_2MoO_6 and Bi_2MoO_6-OVs, they found that an intermediate band appeared in the energy gap of Bi_2MoO_6-OVs, and this intermediate band promoted the transfer of photogenerated carriers. In addition, the influence of O vacancies on the adsorption performance of the materials was determined by calculating the adsorption energy and the electron density on the surfaces of the two materials. The calculation results showed that the adsorption of CO_2 molecules by Bi_2MoO_6-OVs was more stable, and O vacancies played a significant role in the adsorption process. In the above studies, the adsorption energy is an important evaluation index to evaluate the relationship between the adsorption property and vacancy of materials, which can also be used to study the relationship between the thickness of materials and the adsorption capacity. For example, Chen et al.[83] calculated that the adsorption energy of the bulk Co_3O_4 and the monolayer Co_3O_4 for CO_2 molecules were −0.13 eV and −0.27 eV, respectively. The more negative Ea, the stronger the adsorption capacity, so the single-layer Co_3O_4 has stronger CO_2 adsorption ability. Besides, they also calculated that the adsorption energies of bulk Co_3O_4 and monolayer Co_3O_4 to H atoms were −0.16 eV and −0.10 eV, respectively, thereby further indicating the adsorption selectivity of monolayer Co_3O_4 for CO_2 molecule.

DFT calculation can also be used to analyze the electronic structure of the material. Saeedeh S. Tafreshi and co-workers successfully synthesized Ag_3PO_4 (111)/g-C_3N_4 complex and used it in the study of CO_2 photoreduction.[84] They analyzed the electronic structure of Ag_3PO_4 (111)/g-C_3N_4 through total DOS (TDOS) and projected DOS (PDOS) calculations. The compound's valence band maximum (VBM) and conduction band minimum (CBM) were occupied by different atomic orbits. As can be seen from the Fig. 9a, the CBM of the composite material was mainly dominated by the atomic orbital of g-C_3N_4, while the VBM was mainly dominated by the atomic orbital of Ag_3PO_4 (111). And then from Fig. 9b and c, we can see that VBM was mainly occupied by O (p) and Ag (d) orbitals in Ag_3PO_4 (111). CBM was mainly occupied by C (p) and N (p) orbitals in g-C_3N_4, while O (p) and Ag (d) also occupied a part. The band gap of hybrid materials decreased from 2.75 eV of Ag_3PO_4 (111) and 3.13 eV of g-C_3N_4 to about 2.52 eV, which enhanced the photocatalytic activity of materials in the visible region. In addition, for the Ag_3PO_4/Ag/g-C_3N_4 complex, the total DOS and energy bands were further studied and the existence of the midgap was found, thereby confirming the existence of Ag at the interface of Ag_3PO_4 and g-C_3N_4. Through PDOS analysis, the formation of midgap state was mainly the result of the combined action of the Ag, O, C, and N atoms (Fig. 9d–i). Moreover, DFT calculation can also be used to elucidate the electron excitation process during photoreduction of CO_2. Lu et al.[85] successfully synthesized porphyrin-tetrathiafulvalene covalent organic frameworks (TTCOF-M, M = 2H, Zn, Ni, Cu). Electric-deficient metalloporphyrin (TAPP) was covalently coupled with electron-rich tetrathiafulvalene (TTF) within
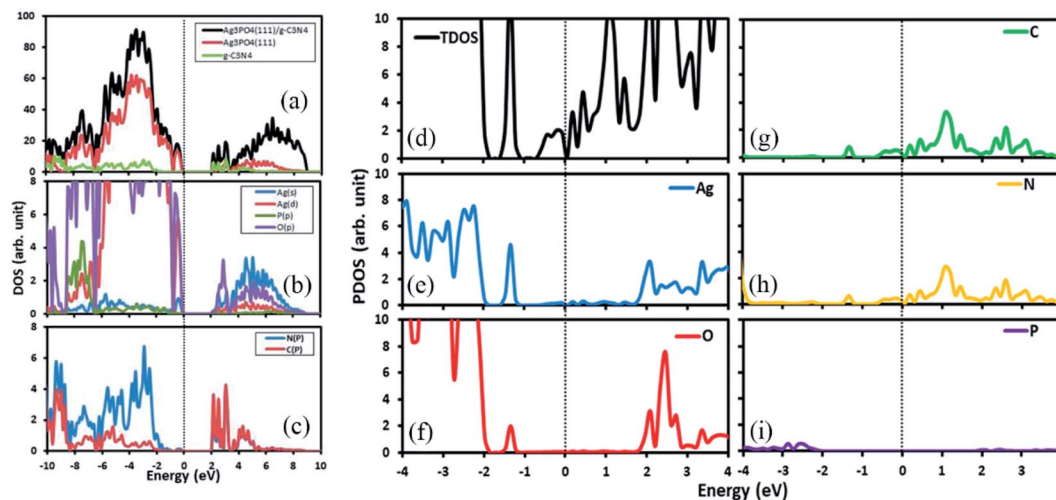
This journal is © The Royal Society of Chemistry 2020

J. Mater. Chem. A, 2020, 8, 19156–19195 | 19165

Fig. 9 (a) TDOS and PDOS of the hybrid Ag_3PO_4 (111)/g-C_3N_4. (b) PDOS of Ag_3PO_4(111) in the hybrid Ag_3PO_4 (111)/g-C_3N_4. (c) PDOS of g-C_3N_4 in the hybrid Ag_3PO_4 (111)/g-C_3N_4. (d) TDOS of the hybrid Ag_3PO_4 (111)/Ag/g-C_3N_4. (e)–(i) PDOS of the hybrid Ag_3PO_4 (111)/Ag/g-C_3N_4. Energy = 0 eV corresponds to the Fermi level. Reproduced with permission from ref. 84. Copyright 2019 American Chemical Society.

COFs. They elaborated the transfer process of photogenerated carriers through DFT calculation. In the electronic structure of the photocatalyst, HOMO was dominated by the TTF portion, and LUMO was dominated by the TAPP portion. Then, the photoinduced electron transfer (PET) process occurred under light conditions, forming TAPP-M⁻ and TTF⁺, respectively. For TTF⁺, the spin density was mainly concentrated on the C=C bond and S atom, so the oxidation of H_2O molecules occurred at both sites, and the reduction of CO_2 occurred at the metal ion center of TAPP-M⁻.

In addition to the above applications, DFT calculation is also widely used in the analysis of CO_2 reduction pathways, which is difficult to be intuitively represented through the experimental process alone. When analyzing the reduction pathways, it is necessary to determine the coordination mode of the CO_2 molecules on the photocatalyst surface, and this process can be realized by DFT calculation. Sun Hee Yoon and co-workers investigated the selectivity of homogeneous and heterogeneous $CuFeO_2$/CuO complexes in converting CO_2 to formate by theoretical calculation, and the materials was named HMS and HTS, respectively.[51] In order to better study the adsorption mode of CO_2 molecules on the surface of the material (Fig. 10b), the adsorption energy of CO_2 was first calculated (Fig. 10a). For HTS and HMS, the tridentate bonding had the most negative adsorption energy, so CO_2 molecules can be strongly adsorbed at Cu_1–Fe_1–Cu_2 sites of HMS and the Cu_2–Cu_3–Cu_4 sites of HTS (Fig. 10d and i). The oxygen coordinated monodentate bonding (O_{CO_2}-monodentate) of the material were the weakest. For bidentate bonding, the adsorption energy of carbon coordination (C_{CO_2}-bidentate) was more negative than that of oxygen coordination (O_{CO_2}-bidentate). Therefore, it can be seen that the stability order of the four coordination modes was: tridentate > C_{CO_2}-bidentate > O_{CO_2}-bidentate > O_{CO_2}-monodentate. Subsequently, the redistribution of the charge on the surface of the material was evaluated by Bader charge analysis. During this analysis, positive and negative represent the donation and

reception of electrons by the atoms in the adsorbed CO_2 molecules, respectively. For both O_{CO_2}-monodentate and O_{CO_2}-bidentate (Fig. 10c, f, h, and k), the valence electrons of the O atom in the CO_2 molecule were negative, and the net charge of O_{CO_2}-monodentate and O_{CO_2}-bidentate were negative, confirming that the CO_2 molecule behaved as Lewis acid to receive electrons from the site on the catalyst surface. Therefore, negatively charged O atoms and positively charged H atoms will combine to form $HCOO^-$. Through the same analysis method, for HMS, since the net charge of tridentate (Fig. 10d), C_{CO_2}-bidentate (Fig. 10e), and C_{CO_2}-monodentate (Fig. 10g) were all positive, the transfer of electrons to the CO_2 molecule was suppressed. But it is feasible for the HTS to donate electrons to CO_2 because of negative net charge in C_{CO_2}-bidentate (Fig. 10j) and C_{CO_2}-monodentate (Fig. 10l) modes. In the analysis of the CO_2 reduction pathways, reaction energy and activation energy are two very important factors, which can be expressed through PBE + U, PBE + D3 and so on. In addition, several intermediates in the path are often the key to determine the subsequent products. The adsorption energy of the intermediate products is used to determine whether the substance will desorb, that is, whether it plays a role as an intermediate or a by-product. In short, exploring the CO_2 reduction pathways is a relatively complicated problem, and it must be analyzed through a series of DFT calculations combined with experiments. The specific CO_2 reduction pathways has been detailed in Section 3.

5. 2D nanomaterials for CO_2 photoreduction

2D materials have great application potential in the field of CO_2 photoreduction. Many semiconductor 2D materials can directly act as photocatalysts or co-catalysts, and some non-semiconductor 2D materials can achieve good photocatalytic performance through appropriate modification, or play other
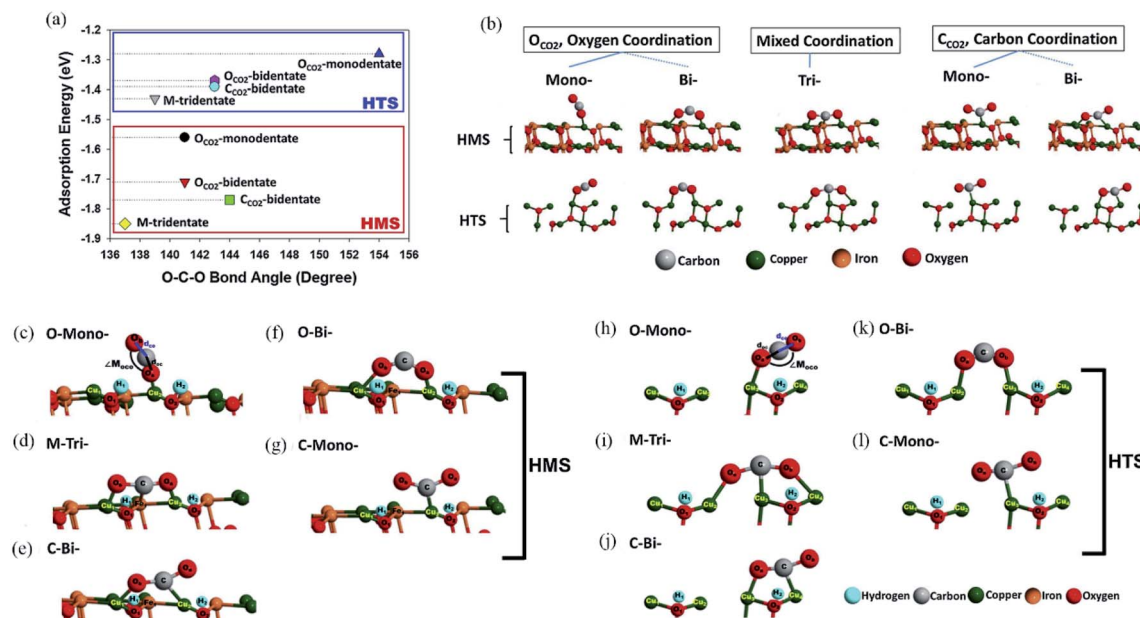
19166 | J. Mater. Chem. A, 2020, **8**, 19156–19195

This journal is © The Royal Society of Chemistry 2020

Fig. 10 (a) The adsorption energy of HMS and HTS under oxygen, carbon, and mixed coordination. (b) Schematic diagram reflects various coordination adsorption modes of CO_2 molecules in HTS and HMS systems. (c)–(l) Schematic diagram reflects the CO_2 adsorption configurations. Reproduced with permission from ref. 51. Copyright 2019 Elsevier.

critical roles (such as transferring electrons, acting as a carrier, *etc.*) in the reduction reactions.[86]

5.1 Metal-containing 2D nanomaterials

5.1.1 MXenes-based photocatalysts. In 2011, Ti_3C_2 was obtained by exfoliating from Ti_3AlC_2, which opened the curtain of MXenes material utilization in photocatalysis.[87] MXenes refer to transition metal carbides, nitrides, and carbonitrides, which are a new class of 2D layered materials. There is no direct precursor of MXenes material in nature, so the material is usually produced in the MAX phase. The MAX phase has the general formula $M_{n+1}AX_n$, where n can be 1, 2, or 3. M, A, and X in the formula represent the early transition metal element, the IIIA or IVA elements, and the C or N element, respectively.[88,89] For the structure of MAX, the stability of layer A is worse than that of layer M–X. Based on this feature, layered MXenes material can be obtained by selectively exfoliating layer A. Intercalation agents such as dimethylsulfoxide (DMSO) and LiF can be added to obtain an ultra-thin material during the exfoliating process.[29] It is worth noting that during the exfoliating process, some terminated groups (such as OH, F, and O) are spontaneously generated without relying on other reaction paths.[90] Therefore, the general formula of MXenes is $M_{n+1}X_nT_x$, where T represents surface terminating groups. So far, more than 10 kinds of MXenes have been successfully synthesized, such as $Ti_3C_2T_x$, Mo_2CT_x, V_2CT_x, Nb_2CT_x, *etc.*

MXenes have some special properties: (i) the surface termination of the MXenes material affects the performance of photocatalysis.[91] Zhang and co-workers reported that when the O-termination group of the surface was incomplete, oxygen vacancies were introduced on the surface.[92] These oxygen vacancies strongly adsorb reactants (such as CO_2) for

photocatalytic reactions. In addition, the surface hydrophilic functional groups can enhance the connection between MXenes and other photocatalysts, which facilitates the formation of heterostructures.[93] (ii) MXenes are unstable under high temperature conditions and easily oxidized. Huang *et al.*[94] used Ti_3C_2 as a carbon skeleton and titanium source, and oxidized it to form N-doped $TiO_2@C$ under high temperature conditions. The apparent rate constant of photocatalytic degradation of phenol reached 1.646×10^{-2} min^{-1}. (iii) The excellent electrical conductivity of MXene material enables it to act as an "electronic sink", which is beneficial to the transfer of electrons, so MXene material can be used as an excellent co-catalyst.[95] (iv) Due to the amount of interlayer space of MXene material, it is beneficial to the adsorption of gas molecules. Wang and co-workers found that the CO_2 adsorption capacity of the intercalated Ti_3C_2 was 5.79 mmol g^{-1}, and the original Ti_3C_2 had a CO_2 adsorption capacity of only 1.33 mmol g^{-1}.[96]

The ideal pristine MXenes are metallic and have no semiconductor properties, so the bare MXenes cannot be used as a photocatalyst alone.[97] Although some MXenes acquire semiconducting natures under the action of surface termination groups, few MXenes have been used for photocatalysis alone due to the mismatched band structure. Because of their lower Fermi level, metallic MXenes are usually used as the excellent co-catalyst.[98] In the study of photocatalytic reduction of CO_2, MXenes mainly form composites with other semiconductors to improve the photocatalytic performance of materials.

Due to its large specific surface area and excellent electrical conductivity, the 2D MXene material can serve as a carrier for many photocatalysts. For example, Cao and co-workers successfully prepared 2D/2D ultrathin Ti_3C_2/Bi_2WO_6 nanosheets and applied them to CO_2 reduction experiment.[99] Ti_3C_2

material was obtained by selective ultrasonic exfoliating of Al element from layered Ti_3AlC_2, and then Bi_2WO_6 nanosheets were grown on Ti_3C_2 surface (Fig. 11). Under simulated visible light irradiation, the yields of methane and methanol were 4 and 6 times that of pristine Bi_2WO_6 nanosheets, respectively. MXenes can form a heterojunction with other photocatalysts to improve photocatalytic effects. Wang et al.[100] prepared the quasi-core-shell In_2S_3/anatase TiO_2@metallic $Ti_3C_2T_x$ hybrids by in situ hydrothermal method. A double heterojunction structure of type-II heterojunction and Schottky junction was simultaneously formed in the material, and the formed electron channel greatly promoted the transfer efficiency of photo-generated electrons. Excellent photocatalytic performance was determined by the visible light absorption capacity of In_2S_3, the wide bandgap of TiO_2, and the conductivity of MXenes. Su et al.[101] synthesized Nb_2O_5/C/Nb_2C (MXenes) material by one-step oxidation of CO_2. The Schottky junction was formed on the surface of Nb_2O_5/Nb_2C. The electrons were transferred from Nb_2O_5 to Nb_2C, and Nb_2C served as electron sink. At the same time, due to the intimate combination between Nb_2C and Nb_2O_5, the transfer of electrons was greatly promoted. Furthermore, the termination of the MXenes material can be fully utilized to enhance the CO_2 reduction efficiency. Ye et al.[102] used the surface-alkalinized Ti_3C_2 as a co-catalyst to improve the ability of commercial titania (P25). The hydroxyl group on the surface of the Ti_3C_2 can provide abundant active sites, which was beneficial to the adsorption and activation of CO_2 molecules. The yields of CO and CH_4 were 11.74 and 25 μmol g^{-1} h^{-1}, which were 3-fold and 277-fold that of pristine P25, respectively. Related studies have shown that MXenes materials can inhibit photocorrosion of CdS. Xie et al.[103] showed that after 2D Ti_3C_2 and CdS constitute a heterojunction, Ti_3C_2 can be employed as an electron mediator. At the same time, due to the strong interaction between Cd^{2+} and Ti_3C_2, the Cd^{2+} generated during the process of photocorrosion was confined on the Ti_3C_2 mezzanine, effectively preventing the leakage of Cd^{2+}.

5.1.2 LDHs-based photocatalysts. In 1842, Hochstetter first discovered the natural hydrotalcite mine from the schist deposit in Sweden, and Feitknecht successfully synthesized $[Mg_6Al_2(OH)_{16}]CO_3 \cdot 4H_2O$ in 1942.[104,105] LDHs are a type of "hydrotalcite-like compounds", also known as anionic clay, which have great application value in catalysis, medicine, adsorption, and ion exchange.[106–109] The general formula of LDHs is $[M_{1-x}^{2+}M_x^{3+}(OH)_2]^{x+}[A_{x/n} H_2O]^{x-}$, where A represents an anion between layers, such as CO_3^{2-}, SO_4^{2-}, Cl^- and ClO_4^-, etc. M^{2+} and M^{3+} represent the divalent and trivalent cations, respectively. The common divalent cations contained in LDHs are Mg^{2+}, Co^{2+}, Ni^{2+}, or Zn^{2+}, and trivalent cations are Al^{3+}, Cr^{3+}, or Fe^{3+}.[110,111] However, in some special cases, LDHs also contain some monovalent and tetravalent cations, such as Li^+, Zr^{4+}, Ti^{4+}, and Sn^{4+}.[112] LDHs have a unique host–guest structure, the host structure of LDHs consists of a positively charged brucite-like layer. Each octahedron forms a unit layer by a common edge, wherein OH^- is located at the apex of each octahedron, and the center of the octahedron is metal cation.[113] According to the occupancy of the central cation, the host structure can be divided into two types, one is the trioctahedron in which all octahedral centers are occupied by metal ions, and the other is the dioctahedron in which two-thirds of the centers are occupied by metal ions. There are also some guest substances between the brucite layer of LDHs: charge-balance cations and crystal water molecules.[114] The electrostatic attraction between the positively charged brucite layer and the negatively charged interlayer ensures the stability of the LDHs structure.

In 2011, Izumi's group used Zn–Cu–M (III) (M = Al, Ga) LDHs materials for photocatalytic reduction of CO_2 for the first time.[115] They synthesized Zn and/or Cu hydroxides and combined them with Al or Ga. Zn–Al LDH was the most active in reduction reaction, and the yield of CO was 620 nmol h^{-1} g$_{cat}^{-1}$. After Cu was introduced into Zn–Al LDH and Zn–Ga LDH, the selectivity of methanol improved from 5.9 to 26 mol% and from

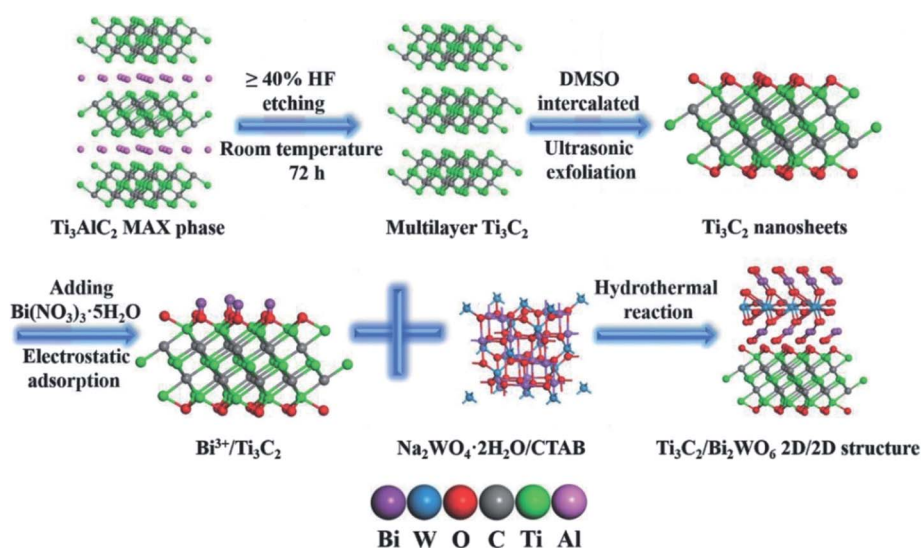**Fig. 11** Schematic illustration of the synthetic process of 2D/2D heterojunction of ultrathin Ti_3C_2/Bi_2WO_6 nanosheets. Reproduced with permission from ref. 99. Copyright 2018 Wiley-VCH.

19168 | J. Mater. Chem. A, 2020, **8**, 19156–19195

This journal is © The Royal Society of Chemistry 2020

39 to 68 mol%, respectively. Since then, LDHs have received more and more attention in CO_2 photocatalytic reduction due to their unique characteristics. Firstly, due to the Lewis acidity of CO_2, alkaline photocatalysts tend to have greater advantages in the adsorption of CO_2 molecules. The host structure of LDHs contains a large amount of alkaline OH groups, which can effectively adsorb CO_2 molecules. Wang and co-workers prepared Co–Al LDH nanosheets for photocatalytic CO_2 reduction at atmospheric concentration (400 ppm) under visible light irradiation.[116] The yield of methane was 4.3 μmol g^{-1} h^{-1} without the addition of sacrificial agent and noble metals. After five cycles of repetition test, the yield of CH_4 remained almost unchanged, the material exhibited excellent stability. The CO_2 adsorption capacity of Co–Al LDH was 2.95 cm^3 g^{-1}, which was about twice higher than P25. In this experiment, the better photocatalytic performance was mainly due to the strong adsorption capacity of alkaline OH groups on the surface of Co–Al LDH. Secondly, the composition of LDHs is controllable. LDHs generally contain two or three different metal cations, so the photocatalytic properties of the material can be changed by adjusting the proportion of metal cations. This principle is similar to the element doping process of semiconductor photocatalysts. Kong et al.[117] studied the performance of Ti–Li–Al LDH with different Ti : Li : Al molar ratios in CO_2 photocatalytic reduction. By comparing $Ti_1Li_3Al_1$-LDHs, $Ti_1Li_3Al_2$-LDHs, Ti_1-Li_3Al_3-LDHs, and $Ti_1Li_3Al_4$-LDHs, $Ti_1Li_3Al_2$-LDHs exhibited the largest specific surface area and the strongest CO_2 adsorption capacity, and the yield of methane was 1.33 mmol h^{-1} g^{-1}. At the same time, by theoretical calculation, it was found that $Ti_1Li_3Al_2$-LDHs was the p-type semiconductor with the narrowest bandgap among all the samples. In addition to the proportion of metal ions, Xiong et al.[118] studied the effect of the types of metal cations in LDHs on the selectivity of CO_2 photoreduction products. They performed photoreduction experiments on Zn-based LDH containing different trivalent and tetravalent metal ions, as well as in situ diffuse reflectance infrared measurements and DFT calculations. The results showed that when the d-band center of cations was relatively close to the Fermi level, the CO_2 molecules were more likely to be reduced to CH_4 or CO. The cations with the d-band center far away from the Fermi level had poor adsorption capacity on CO_2 molecules, and H_2 was more likely to be produced in this process. Thirdly, the interlayer space of LDHs is the main site of photocatalytic process, and the interlayer space contains some anions and H_2O molecules. The proper regulation of the interlayer space of LDHs will affect its photocatalytic performance. Wein et al.[119] pretreated Zn–Cu–Ga–CO_3 LDH with 423 K in a vacuum environment for 1 h, liberating 31% of the crystal water in the interlayer space. After photocatalytic reduction of CO_2, the methanol yield was 2.8 μmol g$_{cat}^{-1}$ h^{-1}. Under the same conditions, the methanol yield of the unpretreated Zn–Cu–Ga–CO_3 LDH material was 0.011–0.30 μmol g$_{cat}^{-1}$ h^{-1}. Therefore, the liberation effect of the interlayer space is very obvious. On the other hand, since the interaction between the LDHs laminate and the interlayer anions is weak, the interlayer anions have a certain exchangeability, so the photocatalytic performance can be improved by introducing different interlayer

anions. Finally, since the metal cation is located at the center of the octahedron in the host structure, the recombination of photogenic carriers is suppressed due to the high dispersion of metal cation, thereby effectively improving the efficiency of photocatalytic reduction of CO_2.

Ultrathin LDHs, with their outstanding structural properties, are often more popular than bulk LDHs in CO_2 photocatalytic reduction. The thickness of 2D LDHs is an important factor affecting its photocatalytic performance.[120] It is generally believed that ultrathin materials tend to expose more surface defects, while in LDHs, they mainly appear as oxygen vacancies and metal vacancies. For example, Zhao et al.[121] reduced the thickness of the Zn–Al LDH sheet to create O vacancies, which in turn resulted in the formation of coordinated unsaturated Zn, thereby enhancing the photoreduction efficiency of CO_2. Tan and co-workers synthesized Ni–Al LDHs materials with the thickness ranging from 27 nm to 5 nm and to 1 nm.[78] The material was characterized by X-ray absorption fine structure, soft X-ray absorption spectroscopy and positron annihilation spectrometry, and the results proved that lower material thickness has more metal defects. Although LDHs materials have many advantages, the photocatalytic properties of pristine LDHs are often unsatisfactory, so researchers often synthesize complexes to achieve higher photocatalytic activity. For example, Jiang and co-workers synthesized $0.1Cu_2O@Zn_{1.8}Cr$ LDH for CO_2 photocatalytic reduction,[122] and the CO yield was 6.3 μmol after 24 h, while the CO yield was only 0.1 μmol when LDH was not loaded with Cu_2O. In this process, Cu_2O acted as electron traps, which promoted the transfer of charge. Gao et al.[123] successfully assembled Fe_3O_4/Mg–Al LDH by co-precipitation method and used it in CO_2 photocatalytic reaction. The production rate of CO (422.2 μmol g^{-1} h^{-1}) and CH_4 (223.9 μmol g^{-1} h^{-1}) were 1.8 and 1.7 times that of pristine Mg–Al LDH, respectively. In this composite, Fe_3O_4 facilitated the separation of electrons and holes, while 2D Mg–Al LDH could reduce the transmission resistance of electrons and provide more active sites.

In addition to being an excellent photocatalytic material, LDHs can also serve as a precursor for other photocatalysts. LDHs have a number of advantages as a precursor, such as high dispersion of metal cations at the atomic level, high specific surface area, and homogeneous microstructure, etc.[124] Chen et al.[125] successfully produced a series of CoFe-based photocatalysts by hydrogen reduction of Co–Fe–Al LDH nanosheets in the range of 300–700 °C. With the increase of reduction temperature, the selectivity of CoFe-x reduction products gradually shifted from CO to CH_4, and the selectivity of CH_4 in CoFe-650 reduction products reached 60%, and the selectivity of C_{2+} reached 35% (Fig. 12a). Zhao's group used Ni–Al LDH as a precursor to prepare NiO nanosheets with a large number of Ni and O vacancies.[126] They calcined Ni–Al LDH at high temperature to make it undergo topological transformation, and then obtained the catalytic material NiAl-X, where X represented the reaction temperature. NiAl-275 had the greatest CH_4 selectivity, and the HER reaction could be completely suppressed under irradiation above 600 nm (Fig. 12b).

This journal is © The Royal Society of Chemistry 2020

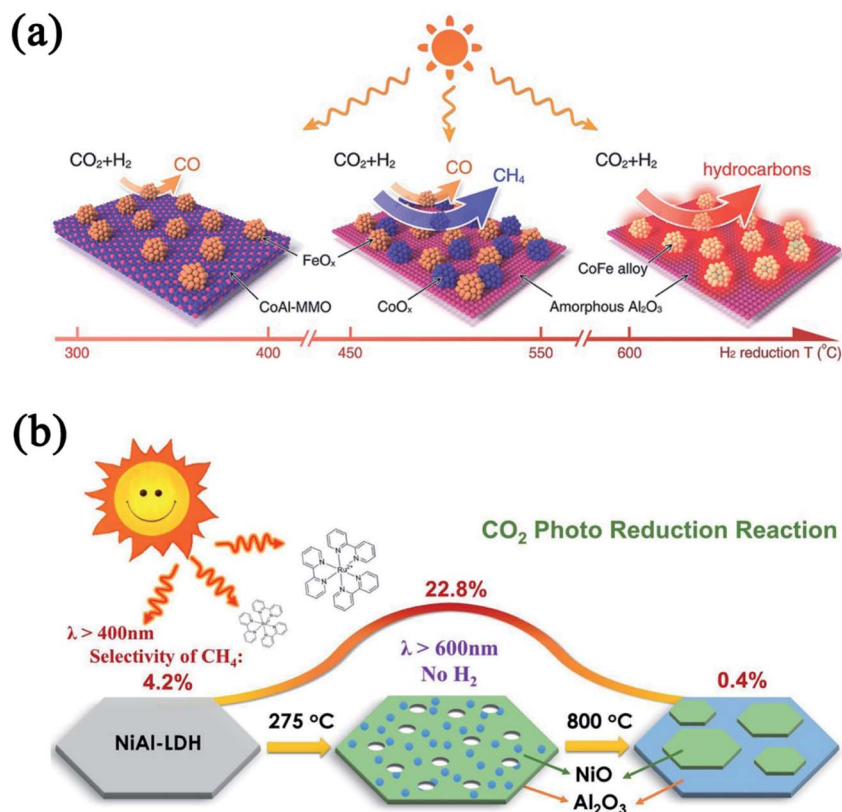J. Mater. Chem. A, 2020, **8**, 19156–19195 | **19169**

Fig. 12 (a) Schematic illustration of the different CoFe-*x* catalysts formed by hydrogen reduction of a CoFeAl-LDH nanosheet precursor at different temperatures. Reproduced with permission from ref. 125. Copyright 2018 Wiley-VCH. (b) Schematic illustration of NiAl-*X* derived from the topological transformation of NiAl-LDH. Reproduced with permission from ref. 126. Copyright 2020 Elsevier.

5.1.3 TMDs-based photocatalysts. Transition metal dichalcogenides (TMDs), a class of 2D semiconductor materials, have recently received extensive attention in the field of CO_2 photoreduction. The general formula of TMDs is MX_2, where M represents a transition metal element and X represents a chalcogen element.[127] Single-layer TMDs exhibit a X–M–X sandwich structure in which the transition metal is between two chalcogens. The atoms in the layer are connected by covalent bonds, and the atoms between the layers are connected by relatively weak van der Waals forces.[128,129] Common TMDs include MoS_2, $MoSe_2$, WS_2, and WSe_2, *etc.*, among which MoS_2 and WS_2 are widely used in photocatalytic research for their excellent performance. It is worth noting that some TMDs have different fundamental phases. For example, MoS_2 has three phases, namely 1T phase, 2H phase, and 3R phase. The 1T phase is a square symmetry single-layer repeating unit. The 2H phase is hexagonal symmetry, wherein the Mo atom maintains an octahedral coordination, and the 3R phase is a prismatic symmetric three-layer repeating unit.[130,131] Related experiments showed that MoS_2 can be converted from 2H phase to 1T phase by Li intercalation.[132–134]

TMDs are ideal materials for replacing noble metals as co-catalysts due to their high stability and low cost. In addition, under the influence of quantum confinement effect, the CB energy level of the material will change accordingly with the number of layers, so TMDs exhibit excellent co-catalytic performance.[135] Xu *et al.*[136] successfully wrapped MoS_2 nanosheets on TiO_2 fiber to form 1D/2D TiO_2/MoS_2 composites. By changing the molar percentage of surface MoS_2 relative to TiO_2, different CO_2 photocatalytic reduction effects can be obtained. The experimental results showed that when the molar percentage of MoS_2 and TiO_2 was 10, the production rates of CH_4 and CH_3OH reached the maximum, which were 2.86 and 2.55 $\mu mol\ h^{-1}\ g^{-1}$, respectively. Through the investigation of material recycling capacity, it was found that the photocatalytic activity did not decrease significantly after four cycles. In addition, MoS_2 can be used as a co-catalyst to increase the selectivity of CH_3OH in the products. Because the Mo cation site at the edge of MoS_2 is beneficial to stabilize the CH_xO_y intermediate by electrostatic attraction, it is favorable for the conversion of CO_2 to CH_3OH.[137] Compared with noble metals, MoS_2 tends to have a higher current density and a lower overpotential, which can receive photogenerated electrons more effectively in composite materials. Jung *et al.*[138] loaded few-layered MoS_2 on three-dimensional graphene aerogel and porous TiO_2 material (TGM) through simple one-pot hydrothermal method (Fig. 13a). Mesoporous TiO_2 nanoparticles and MoS_2 nanoparticles were distributed on the graphene surface (Fig. 13b and c). Photogenerated electrons were transferred from the CB of TiO_2 through the graphene to the edge of MoS_2 (Fig. 13e). The yield of CO in the final product was 92.33 $\mu mol\ g^{-1}\ h^{-1}$, which was 14.5 times that of pristine TiO_2 (Fig. 13d).

19170 | *J. Mater. Chem. A*, 2020, **8**, 19156–19195

This journal is © The Royal Society of Chemistry 2020

After 15 cycles of experiments, there is no loss of material weight, and the original conversion rate can be maintained. MoS_2 can also act as a charge-transfer mode switcher. Zhang et al.[139] prepared $WO_3@MoS_2/CdS$ composites by three-step wet chemistry, in which MoS_2 was located at the interface between WO_3 and CdS. As a charge-transfer mode switcher, MoS_2 successfully converted the type-II electron transfer mode into the Z-system. Photogenerated electrons from the CB of WO_3 and photogenerated holes from CdS can be transferred to MoS_2 for recombination. At the same time, MoS_2 provided many active sites for the whole reaction process, which improved the efficiency of photocatalysis. Therefore, in the $WO_3@MoS_2/CdS$ system, MoS_2 acted as a charge-transfer mode switcher, an electron–hole mediator, and a co-catalyst.

TMDs have some unique characteristics compared with other 2D photocatalytic materials. For example, MoS_2 generally has three phases of 1T (metallic), 2H (semiconducting), and 3R. The 1T metal configuration of MoS_2 has more active sites on the basal plane and edges, and the conductivity is better, but there is thermal dynamic metastable state. Huang et al.[140] combined the properties of 1T MoS_2 and 2H MoS_2 to synthesize 1T/2H MoS_2, and then combined the system with 2D g-C_3N_4 to form a ternary composite structure. In this system, 1T MoS_2 mainly acted as an electron trap to promote electron transfer and provided many active sites, while a heterojunction was constructed between 2H MoS_2 and g-C_3N_4 for the separation of carriers. In general, the MoS_2 material is black, so the photothermal effect will occur in the photocatalytic reaction. In the photocatalytic reaction process, there are two main sources of thermal energy, one is direct thermal radiation, and the other is the photothermal effect of the material. Guo et al.[141] successfully prepared $WS_2/MoS_2@WO_{3-x}$ double Z-system heterojunction
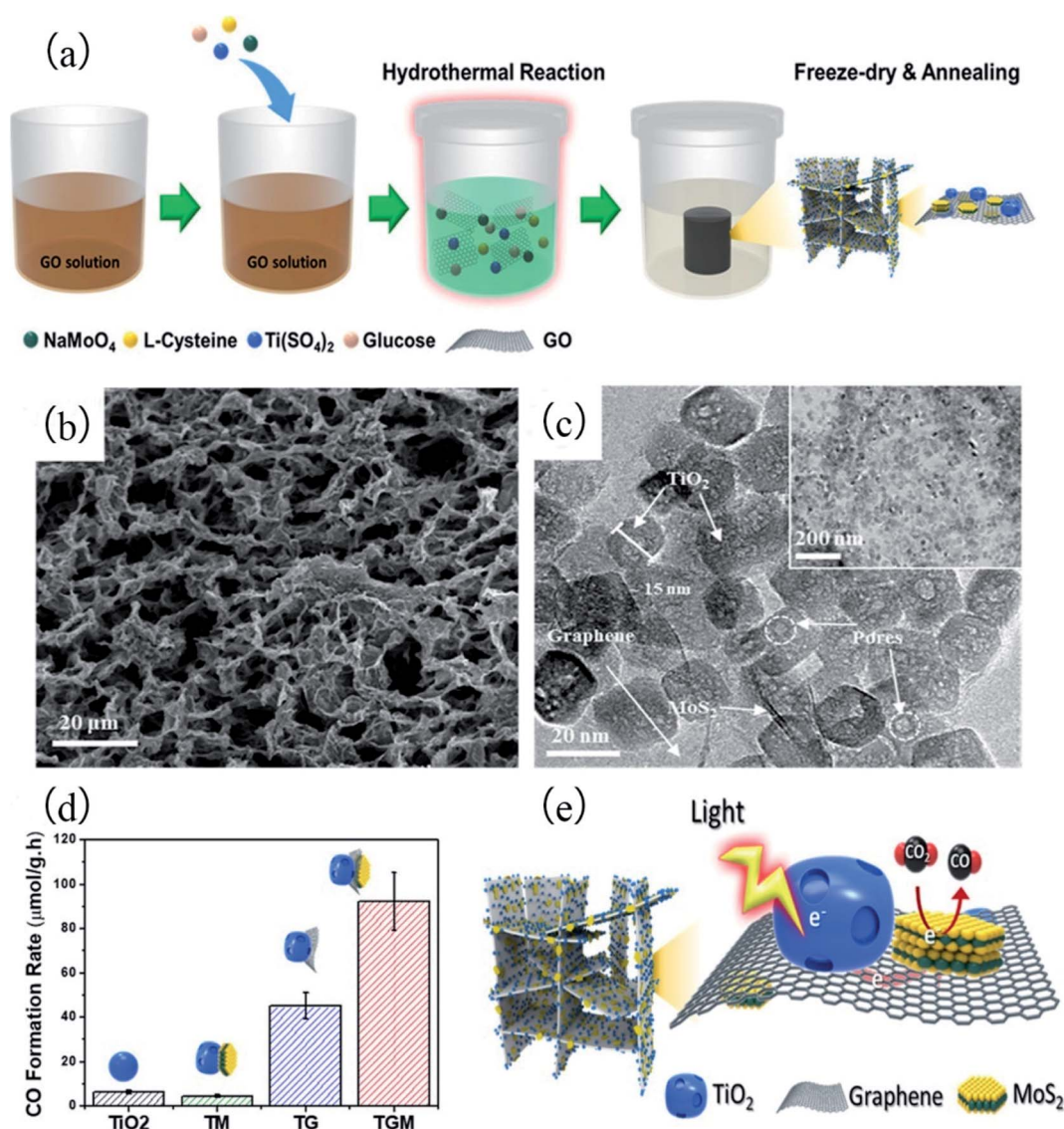

Fig. 13 (a) Schematic diagram of synthesis process of TGM through simple one-pot hydrothermal method. (b) and (c) SEM and TEM image of TGM. (d) The CO formation rate of TGM, TG, TM, and TiO_2. (e) Schematic diagram of material (TGM) structure and photogenic electron transfer process. Reproduced with permission from ref. 138. Copyright 2018 American Chemical Society.

This journal is © The Royal Society of Chemistry 2020

J. Mater. Chem. A, 2020, **8**, 19156–19195 | **19171**

photocatalyst with core–shell structure. In this experiment, the photothermal effect of the material was quantitatively studied by IR thermal driver. Before irradiation, the temperature of the material was only about 24 °C. After irradiation, the temperature of the material rose to about 190 °C, which indicated that the photothermal effect was obvious in the photocatalytic process. Therefore, the photothermal effect of MoS_2 can provide valuable reference ideas for the construction of photocatalytic materials.

At present, the main TMDs material used in the study of CO_2 photoreduction is MoS_2, and other TMDs have relatively few applications in this field. There is a report on the photoreduction of CO_2 by WSe_2. Oh's group synthesized the WSe_2–Graphene–TiO_2 ternary composite by ultrasonic technology,[142] in which WSe_2 and TiO_2 were distributed on the surface of graphene. In heterojunction systems, WSe_2 acted as an electron trap to promote the charge separation. The band gap of WSe_2–Graphene–TiO_2 was about 1.62 eV. Under the irradiation of UV-visible light, the optimal yield of CH_3OH was 6.900 μmol g^{-1} h^{-1} with Na_2SO_3 as sacrificial agent. WS_2, as an important class of TMDs, has been extensively studied in the direction of photocatalytic hydrogen evolution, degradation of pollutants, sterilization and so on,[143–146] but its research in the field of photoreduction of CO_2 is scarce.

5.1.4 Others. Metal oxides are an important class of photocatalytic materials. Metal oxides have strong antioxidant properties, and the commonly used metal oxides in photocatalysis mainly include TiO_2, ZnO, Co_3O_4, WO_3, etc.[83,147–149] TiO_2 is one of the most studied materials in the field of photocatalysis. TiO_2 has the merits of non-toxicity, low price, high stability and good photocatalytic activity. Qamar et al.[150] synthesized 2D TiO_2 nanosheets by TiO_2-octylamine hybrid method, and the ultrathin properties equipped the material with excellent performance. In the CO_2 photoreduction experiment, the yield of formate was 1.9 μmol g^{-1} h^{-1}, which was 450 times that of bulk TiO_2. However, due to its wide bandgap (3.2 eV), the response to visible light is poor, and photogenerated electrons and holes are easily recombined, which greatly limits its application.[151] In recent years, research on 2D TiO_2 has focused on the modification of materials, including element doping, morphology control, construction of heterojunctions, etc. Recently, Jiang and co-workers modified TiO_2 nanosheet with Lewis base $[WO_4]^{2-}$ in which $[WO_4]^{2-}$ substituted OH^- on the surface of TiO_2.[152] The basicity of $[WO_4]^{2-}$ can promote the adsorption of CO_2 molecules, and $[WO_4]^{2-}$ can capture photogenerated electrons. The experimental results showed that the yield of CO was 19 times that of pure TiO_2, which was higher than that of noble metal (Au, Ag) modified TiO_2. 2D ZnO has good thermal stability with a direct bandgap of 3.37 eV. When the number of layers of ZnO is reduced to about 8 layers, the structural properties of graphene-like structures appear. Zhao et al.[153] reported the effect of the number of layers of 2D ZnO on the performance of photocatalytic reduction of CO_2. When the thickness was less than or equal to 5 layers, CO and HCOOH were the main products, and the photocatalytic activity was the highest in the 3 and 4 layers. In the 6 layers, CH_3OH and CH_4 were the main products. In addition to the ZnO, Chen et al.[83]

prepared 2D porous Co_3O_4 and modified it with Ru-based photosensitizer. The ultrathin and porous properties gave the material a lower carrier recombination rate, a larger number of active sites, and a stronger ability to adsorb CO_2. The yield of CO was 4.52 μmol h^{-1}, and the selectivity was 70.1%, which were better than the bulk Co_3O_4.

Metal–Organic Frameworks (MOFs) are a kind of porous crystalline material with network structure composed of organic linkers and metal nodes, also known as porous coordination polymer.[154,155] MOFs have stimulated an immense impetus as photocatalyst because of their ultra-high surface area, adjustable pore structure as well as uniformly distributed coordination unsaturated metal sites.[156–158] Ye et al.[159] used Zn porphyrin-based MOFs as photosensitizer and ZIF-67 as co-catalyst to compare the effects of 2D MOFs and bulk MOFs on photocatalytic reduction of CO_2. The experimental results showed that when the Zn-MOF bulk was used as a photosensitizer, the turnover numbers of CO were 63.6 within 6 h. When the Zn-MOF nanosheet was used as a photosensitizer, the turnover numbers of CO could reach 117.8, and the selectivity of CO increased from 89.5% to 91.0%. There are a lot of researches on the modification of MOFs materials. Recently, Wang et al.[160] modified the material by virtue of the large amount of coordination unsaturated metal ions in the MOFs. Firstly, tetrakis (4-carboxyphenyl)-porphyrin (TCPP) interacted with cobalt carboxyphenyl, and then benzoic acid exerted an axial constraint on cobalt ions to form 2D porphyrin MOF (PMOF) (Fig. 14a). The Co active center in ultrathin porphyrin MOF would coordinate with the N atom in g-C_3N_4, and then the g-C_3N_4 quantum dots would be supported on the PMOF material to obtain g-CNQDs/PMOF hybrids (Fig. 14b). On the one hand, it was conducive to the enrichment of CO_2 at the Co site. On the other hand, it could also promote the direct transfer of electrons from g-C_3N_4 QDs to Co sites (Fig. 14c). The yields of CO and CH_4 were 2.34 and 6.02 times that of pure PMOF, respectively.

There are some metal oxyhalides that are used for photocatalytic reduction of CO_2, among which BiOX (X = Br, Cl, I) is the class of typical layered material with high photocatalytic activity.[161] The {X–Bi–O–Bi–X} layered structure stacked by nonbonding interactions causes a large space between the layers, and an endogenous electric field can be generated. Some studies have focused on improving photocatalytic performance by appropriate modification of metal oxyhalides. By controlling the time of hydrothermal reaction, Ye et al.[162] synthesized BiOI nanosheets exposed to {001} and {100} facets, respectively. The experimental results showed that BiOI-001 had good photoinduced carrier separation efficiency, high CB position, and strong CO_2 molecular adsorption capacity. Besides that, Zhu et al.[163] used Bi and phosphorylation to simultaneously modify the BiOBr in the form of the regular hierarchical spheres, and phosphorus existed in the form of $BiPO_4$. In this composite system, photogenerated electrons migrated from BiOBr to $BiPO_4$. When Bi was in contact with BiOBr and $BiPO_4$, a Schottky junction would be formed. The Schottky junction could promote the migration of photoexcited electrons from BiOBr to Bi, the carrier recombination was suppressed. In addition, the doping of Bi atoms could significantly increase the selectivity of

19172 | J. Mater. Chem. A, 2020, **8**, 19156–19195

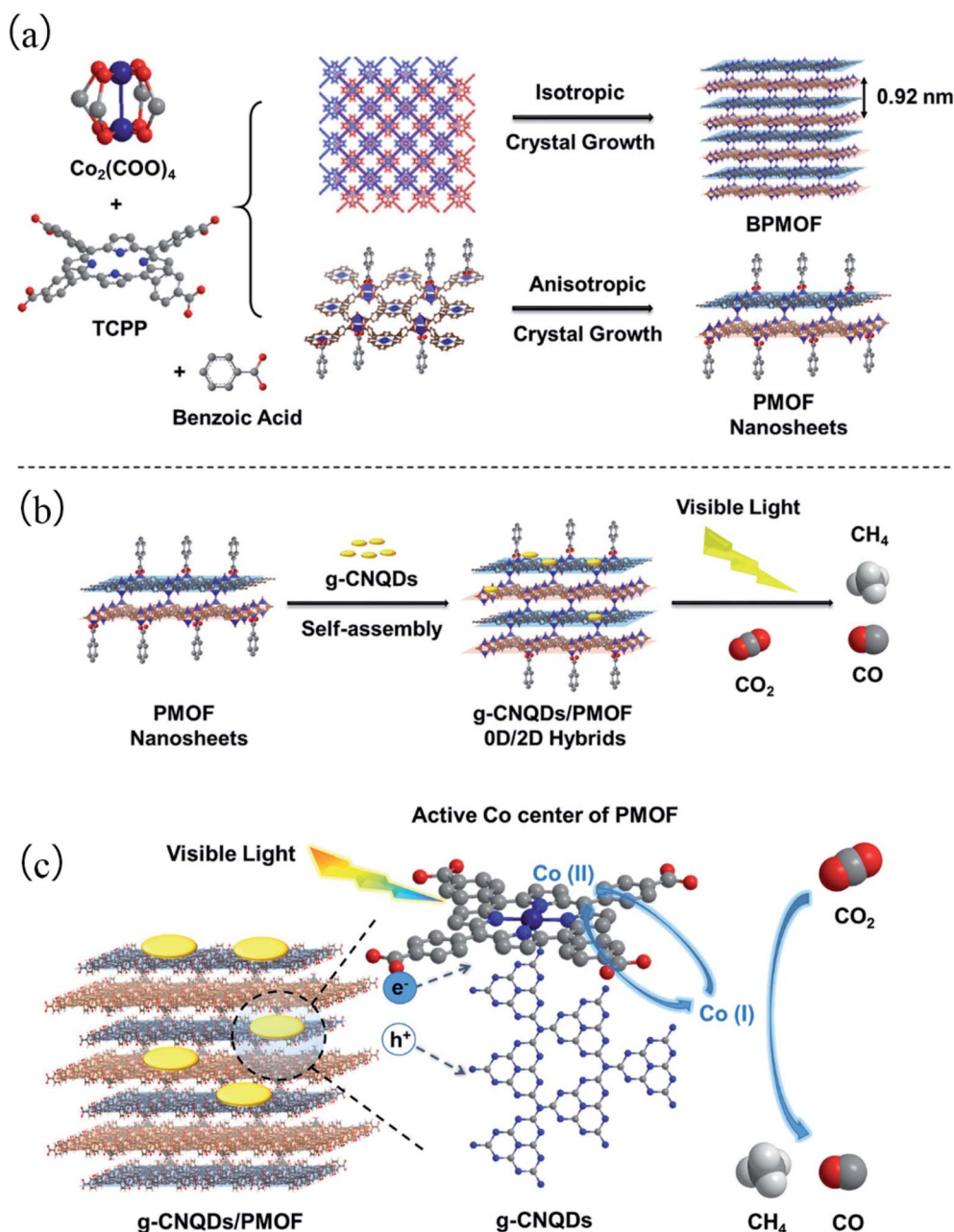This journal is © The Royal Society of Chemistry 2020

Fig. 14 (a) Schematic diagram of synthesis process of PMOF. (b) Schematic diagram of synthesis process of g-CNQDs/PMOF hybrids. (c) Proposed mechanism of CO_2 reduction over g-CNQDs/PMOF hybrids under visible-light irradiation. Reproduced with permission from ref. 160. Copyright 2019 American Chemical Society.

CH_4. Besides that, Bai and co-workers found that 2D $Bi_4O_5Br_2$ nanosheets could also exhibit good photocatalytic reduction of CO_2 performance.[164] Its large surface area and porous structure promoted the adsorption of CO_2, and the reduction products showed certain selectivity.

In addition to the above 2D metal-containing materials, there are also a few research reports on the application of 2D Bi_2WO_6 in the field of CO_2 photoreduction. For example, Wang *et al.*[165] loaded PtO_x nanoparticles on Bi_2WO_6 nanosheet with a thickness of 4.8 nm. The optimal yield of CH_4 was 108.8 ppm g^{-1} h^{-1}, which was 5.7 times higher than pristine Bi_2WO_6.

5.2 Metal-free 2D nanomaterials

5.2.1 g-C_3N_4-based photocatalysts. In 2009, Wang and co-workers applied g-C_3N_4 material to photocatalytic hydrogen evolution for the first time.[166] Since then, the door for the application of g-C_3N_4 in the field of photocatalysis has opened.[167,168] Carbon nitride consists of covalently bonded carbon and nitrogen, and the C and N atoms are sp² hybrids to form a highly delocalized conjugated π-system.[169,170] In theory, according to the structural difference, there are five types of carbon nitride in total, namely α-C_3N_4, β-C_3N_4, g-C_3N_4, cubic C_3N_4, and pseudo-cubic C_3N_4. Among them, g-C_3N_4 is

This journal is © The Royal Society of Chemistry 2020

J. Mater. Chem. A, 2020, **8**, 19156–19195 | **19173**

composed of tri-*s*-triazine, and the atoms are connected by covalent bond, which has a high thermal and chemical stability.[171–173] The bandgap of g-C_3N_4 is about 2.7 eV, where the CB and VB position are −1.3 eV and 1.4 eV, respectively. So it can effectively reduce CO_2 molecules.[174]

In 2012, Dong *et al.*[175] used the g-C_3N_4 as photocatalyst to reduce CO_2 under water vapor and visible light conditions for the first time. Due to its ease of preparation, good stability, low cost, suitable bandgap, and ease of modification, g-C_3N_4 has great potential for photocatalytic reduction of CO_2.[174,176] g-C_3N_4 has the unique tri-*s*-triazine units' structure, making it an excellent carrier material. For example, Tang and co-workers successfully implanted single titanium-oxide species into 2D g-C_3N_4 (2D TiO–CN).[177] Due to the tri-*s*-triazine units' structure, Ti^{4+}–O^{2-} was effectively anchored to g-C_3N_4 and was reduced to a highly reductive Ti^{3+}–O^- by electrons. Under the strong reduction of Ti^{3+}–O^- species, the yield of CO reached 283.9 μmol g^{-1} h^{-1}. In addition, the N atom in the skeleton of the structure could cooperate with metal ions. Huang *et al.*[178] used a simple deposition method to introduce Co^{2+} into the g-C_3N_4 material. The Co–N coordination formed between Co^{2+} and g-C_3N_4, thereby increasing the selectivity of CO in the reduction products. Due to incomplete polymerization of the amide groups-rich precursor, some NH_2 and NH groups are formed on the surface during the synthesis of g-C_3N_4. These groups impart a basic character to the g-C_3N_4 material, which promote the adsorption of CO_2 molecules with Lewis acidity. Mo *et al.*[179] successfully synthesized porous nitrogen-rich g-C_3N_4 nanotubes by simple supramolecular self-assembly method. The CO yield was 17 times higher than bulk g-C_3N_4. The introduction of amino group effectively improved the Lewis basicity and hydrophilicity of the material, thus promoting the adsorption of CO_2 molecules. But in the opposite direction, the NH_2 and NH groups are related to a large number of defects in layers, and some hydrogen bonds are formed in these defects, which makes the material distinct from those containing only covalent bonds. These defects affect carrier transport between layers. Li and co-workers introduced a carbon chain in the polymeric carbon nitride and carried out a CO_2 photoreduction experiment.[180] In this experiment, the carbon chain connected the defects in g-C_3N_4 through the action of C–N covalent bonds. The carbon chain acted as an electron channel, accelerating the separation and transfer of charge carriers. The yield of CO was 29.2 times higher than the original g-C_3N_4. In addition, Lin *et al.*[181] introduced 3,5-dibromobenzoyl chloride as π-conjugated organic subunits in the polymeric carbon nitride, and promoted the separation and transfer of photogenerated carriers by π-conjugated organic molecules. In g-C_3N_4, electrons were excited from N atoms to C atoms, but the two-coordinated N atoms were usually the photocatalytic active sites, so the excited electrons need to transfer from C atoms to N atoms again. However, in the above process, it is often difficult to excite electrons from N atoms to C atoms. Therefore, Fu and co-workers used the coordination between the B atoms and the two-coordinated N atom to dope the B atom into the g-C_3N_4 material.[182] According to theoretical calculation, it was easier to excite electrons from N to B than from N to C, and the CH_4 yield

obtained by 1% B/g-C_3N_4 sample was 32 times that of the pristine g-C_3N_4.

Although g-C_3N_4 is a good photocatalytic material, the original g-C_3N_4 still has the inherent drawbacks, such as poor adsorption capacity for CO_2 molecules, low visible light absorption range, and easy recombination of carriers.[183] Therefore, g-C_3N_4 generally combines with other materials to form a composite. In recent years, some studies have begun to focus on interfacial connections between g-C_3N_4 and other materials. In the process of combining different materials, it is easy to ignore the occurrence of lattice mismatch, which is not conducive to carrier separation and transfer. Wu and co-workers introduced phosphate-oxygen links in the g-C_3N_4/TiO_2-nanotubes (TNTs) complex.[184] The P–O bond strengthened the interface connection between g-C_3N_4 and TNTs, thus inhibiting the occurrence of lattice mismatch. The P–O bond accelerated the transfer of photogenerated electrons from TiO_2 to g-C_3N_4. The results showed that the yields of acetic acid, methanol and formic acid were 46.9 ± 0.76 mg L^{-1} h^{-1}, 38.2 ± 0.69 mg L^{-1} h^{-1}, and 28.8 ± 0.64 mg L^{-1} h^{-1}, respectively. In addition, the protonation of g-C_3N_4 is also used to construct the catalyst of composite structure. Protonation can significantly change the charge structure of the surface and give the material some special properties. Bafaqeer and co-workers pretreated g-C_3N_4 with HNO_3 to obtain protonated g-C_3N_4 (PCN) with positive polarity.[185] The g-C_3N_4 and ZnV_2O_6 were combined to form a 2D/2D heterojunction, and PCN was used as an electron transfer mediator and electron trap. Many high-speed charge transfer channels were constructed to transfer electrons from the CB of g-C_3N_4 to the CB of ZnV_2O_6 through PCN (Fig. 15a–c). The experimental results showed that the yield of CH_3OH was 3742 μmol g^{-1} cat^{-1}. Copolymerization is also a good method for the construction of g-C_3N_4-based composites. The specific monomers are integrated into the copolymerized carbon nitride to change the bandgap, composition, and electronic structure of the material. Hayat *et al.*[186] integrated trimesic acid (TMA) into polymeric carbon nitride (PCN) by copolymerization. The integration of TMA effectively promoted the transfer of electrons from the ground state to the excited state in PCN. The photocatalytic performance of the CNU-$TMA_{13.0}$ sample was 16 times that of the blank CNU in all test samples. In conclusion, g-C_3N_4 is an excellent photocatalyst and deserves further study.

5.2.2 Graphene-based photocatalysts. In 2004, Novoselov and Geim successfully separated graphene materials from graphite by micromechanical exfoliation.[24] As the first 2D material to be prepared, graphene materials act as guides in the wide application of 2D materials.[187] Graphene is a honeycomb-shaped carbon atom sheet formed by 2D plane sp^2 hybridization. Graphene has many excellent structural and optoelectronic properties, making it a promising photocatalytic material.[188] Firstly, the large specific surface area of graphene guarantees more active sites, which facilitates the adsorption and activation of CO_2 molecules. Theoretically, the specific surface area of graphene can reach 2630 m^2 g^{-1}.[26] Then, at room temperature, graphene has a high electron transfer rate of 200 000 cm^2 V^{-1} s^{-1}, the excellent conductivity facilitates the migration and transfer of photogenic electrons, thus

19174 | *J. Mater. Chem. A*, 2020, **8**, 19156–19195

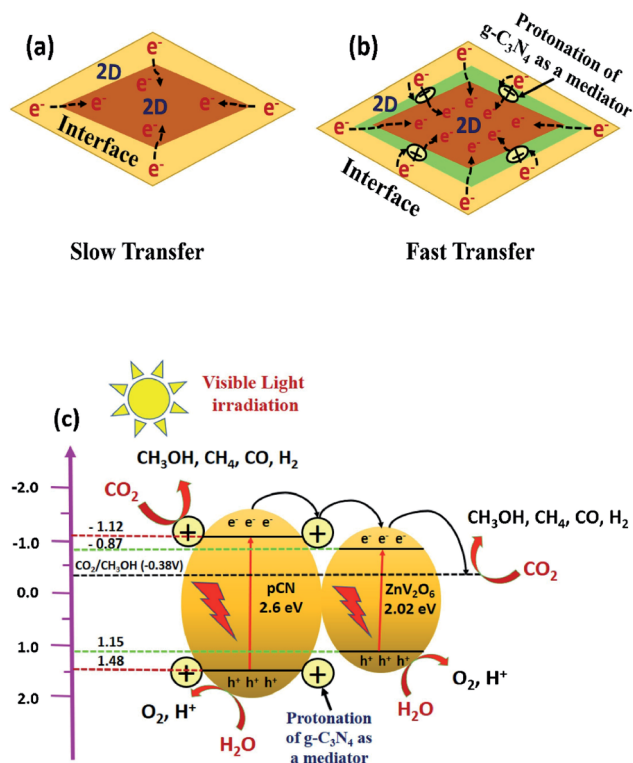This journal is © The Royal Society of Chemistry 2020

Fig. 15 Schematic illustration of contact interfaces for (a) 2D/2D heterojunction, (b) 2D/2D heterojunction with protonation (HNO₃) as a mediator. (c) Schematic diagram of the separation and transfer of photogenerated charges in ZnV₂O₆/PCN composite under visible light irradiation. Reproduced with permission from ref. 185. Copyright 2019 Elsevier.

improving the conductivity of the material. At the same time, rGO retains some functional groups of GO.[193] Recently, there have been some studies on the modification of graphene derivatives. The oxygen-containing functional groups on the GO surface make the material alkaline. Since CO_2 itself has the characteristic of Lewis acidity, the adsorption of CO_2 molecules on the GO surface is greatly promoted. In general, oxygen functional groups are easily modified by nitrogenous substances. Liu and co-workers used ultrasound-assisted method to prepare amine functionalized GO.[194] The amine is nucleophilic and undergoes a strong nucleophilic substitution reaction with the electrophilic CO_2, which greatly increases the adsorption capacity of GO for CO_2 molecules. The optimum adsorption capacity of TEPA-GO was 1.2 mmol g^{-1} at 338 K and 0.1 atm. After 10 cycles, the adsorption capacity of the material decreased by only 1%. In addition, there are also some studies on N-doped GO. Through N doping, GO can have the following advantages: (i) an active region is formed at a position adjacent to a nitrogen atom and a carbon atom; (ii) N atoms can act as anchor centers to adsorb and activate CO_2 molecules; (iii) when GO is coordinated with metal ions, the N atom can act as a connection site.[195] Since GO is a layered structure, the inter-layer spacing is an important factor affecting the properties of materials. Cai et al.[196] incorporated the alkyl diamine molecule into the layer of GO and expanded the intralayer spacing from 0.762 nm to over 1.030 nm (Fig. 16a and b). The results showed that the intralayer spacing of GO directly affected the adsorption performance of CO_2 molecules. When the interlayer spacing was 0.860 nm, the adsorption capacity of the CO_2 molecule was maximized (Fig. 16c).

The composite structure formed by graphene-based materials and other semiconductors is an excellent way to make full use of its properties. Since the Fermi level of graphene (derivatives) is lower than the CB position of most semiconductor materials, graphene and its derivatives tend to act as an electron acceptor in the composite structure. In addition, its excellent conductivity greatly accelerates the transfer of electrons. Liu et al.[197] synthesized the rhombic dodecahedral Cu₂O/rGO, and used it in CO_2 photocatalytic reduction experiments. In this composite system, rGO received photogenerated electrons from the CB of the Cu₂O, then photogenerated electrons were rapidly transferred to the surface of the GO. The yield of methanol was 355.3 μmol g_{cat}^{-1}. Through the study of durability and recyclability, it was found that the photocatalytic performance of the material did not decline significantly after three consecutive tests. Graphene and its derivatives can also act as an electron medium in the construction of heterostructures, facilitating the transfer of electrons between different materials. Meng et al.[198] synthesized ZnO/rGO/UiO-66-NH₂ composite material, in which ZnO and UiO-66-NH₂ formed Z system, and rGO acted as an electronic medium. Electrons were transferred from the CB of ZnO to the VB of UiO-66-NH₂ through rGO, which inhibited the recombination of charge carriers. Graphene and its derivatives have a large specific surface area, making it an ideal carrier material. It is worth noting that the oxygen-containing functional groups on the surface of GO can serve as sites for other semiconductors, thereby uniformly dispersing them on the
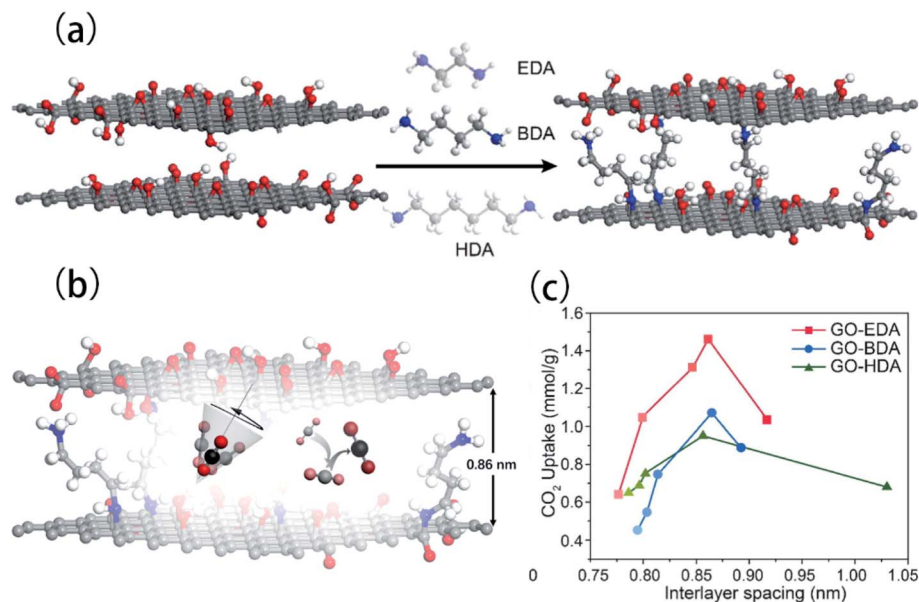
accelerating the bonding of electrons and CO_2 molecules. Next, the thermal conductivity of graphene is about 5000 W m^{-1} K^{-1}, and its good thermal conductivity is beneficial to its photo-thermal effect.[189] However, it is worth noting that, unlike other semiconductor photocatalysts, graphene is difficult to generate photogenerated electrons under photoexcitation due to the lack of bandgap, which limits the application in photocatalysis. In order to overcome this drawback, some derivatives of graphene are developed, such as graphene oxide (GO) and reduced graphene oxide (rGO). These derivative materials have an adjustable bandgap and contain some special surface functional groups, which can be an ideal photocatalytic material.[190] Moreover, the combination of graphene and other semiconductors is also an effective way to overcome the bandgap drawback.

The graphene material is oxidized to obtain GO, which is quite different from graphene. Some defects appear in the crystal structure of GO, forming functional groups such as epoxy groups, hydroxyl groups, and carboxyl groups, etc.[191] When graphene is oxidized, it will convert its zero-gap charac-teristics into semiconductor characteristics, and related exper-iments show that the position of the energy band can be significantly changed by changing the oxidation degree of GO, thereby affecting the bandgap of the semiconductor.[192] In addition, rGO can be obtained by partial reduction of GO, thus

This journal is © The Royal Society of Chemistry 2020

J. Mater. Chem. A, 2020, 8, 19156–19195 | 19175

Fig. 16 (a) Reaction process and structural diagram of 1,4-butanediamine-cross-linked GO. (b) Schematic diagram shows the adsorption of CO_2 molecules between the layers of diamine-cross-linked GO. (c) The effect of interlayer spacing on CO_2 uptake. Reproduced with permission from ref. 196. Copyright 2019 American Chemical Society.

surface of the GO to prevent aggregation. Wang and co-workers successfully constructed α-Fe_2O_3–ZnO/rGO heterojunction.[199] Zn spheres were oxidized to ZnO on the surface of GO and uniformly supported on the surface of GO. This anchoring effect of rGO inhibited the aggregation of Zn spheres, thereby promoting the photocatalytic reaction. Graphene and its derivatives can wrap certain photocatalyst materials, which in turn produce some special effects. For example, Zhao and co-workers synthesized (Pt/TiO_2)@rGO-n composite material.[200] TiO_2 was encapsulated by GO, wherein the surface hydroxyl group and extended π bond of GO could improve the adsorption and activation of CO_2 and H_2O molecules. The photogenerated electrons were transferred from TiO_2 to Pt and then to the rGO surface, which greatly promoted the separation of carriers (Fig. 17). The encapsulation of graphene can be used to inhibit the photocorrosion of materials, thereby increasing the

light stability of the material. Tang et al.[201] prepared rGO/CdS–TiO_2 nanotube materials in which rGO was coated on the surface of CdS. There are two reasons why the photocorrosion of CdS was suppressed: Firstly, due to the barrier effect of rGO, the contact of active radical $\cdot OH$ with CdS was prevented; secondly, an electron-rich microenvironment was generated on the rGO surface, which in turn converted S^- into S^{2-}. Because of its black and zero bandgap characteristics, graphene can absorb almost the whole spectrum of light from ultraviolet to infrared. Graphene cannot generate photogenerated electrons under the excitation of photons, but it can convert the energy of photons into heat energy, thus making the material has a good photothermal effect. Recently, Xu and co-workers specially studied the influence of photothermal effect of graphene on the photoreduction performance of TiO_2.[202] When 30 mg of graphene was introduced, the temperature of the material surface
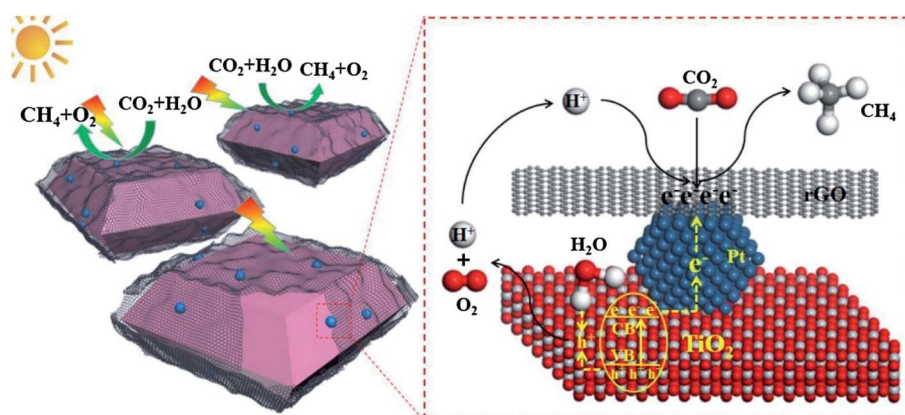

Fig. 17 Schematic of the mechanism for CO_2 photoreduction with H_2O to CH_4 over (Pt/TiO_2) @ rGO-n catalysts. Reproduced with permission from ref. 200. Copyright 2018 Elsevier.

19176 | J. Mater. Chem. A, 2020, 8, 19156–19195

This journal is © The Royal Society of Chemistry 2020

Table 3 Summary of various 2D-related nanomaterials toward CO_2 reduction

	Photocatalyst	Mass (mg)	Light source	Reaction medium	Quantum yield	Performance	Ref.
MXenes-based	Ti_3C_2/Bi_2WO_6	100	300 W Xe lamp	CO_2 and H_2O	—	CH_4: 1.78 μmol g⁻¹ h⁻¹; CH_3OH: 0.44 μmol g⁻¹ h⁻¹	99
	TiO_2/Ti_3C_2	50	300 W Xe lamp	CO_2 and H_2O	—	CH_4: 0.22 μmol h⁻¹	217
	$Ti_3C_2/P25$	—	300 W Xe lamp	CO_2 and H_2O	CO: 0.32%; CH_4: 1.61%	CO: 11.74 μmol g⁻¹ h⁻¹; CH_4: 16.61 μmol g⁻¹ h⁻¹	102
LDHs-based	TiLiAl-LDH	1000	UV lamp	CO_2 and H_2O	—	CH_4: 1.33 mmol g⁻¹ h⁻¹	117
	$MgAl$-LDH/Ag/Ga_2O_3	—	400 W Hg lamp	CO_2 and H_2O	—	CO: 211.7 μmol h⁻¹	218
	NiAl-LDH	10	λ > 600 nm	CO_2 and H_2O (sacrificial reagent: TEOA)	CO + CH_4: 0.95% (AQY)	CH_4: 70.3%	78
	CoZnAl-LDH/RGO/g-C_3N_4	50	300 W Xe lamp	CO_2 and H_2O	CO: 0.45% (AQY)	CO: 10.11 μmol g⁻¹ h⁻¹	219
	0.1Cu_2O@$Zn_{1.8}$Cr-LDH	200	200 W Hg–Xe lamp	CO_2 and H_2O	—	CO: 6.3 μmol after 24 h	122
	P25@CoAl-LDH	50	300 W Xe lamp	CO_2 and H_2O	CO: 0.1% (AQY)	CO: 94%	220
	Fe_3O_4/MgAl-LDH	50	8 W UV lamp	CO_2 and H_2O	—	CO: 442.2 μmol g⁻¹ h⁻¹; CH_4: 223.9 μmol g⁻¹ h⁻¹	123
TMDs-based	g-C_3N_4/NiAl-LDH	50	300 W Xe lamp	CO_2 and H_2O	—	CO: 8.2 μmol g⁻¹ h⁻¹	221
	MoS_2/TiO_2	100	300 W Xe lamp	CO_2 and H_2O	—	CH_3OH: 10.6 μmol g⁻¹ h⁻¹	137
	SiC@MoS_2	—	Visible light (λ ≥ 420 nm)	CO_2 and H_2O	CH_4: 1.75%	CH_4: 323 μL g⁻¹ h⁻¹	222
	TiO_2/MoS_2	—	350 W Xe lamp	CO_2 and H_2O	0.16% (AQY)	CH_4: 2.86 μmol g⁻¹ h⁻¹; CH_3OH: 2.55 μmol g⁻¹ h⁻¹	136
	TiO_2/graphene/MoS_2	—	300 W Xe lamp	CO_2 and H_2O	—	CO: 93.22 μmol g⁻¹ h⁻¹	138
	WSe_2/Graphene/TiO_2	100	500 W Xe lamp	CO_2 and H_2O (sacrificial reagent: Na_2SO_3)	—	CH_3OH: 6.3262 μmol g⁻¹ h⁻¹	142
	MoS_2/Bi_2WO_6	50	300 W Xe lamp	CO_2 and H_2O	—	CH_3OH: 36.7 μmol g$_{cat}$⁻¹; CH_3CH_2OH: 36.6 μmol g$_{cat}$⁻¹	223
g-C_3N_4-based	TiO/g-C_3N_4	3	300 W Xe lamp	CO_2 and H_2O (sacrificial reagent: TEOA)	—	CO: 283.9 μmol g⁻¹ h⁻¹	177
	TiO_{2-x}/g-C_3N_4	5	300 W Xe lamp	CO_2 and H_2O (sacrificial reagent: TEOA)	—	CO: 77.8 μmol g⁻¹ h⁻¹	224
	V_N-g-C_3N_x	5	300 W Xe lamp	CO_2 and H_2O (sacrificial reagent: TEOA)	—	CO: 56.9 μmol g⁻¹ h⁻¹	225
	CN-xGly	20	300 W Xe lamp	CO_2 and H_2O (sacrificial reagent: TEOA)	—	CO: 29.2-fold than pure CN	180
	C, O co-doped polymeric g-C_3N_4	100	300 W Xe lamp	CO_2 and H_2O (sacrificial reagent: TEOA)	—	CH_3OH: 4.18 mmol g⁻¹ in 6 h	183
	NCD/LDH/CN	50	300 W Xe lamp	CO_2 and H_2O	CH_4: 0.62% (AQY)	CH_4: 25.69 μmol g⁻¹ h⁻¹	226
	α-Fe_2O_3/g-C_3N_4	10	300 W Xe lamp	CO_2 and H_2O	—	CH_3OH: 5.63 μmol g⁻¹ h⁻¹	227
	Cu-SCN	25	500 W Xe lamp	CO_2 and H_2O	—		228

This journal is © The Royal Society of Chemistry 2020

J. Mater. Chem. A, 2020, **8**, 19156–19195 | **19177**

Table 3 (*Contd.*)

Photocatalyst		Mass(mg)	Light source	Reaction medium	Quantum yield	Performance	Ref.
	$ZnV_2O_6/g\text{-}C_3N_4$	100	35W HID Xe lamp	CO_2 and H_2O	CH_3OH: 0.21%	Total consumed electron number: 9.47 $\mu mol\ g^{-1}\ h^{-1}$; Slurry system: CH_3OH 3742 $\mu mol\ g_{cat}^{-1}$	185
					CO: 2.8%	Gas phase system: CO 3237 $\mu mol\ g_{cat}^{-1}$	
	$C\text{-}TiO_{2-x}@g\text{-}C_3N_4$	1	300 W Xe lamp	CO_2 and H_2O	—	CO: 12.30 mmol g^{-1} within 60h	229
Graphene-based	$TiO_2/rGO/CeO_2$	150	15W UV-C mercury lamp	CO_2 and H_2O	—	CH_3OH: 641 $\mu mol\ g_{cat}^{-1}\ h^{-1}$; CH_3CH_2OH: 271 $\mu mol\ g_{cat}^{-1}\ h^{-1}$	230
	$\alpha\text{-}Fe_2O_3\text{–}ZnO/rGO$	100	300 W Xe lamp	CO_2 and H_2O	—	CH_3OH: 1.8 $\mu mol\ g^{-1}\ h^{-1}$	199
	Cu_2O/rGO	25	300 W Xe lamp	CO_2 and H_2O	—	CH_3OH: 355.3 $\mu mol\ g_{cat}^{-1}$ after 20 h	197
	$TiO_2\text{–}graphene$	50	300 W Xe lamp	CO_2 and H_2O	—	CH_4: 26.4 $\mu mol\ g^{-1}\ h^{-1}$	202
	$Ag_2CrO_4/Ag/BiFeO_3@RGO$	5	300 W Xe lamp	CO_2 and H_2O	—	CH_4: 180 $\mu mol\ g^{-1}$ after 8h	231
	RGO/TiO_2	5	8 W UV-A lamp	CO_2 and H_2O (sacrificial reagent: TEOA)	—	CH_3OH: 2.33 mmol $g^{-1}\ h^{-1}$	232
	$O\text{-}ZnO/rGO/UiO\text{-}66\text{-}NH_2$	100	300 W Xe lamp	CO_2 and H_2O	—	CH_3OH: 34.83 $\mu mol\ g^{-1}\ h^{-1}$; $HCOOH$: 6.41 $\mu mol\ g^{-1}\ h^{-1}$	198
	$NH_2\text{-}rGO/Al\text{-}PMOF$	50	Visible-light	CO_2 and H_2O (sacrificial reagent: TEOA)	—	$HCOO^-$: 685.6 $\mu mol\ g_{cat}^{-1}\ h^{-1}$	233
	$SnO_2/eo\text{-}GO$	20	450 W Xe lamp	CO_2 and H_2O	—	CH_4: 85 nmol $g_{cat}^{-1}\ h^{-1}$	234
	$(Pt/TiO_2)@rGO$	100	300W Xe lamp	CO_2 and H_2O	CH_4: 1.93% (AQY)	CH_4: 41.3 $\mu mol\ g^{-1}\ h^{-1}$	200
	$NiO/Ni\text{-}G$	50	300W Xe lamp	CO_2 and H_2O	CH_4: 1.98% (AQY)	CH_4: 642 $\mu mol\ g_{Ni}^{-1}\ h^{-1}$	235
	Cu_2O/G	—	300W Xe lamp	CO_2 and H_2O	CH_4: 7.84% (AQY)	CH_4: 14.93 mmol $g_{Cu_2O}^{-1}\ h^{-1}$	236

increased sharply from 58.9 to 116.4 °C under light illumination of 4.38 kW m^{-2}. The experimental results showed that the photothermal effect of graphene promoted the movement speed of CO_2 molecules and carriers on the surface of the material, thereby increasing the yield of CH_4. The yield of CH_4 was 26.7 μmol g^{-1} h^{-1}, which was 5.1 times that of pristine TiO_2. Therefore, modification of graphene derivatives and composite of graphene with other semiconductors are still two important aspects of the current research on the application of graphene in photocatalysis. Further research is worthwhile in order to fully exploit the potential of graphene.

5.2.3 Others. Hexagonal boron nitride (h-BN) is a type of layered 2D photocatalytic material, also known as "white graphene", which has good stability and strong electrical conductivity.[203] But the bandgap of h-BN is 5.5 eV, which needs to be modified properly to be better applied in the field of photocatalysis.[204] Zhao *et al.*[205] synthesized S-doped 2D h-BN nanosheets, which significantly adjusted the bandgap of the material, thereby improving the photocatalytic activity. Chen and co-workers studied the adsorption properties of porous h-BN to CO_2 molecules.[206] They successfully doped C atoms into h-BN materials to produce borocarbonitride (BCN) materials. In the structure of this material, both graphene and h-BN were contained in the structural domain, so it possessed the properties of both materials. The adsorption capacity of BCN for CO_2 was 3.74–3.91 mmol$_{CO_2}$ g^{-1} under the conditions of 298 K and ambient pressure, while the adsorption capacity of the original h-BN was only 1.16–1.66 mmol$_{CO_2}$ g^{-1}. Therefore, their research has certain guiding value for the application of h-BN in the field of photocatalytic reduction of CO_2.

Black phosphorus (BP) nanosheet is also a metal-free emerging 2D photocatalytic material. BP has excellent electrical conductivity, adjustable band gap structure, and a large surface area.[207] The band gap of BP can be effectively adjusted by changing the thickness of the material, and the bandgap range from 0.3 to 2.0 eV.[208,209] Lee and co-workers used BP as a photocatalyst for the first time and applied it to the degradation of pollutants.[210] In the past period of time, research on 2D BP in the field of photocatalysis has mainly focused on photocatalytic hydrogen evolution and pollutants degradation.[211,212] Very recently, some research results on the application of 2D BP in photocatalytic CO_2 reduction have been reported gradually. In these studies, 2D BP was mainly used to form composites with other materials (such as g-C_3N_4, covalent triazine framework, and $CsPbBr_3$), rather than acting as photocatalysis alone for CO_2 reduction reaction.[213–215] The reason for this phenomenon is that 2D BP has some inherent shortcomings. Firstly, the photogenerated electrons and holes of 2D BP are prone to recombination, which greatly reduces the efficiency of photoreduction. Secondly, the lone pair electrons of the P atom in BP can easily react with oxygen, and then the intermediate product will react with water. Therefore, 2D BP is extremely unstable in air and water. Aiming at the stability of 2D BP, Zhu *et al.*[216] used the hydroxyl group to occupy the lone pair electrons of the P atom, thereby effectively inhibiting the reaction between the lone pair electrons and oxygen. In the CO_2 photoreduction experiment, the stable BP nanosheets were

used as the main photocatalyst, which showed excellent photoreduction performance and strong air and water stability. In conclusion, 2D BP still has great research and application potential in the field of photocatalytic CO_2 reduction.

To sum up, it can be seen that there exist many kinds of 2D materials, which show different photocatalytic capabilities and effects in the experiments of photocatalytic reduction of CO_2. Table 3 summarizes the performance of various 2D-related photocatalysts in specific experiments. In addition, different kinds of 2D materials have different structures and photo-electrical properties. The advantages and disadvantages of the main 2D materials are shown in Table 4.

6. Combination of single-atom and 2D nanomaterials for CO_2 photoreduction

In general, decreasing the number of layers of a 2D material will change the electronic structure of the material, such as a decrease in the DOS. Similarly, when the size of a bulk photocatalyst is reduced to the single atom level, the electronic state of the photocatalyst will also change significantly. In 2005, John Meurig Thomas first proposed the concept of single-site heterogeneous catalysts (SSHC), and pointed out the broad prospects of SSHC in the field of catalysis.[237] In 2011, Zhang and co-workers successfully anchored Pt atoms to the surface of iron oxide nanocrystals and used them for CO oxidation.[238] The Pt atom showed extremely high dispersibility on the support, and the catalyst showed excellent stability and selectivity. Since then, the concept of single-atom catalysts (SACs) has gradually emerged in the field of photocatalysis and attracted widespread attention.[239] After relevant experimental research and theoretical calculations, single-atom catalysts can effectively combine the advantages of homogeneous and heterogeneous catalysts, thereby playing the role of homogeneous catalyst analogs.[240] The active atoms in the traditional supported nanoparticle catalysts cannot be completely exposed on the surface of the support material, and the atoms below the surface cannot function, while the single atom catalysts can ensure maximum contact between the active site and the reactants. And theoretically, there are no atoms that touch each other in SACs, thus effectively preventing the accumulation of atoms. These properties make single-atom catalysts effectively distinct from common nanoparticles and elemental doping.

For SACs, to achieve high dispersion and excellent catalytic performance, the development of single-atom carriers will be a key issue. For a suitable carrier, a large specific surface area is indispensable to carry as many active sites as possible. In addition, there must be specific anchor points on the carrier surface, so that single atoms can be firmly loaded. Furthermore, a high electrical conductivity is needed for carrier material, which is conducive to the transfer of electrons.[50] Taking the above factors into consideration, the 2D material is an ideal single-atom support due to its unique geometry and photoelectric structure. The effective combination of 2D materials and single atoms will endow the materials with some unique

This journal is © The Royal Society of Chemistry 2020

J. Mater. Chem. A, 2020, **8**, 19156–19195 | **19179**

Table 4 Structure and performance comparison of common 2D nanomaterials

2D nanomaterials	Band gap (eV)	General formula	Structure	Advantage	Disadvantage
MXenes	0.24–1.8 (functionalized)	$M_{n+1}X_nT_x$	Hexagonal close-packed structure	(i) Excellent stability and mechanical strength; (ii) tunable band structure; (iii) the unique surface termination group.	(i) Preparation method is not mature enough, fluorine-containing etchant is harmful to the environment; (ii) in theory, pristine MXenes are metallic and have no semiconductor properties.
LDHs	2.0–3.4	$[M_{1-x}^{2+}Mx^{3+}(OH)_2]^{x+}[A_{x/n} \cdot H_2O]^{x-}$	Brucite-like layers	(i) The alkaline OH^- groups facilitate the adsorption of CO_2 molecules; (ii) controllability of metal ion components; (iii) tunable interlayer space.	The properties of LDHs depend on its structure and synthesis methods, and better materials synthesis methods need to be proposed.
TMDs	1.0–1.6	MX_2	Sandwiched structure	(i) Excellent chemical stability and conductivity; (ii) TMDs have different phases, materials with different phases have different optoelectronic properties; (iii) there are many groups containing unsaturated and dangling bonds on the edge of the material.	The surface and inner plane of the sheet have low catalytic efficiency, and the high active sites are mainly concentrated at the edge positions.
g-C₃N₄	2.7	—	Tri-s-triazine structure	(i) Low cost and easy preparation; (ii) high chemical and thermal stability; (iii) low toxicity.	(i) Low visible light absorption range; (ii) low surface area; (iii) low photoinduced carrier separation efficiency.
Graphene	Zero-gap	—	Honeycomb-shaped carbon atom sheet	(i) Extremely huge theoretical special surface area and a large number of active sites; (ii) excellent electrical and thermal conductivity; (iii) easily modified, can be oxidized to graphene oxide with good photocatalytic performance.	The characteristic of zero band gap makes it impossible to produce photogenic electrons.

19180 | J. Mater. Chem. A, 2020, 8, 19156–19195

This journal is © The Royal Society of Chemistry 2020

properties.[241] Firstly, single atoms can be fixed in the lattice of 2D materials or connected by covalent bonds, thereby ensuring the stability of the overall structure. Secondly, the single atoms anchored on 2D materials tend to be more coordination unsaturated, while a high proportion of low coordination atoms greatly increases the number of active sites, thereby improving catalytic performance. Thirdly, due to the ultra-thin properties of 2D materials, the open structure on either side is more conducive to the contact of reactants with single atoms, thereby maximizing the utilization of single atoms and greatly reducing the use of materials. Fourthly, single atoms generally show a long-range ordered arrangement on the surface of 2D materials, so that theoretical calculations can play a better role in the study of catalytic performance. Therefore, it will be an excellent platform that combines theoretical calculations and experimental research.[242]

The effective adsorption of single atoms on 2D materials is a prerequisite for the high efficiency of CO_2 photoreduction. Therefore, analyzing the adsorption behavior between single atoms and 2D materials is helpful to the design of high-performance photocatalytic materials. Different single atoms often have different adsorption sites on 2D materials. Tong and co-workers investigated the different adsorption sites of single atom Pt, Pd and Au on the bilayer g-C_3N_4.[243] According to the calculation results of the formation energy, single-atom Pd and Pt were embedded in the interlayer of g-C_3N_4, while single-atom Au was adsorbed on the surface of g-C_3N_4. The Pt atom has vacant 5d orbitals, which could have a strong coordination effect with g-C_3N_4. The partial overlap of the 4d orbital and the 5d orbital of the Pd atom also makes it have a strong bonding ability. The closely packed 5d and 6 s orbitals of Au atoms make them adsorbed only on the surface of g-C_3N_4. Therefore, the adsorption sites of single atom on a two-dimensional material are usually determined by its outer orbital characteristics. In addition to different adsorption sites, there are many different coordination modes between single atom and 2D materials. Firstly, single metal atoms can bond with atoms in a 2D plane through ligands. For example, Gao et al.[244] successfully anchored single atom Co to the surface of partially oxidized graphene. In this process, in addition to electrostatic force and complexation, the oxygen-containing functional groups of partially oxidized graphene also acted as ligands that anchor Co atoms. Secondly, vacancy engineering is an effective method to load single atom. Zhou et al.[245] synthesized g-C_3N_4 with N vacancies and 2H MoS_2 with S vacancies, and analyzed the adsorption properties of the materials to single atoms. Compared with the pristine g-C_3N_4 and 2H MoS_2 surface, they found that the metal atom Ir had a more negative adsorption energy in the N vacancy, and the single atom Rh had a more negative adsorption energy in the S vacancy. The reason for this phenomenon is that the vacancy on the material surface changes the regional electronic structure, which enhances the stability of the single atom load. Thirdly, single atoms can replace atoms in the plane to achieve efficient load. Di and co-workers replaced the Bi atoms in the Bi_3O_4Br nanosheet crystal lattice with a single atom of Co,[246] thus achieving uniform and isolated distribution of Co atoms on 2D materials. In short, the

adsorption behavior of a single atom on 2D material surface is closely related to the electronic structure of both.

The adsorption of single atoms on the 2D material will change some of the original properties of the material. It is very common to change the electronic structure of 2D materials, such as the band position, intermediate energy state and so on. Shi et al.[247] loaded atomic Co on 2D Te nanosheets and analyzed the influence of Co atoms on the electronic structure of Te nanosheets. The introduction of Co atoms caused the valence band minimum of Te nanosheets to shift upwards towards the Fermi level, thus narrowing the band gap of the material. Due to the low orbital level of the atom Co, the orbital hybridization between the Te atom and the Co atom occurred, resulting in an intermediate energy state lower than the CB. The change in the electronic structure of 2D Te enhanced its ability to excite carriers, separate and transfer electrons, thereby improving the efficiency of photocatalysis. Moreover, the interfacial interaction between single atom and the 2D carrier material can result in the structural change of the material. Zhang and co-workers dispersed atom Mo in g-C_3N_4 and studied its effect on the performance of photocatalytic reduction of CO_2.[248] When Mo atoms were introduced into g-C_3N_4, the coordination of atoms in the melon unit and the coordination between adjacent melon units remained unchanged, but the melon unit itself was twisted outward. Therefore, the crystal lattice of the g-C_3N_4 was distorted, and the atomic arrangement appeared disordered, resulting in the transition of g-C_3N_4 from crystalline to amorphous phase. The phase transition increased the surface area of g-C_3N_4 from 13.2 to 61.2–71.3 $m^2\ g^{-1}$. The experimental results showed that the yield of CO was 18 $\mu mol\ g^{-1}\ h^{-1}$, which was 10.6 times higher than the crystal phase g-C_3N_4. Therefore, under certain conditions, the change of 2D material properties caused by single atom load is a favorable factor to improve the performance of CO_2 photoreduction.

The adsorption, activation and conversion process of CO_2 molecules on the surface of the photocatalyst are vital factors that affect the yield and selectivity of the final product. In composite systems composed of single-atom and 2D materials, metal atoms tend to act as active sites for CO_2 reduction. Therefore, in order to achieve rich and controllable reduction products, we must study the adsorption and conversion properties of single atom to CO_2 molecules. In general, the orbital characteristics of a single atom have a great influence on the adsorption of CO_2 molecules. Homlamai et al.[249] used first-principles to analyze the influence of different single atoms (Fe, Co, Ni, and Cu) loaded on g-C_3N_4 on the adsorption of CO_2 molecules. Among all the materials, Fe-g-C_3N_4 showed the most negative CO_2 adsorption energy (-0.40 eV). According to the calculation of partial DOS, it was found that the d orbital of metal atom overlapped with the p orbital of O in CO_2. The d–p orbital overlap between Fe-g-C_3N_4 and CO_2 molecules was the most obvious, which means that a strong bond exists between Fe and O. The electrons transferred from O to the d orbital of Fe atoms caused a strong interaction between CO_2 molecules and the photocatalyst surface, and CO_2 molecules were absorbed stably on the surface of Fe-g-C_3N_4. The other single atoms (Co, Ni, and Cu) and O shown only small d–p overlapping peaks. In

This journal is © The Royal Society of Chemistry 2020

J. Mater. Chem. A, 2020, **8**, 19156–19195 | **19181**

addition, through Perdew–Burke–Ernzerfhof (PBE) functional analysis, it was found that the van der Waals force between the single-atom photocatalyst and the CO_2 molecules had a great effect on the adsorption energy. In the process of CO_2 molecular reduction, the type of single atom will directly affect the conversion of CO_2 molecules, and then change the selectivity of the final product. In each step of CO_2 reduction, the barrier is an effective index to reflect the difficulty of the reduction reaction. Generally speaking, the weaker the adsorption strength between the intermediate and the photocatalyst, the higher the barrier required for the reaction.[250] For single-atom photocatalysts, different electronic structures of atoms lead to different interactions with hydrocarbons, thereby affecting the reaction barriers required for the formation of various intermediates, and showing certain selectivity in the final reduction products. Gao and colleagues loaded single-atom Pd and Pt on g-C_3N_4 for CO_2 photoreduction reaction.[251] The Pt atoms have two uncoupled electrons, so compared to Pd atoms, there is a stronger interaction between the Pt atom and the hydrocarbon. The largest barrier during the formation of CH_3OH on Pd/g-C_3N_4 was 1.46 eV, which was higher than the barrier on Pt/g-C_3N_4 (1.16 eV). For Pd/g-C_3N_4, the largest barrier required to form HCOOH was only 0.66 eV, which was much lower than the largest barrier for the formation of CH_3OH, so Pd/g-C_3N_4 was more inclined to reduce CO_2 to HCOOH. After further theoretical calculations, the formation of CH_4 on Pt/g-C_3N_4 was more

thermodynamically stable. Therefore, when Pt/g-C_3N_4 was used as a photocatalyst, CH_4 was considered to be the final reduction product. In a word, studying the electronic structure of single atom and its interaction with intermediates is an effective way to reveal the selectivity of reduction products.

Single-atom photocatalysts have great application potential, but it is worth noting that there are still some challenges here. For example, 2D materials have a large surface area, but it is difficult for single atom to achieve a uniform load over a large area. The surface energy of metal materials increases sharply with decreasing size, so metal aggregation has always been a major problem for single-atom photocatalysts. In addition, the bond between the single-atom metal site and the 2D material may become unstable as the reaction progresses, thereby affecting the single-atom loading. Therefore, the combination of single-atom photocatalysts and two-dimensional materials still has wide research space in the field of CO_2 photoreduction.

7. Strategies for improving photocatalytic CO_2 reduction activity of 2D nanomaterials

In order to effectively improve the activity of CO_2 photoreduction, the following aspects should be taken into account: (i)

Table 5 Summary of the typical material modification method and its performance improvement

Methods	Classification	Function	Photocatalyst	Performance	Ref.
Elements doping	Metal elements	As the active sites and the electron trap.	MOF-525-Co	CO: 3.13 times higher than pristine MOF-525 CH$_4$: 5.93 times higher than pristine MOF-525	252
	Non-metallic elements	Adjust the energy band structure.	B/g-C_3N_4	CH$_4$: 32 times higher than pristine g-C_3N_4	182
Morphology control	Shape	Expose certain special groups; improve the specific surface.	ZIF-67	CO_2 adsorption capacity: Rhombic dodecahedral morphology: 1.11 mmol g^{-1} Pitaya-like morphology: 0.81 mmol g^{-1} Leaf-like morphology: 1.16 mmol g^{-1}	253
	Thickness	Affects the surface defects and coordination relationships.	Ni–Al LDH	The selectivity of CH$_4$: 27 nm: 0.1%; 5 nm: 2.4%; 1 nm: 16.5%	78
	Facets exposure	Improve the surface energy.	Cu_2O/WO_3-001	CO: 11.7 μmol in 24 h	254
Vacancy engineering	Non-metallic vacancy	Adjust the energy band structure; promote the adsorption and activation of CO_2 molecules; Weaken the exciton-effect.	V_N-g-C_3N_4	CO: 4 times higher than bulk g-C_3N_4	255
	Metallic vacancies	Adjust the electronic structure.	V_{Bi}-BiOBr	CO: 3.8 times higher than pristine BiOBr	256
Heterostructure engineering	0D/2D heterostructure	Promote the separation of photogenic electrons, reduce the carrier recombination rate.	TiO$_{2-x}$/g-C_3N_4	CO: 5 times higher than pristine g-C_3N_4	224
	1D/2D heterostructure	Promote the separation of photogenic electrons, reduce the carrier recombination rate.	CNTs/PCN	CO: 6.6 times higher than pristine g-C_3N_4 CH$_4$: 1.52 times higher than pristine g-C_3N_4	257
	2D/2D heterostructure	Promote the separation of photogenic electrons, reduce the carrier recombination rate.	g-C_3N_4/NiAl-LDH	CO: 5 times and 9 times higher than pristine g-C_3N_4 and NiAl-LDH	221

19182 | J. Mater. Chem. A, 2020, **8**, 19156–19195

This journal is © The Royal Society of Chemistry 2020

rationally adjusting the band structure of the material; (ii) accelerating the migration rate of photogenerated carriers and reducing the recombination rate of charge carriers; (iii) promoting the CO_2 molecular adsorption and activation. In order to achieve these purposes, element doping, morphology control, vacancy engineering and heterostructure engineering are introduced. Table 5 summarizes the typical material modification method and its performance improvement.

7.1 Element doping

Element doping is a very common strategy to improve the photocatalytic performance of 2D materials, which can significantly change the photoelectric properties of materials. It is worth noting that the influence of different doped elements on the properties of materials is different. In general, doped elements can be classified into two types: metal elements and non-metallic elements. The most widely studied metal doping elements are Fe, Na, K, Pt, Co, etc.,[258-263] while common non-metallic doping elements include C, O, B, S, N, etc.[264-269] In addition, the number and location of doping elements are also important factors affecting material properties.[31]

The metal element implanted in the 2D material can generally act as a photocatalytic active site and electronic trap, thereby becoming the central atom of the reaction. Zhang et al.[252] implanted Co atoms into MOF-525. Compared with the pristine MOF-525, the yields of CO (200.6 $\mu mol\ g^{-1}\ h^{-1}$) and CH_4 (36.67 $\mu mol\ g^{-1}\ h^{-1}$) were 3.13 times and 5.93 times that of the previous ones. The unsaturated Co site greatly enhanced the adsorption and activation of CO_2 molecules. In addition, Co site led to the migration of photogenic electrons from porphyrin to Co. Apart from this, the doping of the metal element can also change the selectivity of reduction products. Li and co-workers compared the effects of Au and Cu doped polymeric carbon nitride on the selectivity of CO_2 reduction products.[270] The experimental results showed that the reduction products of Au/CN mainly included CO and CH_3OH, while Cu/CN achieves a high selectivity of CH_4. After analysis, the covalent action between Cu atoms and CN was stronger than that between Au atoms and CN, which was more conducive to the deep reduction of CO_2. However, the electron transfer between the intermediates and Au/CN was weak, which led to the easy desorption of CH_3OH/CO from the material surface, and the reduction products were mainly CH_3OH and CO. What's more, metal doping also improves the light absorption capacity of materials. Tan et al.[271] implanted Ag/Pd alloy into N-doped TiO_2 nanosheets. UV-vis-NIR absorption spectra showed that Ag_xPd_y/TiO_2 photocatalysts greatly enhanced the visible light response. Compared with the absence of CH_4 production of pure TiO_2, the maximum CH_4 yield of Ag_xPd_y/TiO_2 was 79.0 $\mu mol\ g^{-1}\ h^{-1}$.

Non-metallic elements have the advantages of low price and wide sources, so the doping with non-metallic elements tends to be more attractive. Doping of certain nonmetallic elements will affect the electronic system of the material and change the bandgap of the semiconductor material. Huang et al.[272] doped C element into the lattice of g-BN nanosheets to form a ternary B–C–N structure. The DFT theoretical calculation showed that

the indirect bandgap of pristine h-BN was 4.56 eV, and the bandgap of the $B_{11}C_{12}N_9$ was significantly reduced to 2.00 eV, which greatly enhanced the absorption of visible light. It is worth noting that the doping of foreign non-metallic elements will form a new photogenerated carrier recombination center, which will cause additional energy loss.[273] Therefore, self-doping of materials is an effective way to avoid this defect. Huang and co-workers successfully introduced C into the structure of g-C_3N_4 and replaced part of N by self-doping.[274] The doping of C improved the availability of π-electron, and the bandgap of g-C_3N_4 was reduced from 2.75 eV to 2.58 eV. The material showed a good photocatalytic performance under green ($\lambda = 500$ nm) and yellow ($\lambda = 550$ nm) light. Since doping of different elements produces different effects, multi-element co-doping tends to impart a variety of effective properties to the material, and one element can also be used to compensate for defects caused by another element.[275] Samanta et al.[183] co-doped the C and O elements into the polymeric g-C_3N_4. Among them, C doping promoted the separation of charge carriers and increased the electrical conductivity of the material, while the O element expanded the absorption range of light and facilitated the adsorption of CO_2 molecules on the surface. The experimental results showed that the yield of CH_3OH within 6 h was 4.18 mmol g^{-1}.

7.2 Morphology control

In addition to elemental doping, morphology control is an effective method to change the properties of materials. The commonly used morphology control methods for 2D materials mainly include changing the thickness of 2D materials, changing the shape of materials, and controlling the exposed facets. Through morphological control, the electronic structure, active site, and light absorption capacity can be significantly changed.

Constructing different shapes is one of the most common methods for morphology control. By constructing special shapes, it is more conducive to the exposure of certain special groups. For example, the groups containing unsaturated bonds and dangling bonds in TMDs are generally located at the edge of the nanosheet, rather than the surface or the basal planes of the bulk material. Based on this characteristic, photocatalytic performance can be improved by creating more edge positions. Meier et al.[276] successfully synthesized a MoS_2 nanoflower with a large number of edge planar slices by chemical vapor deposition. In the CO_2 photocatalytic reduction experiment, the diameter of nanoflowers increased with the increased of temperature rise rate (Fig. 18d–f). It is worth noting that when the heating rate reached 20 °C min^{-1} (SZF-20), the excessive heating rate would lead to distortion of the crystal structure of the material, thus affecting the absorption of light. At 5 and 10 °C min^{-1} (SZF-5 and SZF-10), the photocatalyst samples had abundant edge site abundance and defect crystal structure, and the activity of the photocatalyst reached the optimal point. By adjusting the shape of the material, the specific surface of the material can be improved; the active site can be increased; the adsorption capacity of the reactant can be enhanced. Low

This journal is © The Royal Society of Chemistry 2020

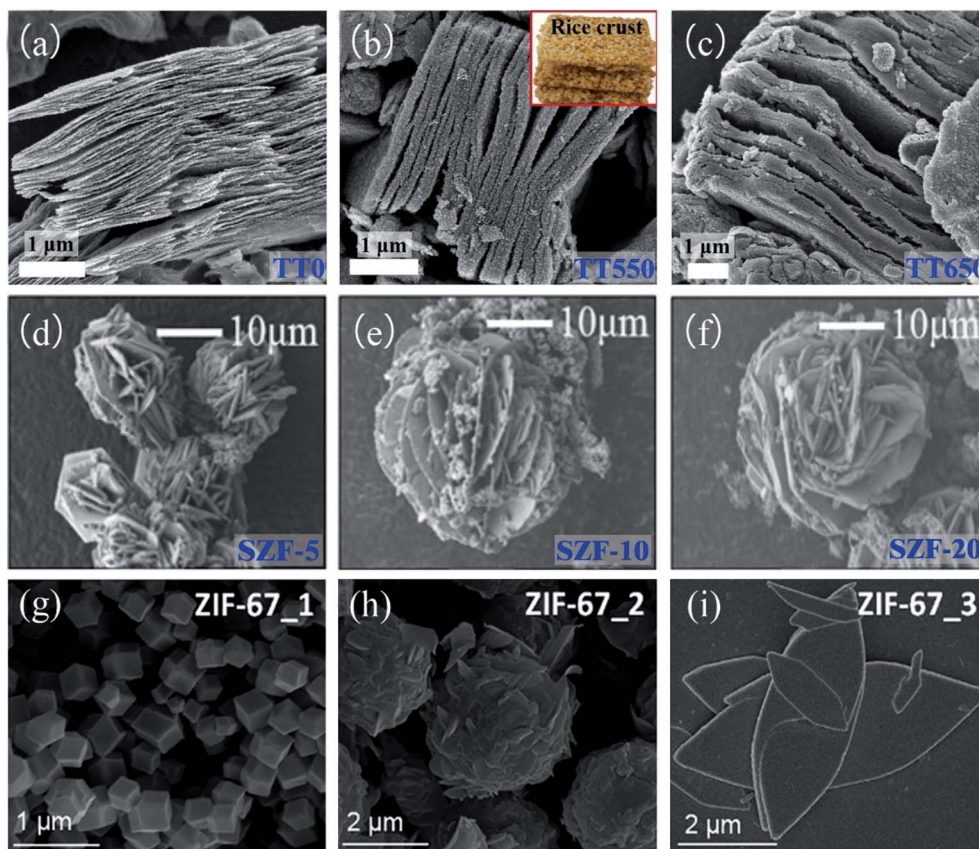*J. Mater. Chem. A*, 2020, **8**, 19156–19195 | **19183**

Fig. 18   Field emission scanning electron microscope (FESEM) images of (a) TT0, (b) TT550 and (c) TT650. Reproduced with permission from ref. 217, copyright 2018 Elsevier. Scanning electron microscope (SEM) images of (d) SZF-5, (e) SZF-7, (f) SZF-20. Reproduced with permission from ref. 276, copyright 2018 American Chemical Society. Scanning electron microscope (SEM) images of (g) ZIF-67_1, (h) ZIF-67_2, and (i) ZIF-67_3. Reproduced with permission from ref. 253, copyright 2018 Royal Society of Chemistry.

et al.[217] loaded TiO_2 nanoparticles onto 2D Ti_3C_2 to form a unique rise crust-like structure by a simple calcination method, and the loading of TiO_2 nanoparticles could be adjusted by controlling the calcination temperature. Fig. 18a–c show dried TiO_2/Ti_3C_2 (TT0), TiO_2/Ti_3C_2 at 550 °C (TT550) and 650 °C (TT650) with a ramping rate of 10 °C min^{-1}, respectively. This unique morphological structure greatly increased the specific surface area of the material, thereby generating more active sites and facilitating the adsorption of CO_2 molecules. The experimental results showed that the optimal CH_4 yield of TiO_2/Ti_3C_2 samples was 2.8 and 3.7 times of pure TiO_2 and P25, respectively. Besides, Wang and co-workers specifically compared the effects of different shapes of MOF materials as co-catalysts on the CO_2 photoreduction performance.[253] The rhombic dodecahedral morphology ZIF-67_1 (Fig. 18g), the pitaya-like morphology ZIF-67_2 (Fig. 18h), and the leaf-like morphology ZIF-67_3 (Fig. 18i) were synthesized by using different volume ratios of CH_3OH and H_2O as solvents. At 100 KPa, ZIF-67_3 had the best adsorption capacity for CO_2, which was 1.16 mmol g^{-1}.

For 2D materials, the thickness is an important factor affecting its properties. The thickness of the material affects the surface defects and coordination relationships. Therefore, thickness control is an important aspect of morphology control.

Tan et al.[78] synthesized a series of Ni–Al LDH with the thickness ranging from 27 nm to 5 nm to 1 nm. Through CO_2 photocatalytic reduction experiments, it was found that the selectivity of H_2 in the product decreased from 43.8% to 26.5% to 13.3%, and the selectivity of methane was increased from 0.1% to 2.4% to 16.5%. Therefore, as the thickness of Ni–Al LDH decreased, the competitive reaction of HER was effectively inhibited, and the selectivity of methane was improved. The main reason for this phenomenon was the increase of the coordination unsaturated metal and hydroxyl defects on the surface of LDH as the thickness decreases.

In parallel, facets exposure is also one of the ways to control morphology. Facets are closely related to the surface energy of the material, and the exposure of high-energy facets can greatly improve the surface energy.[277,278] In general, the low-energy facets of a material tend to dominate in order to keep its stability. For example, Anatase TiO_2 crystals tend to be dominated by the {101} low-energy facets (0.44 J m^{-2}) to maintain thermodynamic stability without exposing {001} high-energy facets (0.90 J m^{-2}).[279] Shi et al.[254] modified WO_3 nanosheets with Cu_2O and studied the effect of WO_3 with or without dominant {001} facets on photocatalytic reduction of CO_2. The analysis showed that the {001} facets of WO_3 promoted the transfer of photogenerated holes to H_2O molecules, which was

19184 | J. Mater. Chem. A, 2020, 8, 19156–19195

This journal is © The Royal Society of Chemistry 2020

beneficial to the oxidation process of H_2O molecules. The maximum CO yield of Cu_2O/WO_3-001 material was 11.7 μmol in 24 h, which was higher than Cu_2O/WO_3 without dominant {001} facets.

7.3 Vacancy engineering

For 2D materials, because the thickness is reduced to the nanometer level, it will lead to the discontinuity of the crystal, and a large number of atoms are exposed on the surface, resulting in atomic vacancies and surface dangling bonds.[280] The introduction of defects can significantly change the physicochemical properties and photoelectric properties of materials, thus promoting their application in the field of photocatalysis. Different kinds of vacancies will have different effects on the material. The types of vacancies can be divided into metal vacancies and non-metal vacancies.[31]

At present, there are many researches on non-metallic vacancy, and it is relatively easy to introduce non-metallic vacancy. Firstly, the energy band structure of the material can be adjusted through the introduction of vacancies. The N vacancy can adjust the band structure by introducing the midgap states. Tu *et al.*[255] calcined bulk g-C_3N_4 from 475 °C to 550 °C under the atmosphere of H_2 to produce g-C_3N_4 nanosheets with different N vacancy densities. With the increased of temperature, C/N gradually increased, indicating the formation of N vacancies (Fig. 19a). Fig. 19b showed that the proportion of C–N=C and N–(C)$_3$ decreased with the increase of temperature, reflecting that the missing N atom may be located at the two-coordinated lattice sites. Through experimental analysis and DFT theoretical calculations, it was found that the introduction of N vacancies led to a midgap state under the CB of g-C_3N_4

(Fig. 19c and d). The photogenerated electrons of the VB would transit to the midgap states, which played a role similar to narrowing the bandgap (Fig. 19c, path 1). The midgap states could also receive electrons from the CB, thereby accelerating the separation of photogenerated electrons and holes (Fig. 19c, path 2). However, as the N vacancies increased, the position of the midgap states would become deeper. When too many N vacancies were introduced, the midgap states would become the recombination site (Fig. 19c, path 3). When the density of N vacancy was optimal, the yield of CO was 4 times higher than the bulk g-C_3N_4. In addition to the adjustment of the energy band structure, the introduction of vacancies will also promote the adsorption and activation of CO_2 molecules. Shen *et al.*[281] introduced C vacancies by heating g-C_3N_4 under NH_3 atmosphere. The experimental and theoretical calculations showed that the CO_2 adsorption energy of sample GCN510 with C vacancies was −0.463 eV, which was more negative than pure GCN (−0.183 eV). Furthermore, the C=O bond length of the CO_2 molecule adsorbed on the surface of the GCN with C vacancies was 1.177 Å, which was greater than the initial C=O bond length (1.169 Å). It can be seen that the C vacancies promoted the adsorption and activation of CO_2 molecules. Moreover, the C vacancies weaken the exciton-effect, which promoted the generation of carriers. The experimental results showed that the yield of CO was 4.18 μmol g^{-1} h^{-1}, which was 2.3 times higher than pristine GCN.

In addition to non-metallic vacancies, metal cation vacancies can also change the electronic structure and physicochemical properties of materials due to the diversity of electronic configurations and orbital distribution.[282] However, it is more difficult to form metal cation vacancies because the formation
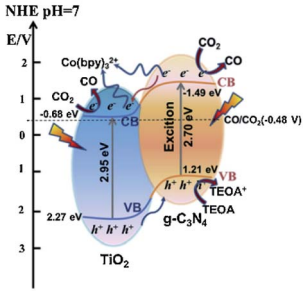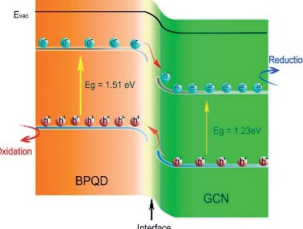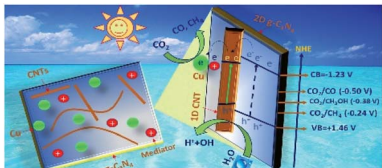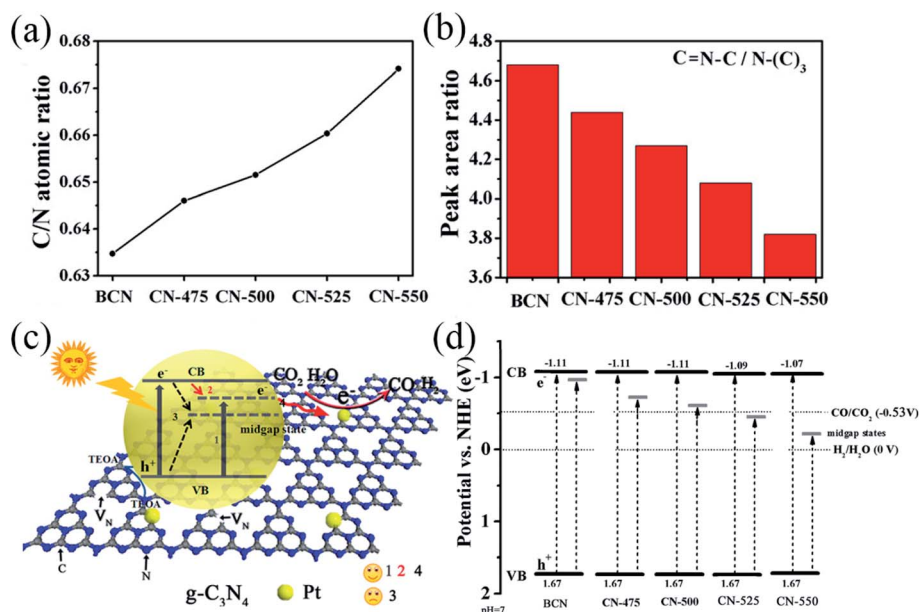

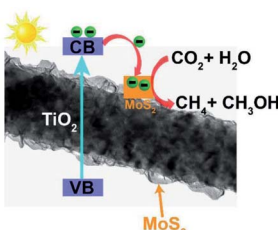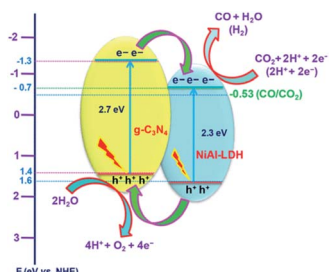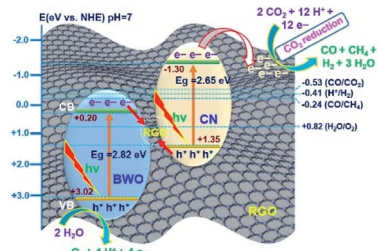**Fig. 19** (a) C/N atomic ratio of BCN and CN-*x* from element analysis. (b) The peak area ratio of C=N–C groups to N–(C)$_3$ of BCN and CN-*x* from XPS analysis. (c) Schematic illustrates the schematic diagram of g-C_3N_4 photocatalytic reduction of CO_2 with N vacancy. The numbers 1, 2, 3, and 4 reflect four paths of electron excitation. (d) Schematic illustration of the electronic structure of BCN and CN-*x*. Reproduced with permission from ref. 255. Copyright 2017 American Chemical Society.

This journal is © The Royal Society of Chemistry 2020

J. Mater. Chem. A, 2020, **8**, 19156–19195 | **19185**

Table 6 List of the synthesis, type and schematic diagram of heterojunction photocatalyst

Classification	Composites	Synthetic methods	Heterojunction type	Schematic diagram	Ref.
0D/2D	TiO$_{2-x}$/g-C$_3$N$_4$	In situ pyrolysis	Conventional type II		224
	BPQD/GCN		Conventional type II		285
1D/2D	CNTs/PCN	Impregnation	Conventional type II		257
	TiO$_2$/MoS$_2$	Hydrothermal	Conventional type II		136
2D/2D	g-C$_3$N$_4$/Ni Al-LDH	Hydrothermal	Conventional type II		221
	Bi$_2$WO$_6$/RGO/g-C$_3$N$_4$	Hydrothermal	Z-scheme		286

energy is relatively large, which leads to relatively little research on cation vacancies. Di and co-workers successfully synthesized BiOBr nanosheets containing Bi vacancies by controlled long carbon chain ionic liquid-assisted synthesis.[256] The introduction of Bi vacancies changed the electronic structure. The density of states (DOS) of BiOBr VB edge with Bi vacancies (V$_{Bi}$-

19186 | J. Mater. Chem. A, 2020, **8**, 19156–19195

This journal is © The Royal Society of Chemistry 2020

BiOBr) was higher, which means that more carriers of V_{Bi}-BiOBr would participate in CO_2 reduction reaction. At the same time, more negative CB gave V_{Bi}-BiOBr a stronger reducibility. The CO temperature programmed desorption (TPD) pattern showed that V_{Bi}-BiOBr has a lower onset CO desorption temperature, and the total amount of CO in the product was 3.8 times that of BiOBr nanosheets. In addition to the introduction of single metal atomic vacancies, Di and co-workers introduced a Bi–O vacancy pair in ultrathin $BiMoO_6$ nanosheets by template-directed method.[283] Similar to the introduction of Bi vacancies in BiOBr, the Bi–O vacancy pair also improved the electronic structure of the material and increased the carrier concentration. In addition, the Bi–O vacancy pair on the surface of the material could serve as a capture center for photogenerated electrons, thereby promoting the separation of photogenerated charge carriers. The results showed that the yield of CO was 3.62 $\mu mol\ g^{-1}\ h^{-1}$. Therefore, whether it is a metal vacancy or a non-metal vacancy, after reasonable setting, it can be an effective means to improve the photoreduction performance of CO_2.

7.4 Heterostructure engineering

Due to the limitation of intrinsic properties, the photocatalytic effect of 2D materials with single components is often unsatisfactory. Therefore, the formation of heterostructure between 2D materials and other materials is an excellent strategy to make up for the shortcomings of single components. In general, conventional heterostructure can be divided into three categories: type-I (straddling gap), type-II (staggered gap), and type-III (broken gap). In recent years, there have been some studies on new p–n heterojunctions and Z-scheme heterojunctions. For 2D materials, they can be divided into 0D/2D (point contact) heterojunctions, 1D/2D (line contact) heterojunctions, and 2D/2D (face contact) heterojunctions according to the different contact methods between different materials (Table 6).[284]

Coupling 0D nanoparticles on the surface of 2D materials is an effective method to construct heterojunction. Shi et al.[224] coupled 0D TiO_2 quantum dots rich in O defects on g-C_3N_4 nanosheets to form a 0D/2D heterojunction (TiO_{2-x}/g-C_3N_4) for CO_2 photoreduction. In this structure, photogenerated electrons were transferred from the CB of g-C_3N_4 to the CB of TiO_2, while the migration direction of photogenerated holes was opposite. Electron transfer occurred on the subpicosecond time scale, which greatly promoted the separation of electrons. The CO yield of TiO_{2-x}/g-C_3N_4 was 77.8 $\mu mol\ g^{-1}\ h^{-1}$, which was 5 times that of the pure g-C_3N_4. Similarly, Kong and co-workers successfully synthesized 0D/2D (BPQD)/g-C_3N_4 type-II heterojunction.[285] Due to the staggered energy bands, the electrons in the CB of BPQD were transferred to the CB of g-C_3N_4, and the holes in the VB of g-C_3N_4 were transferred to the VB of BPQD. This heterojunction reduced the carrier recombination rate and greatly improved the photocatalytic efficiency. However, it is worth noting that the distribution of 0D nanoparticles on the surface of the 2D material is limited, and it is difficult to achieve comprehensive coverage. Such limited contact often fails to give full play to the advantages of heterostructures, so the separation efficiency of photogenerated carriers is limited.

Compared with 0D nanoparticles, 1D materials tend to have larger specific surface area, higher aspect ratio and better carrier mobility.[86] There are some studies on the application of 1D/2D heterojunction in photocatalysis. For example, Tahir et al.[257] used 1D carbon nanotubes (CNTs) to modify 2D protonated g-C_3N_4 (PCN), and then embedded Cu nanoparticles in the structure. The CNTs not only have a large specific surface area and a porous structure, but also have excellent thermal and electrical properties. In this heterostructure, CNTs acted as electron acceptors and received photogenerated electrons from g-C_3N_4. The experimental results showed that the highest CO yield of CNTs/PCN was 410 $\mu mol\ g_{cat}^{-1}\ h^{-1}$, which was 6.6 times that of pure g-C_3N_4, while the yield of CH_4 was 1.52 times that of g-C_3N_4. Moreover, Xu et al.[136] constructed 1D/2D TiO_2/MoS_2 heterojunction by in situ growth of MoS_2 nanosheets on TiO_2 nanofiber. The optimal yields of CH_4 and CH_3OH were 2.86 and 2.55 $\mu mol\ g^{-1}\ h^{-1}$, respectively. When pure TiO_2 nanofibers were used as photocatalysts, the products contained only CH_3OH (0.72 $\mu mol\ g^{-1}\ h^{-1}$). In this structure, electrons tended to transfer from TiO_2 nanofibers to MoS_2 nanosheets. MoS_2 nanosheets increased the surface area of the material, provided more reactive sites, and facilitated the adsorption and activation of CO_2 molecules.

Compared with the above two types of heterojunctions, 2D/2D heterojunctions have stronger physical and electronic coupling due to their relatively larger contact surfaces. There are special studies on the effect of different dimensions of materials on the electron transfer at the heterojunction interface. For example, Sun et al.[287] compared the effects of 0D/2D P25/graphene, 1D/2D TiO_2 nanotubes/graphene, and 2D/2D TiO_2 nanosheets/graphene on photocatalytic performance. Through experimental analysis, the interfacial electron transfer rates on the surface of 0D/2D, 1D/2D, and 2D/2D heterojunction were $1.15 \times 10^8\ s^{-1}$, $3.47 \times 10^8\ s^{-1}$, and $1.06 \times 10^9\ s^{-1}$, respectively. 2D/2D heterojunctions have obvious advantages in terms of electron transfer. Tonda and co-workers synthesized the g-C_3N_4/NiAl-LDH 2D/2D heterostructure by the strong electrostatic interaction.[221] Through VB-XPS, it was shown that the minimum CB value of NiAl-LDH was lower than g-C_3N_4, while the maximum VB value of g-C_3N_4 was higher than NiAl-LDH. The photogenerated electrons were transferred from the CB of g-C_3N_4 to the CB of NiAl-LDH, while the holes formed on the VB of NiAl-LDH could enter the VB of g-C_3N_4. When the content of NiAl-LDH was 10%, the yield of CO reached a maximum of 8.2 $\mu mol\ g^{-1}\ h^{-1}$. Moreover, in order to further promote the photocatalytic properties of materials, the formation of heterojunction by combination of three materials is also a method of material design. Jo et al.[286] successfully synthesized Bi_2WO_6/RGO/g-C_3N_4 (BRC) 2D/2D/2D heterojunction through the two-step hydrothermal method (Fig. 20a–e). It is worth noting that, unlike traditional heterojunctions, Z-scheme heterojunctions were formed between Bi_2WO_6 and g-C_3N_4. The photogenetic electrons in the CB of Bi_2WO_6 were transferred to the VB of g-C_3N_4 through RGO, so that the oxidation and reduction sites were spatially separated. The redox reactions occurred in the VB of Bi_2WO_6 and the CB of g-C_3N_4, respectively. RGO acted as both a carrier and a medium for electron transfer, facilitating

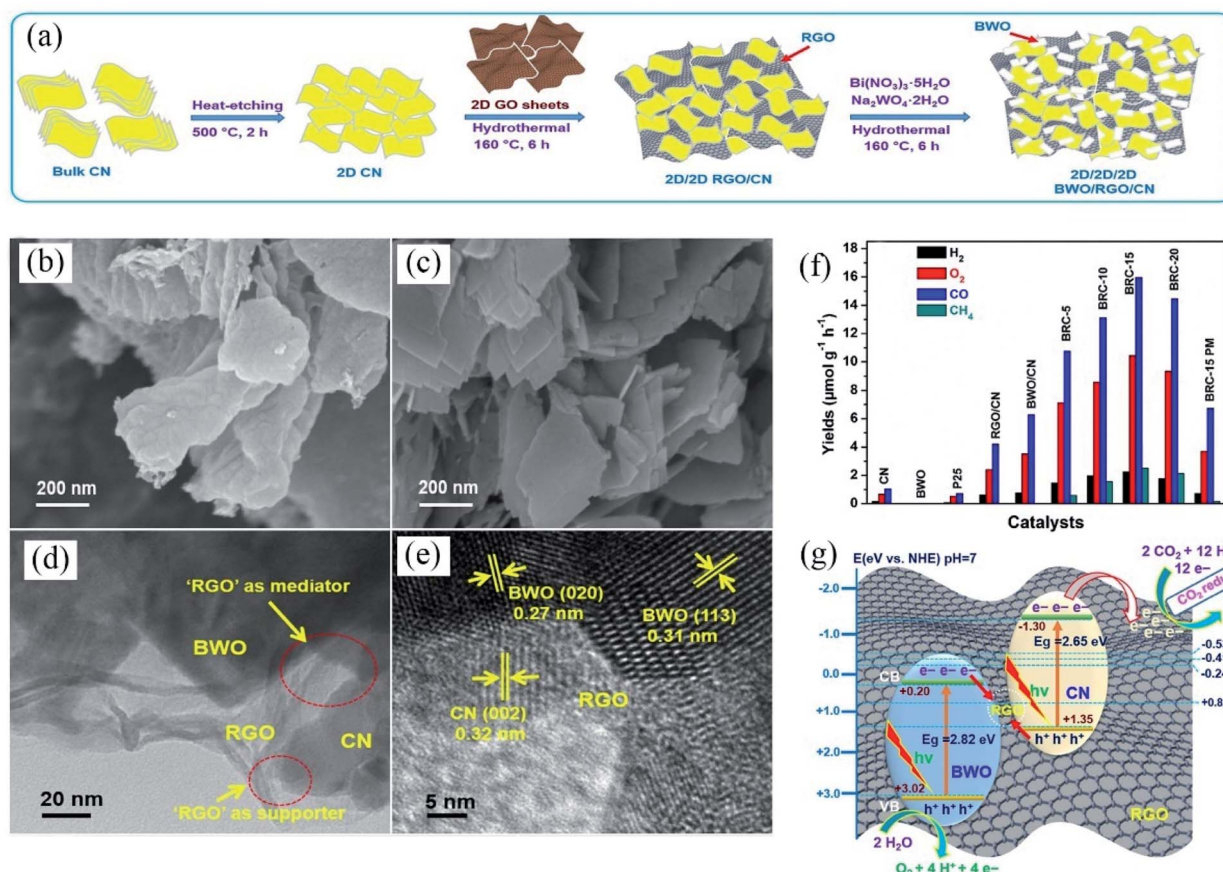This journal is © The Royal Society of Chemistry 2020

J. Mater. Chem. A, 2020, **8**, 19156–19195 | **19187**

Fig. 20 (a) Schematic diagram of synthesis process of Bi_2WO_6/RGO/g-C_3N_4 heterojunction. (b) and (c) SEM images of BRC-15 samples. (d) and (e) HR-TEM images of the BRC-15 samples. (f) The bar chart reflects the comparison of the yield of H_2, O_2, CO, and CH_4 after 5 h of visible light illumination. (g) Schematic diagram reflects the mechanism of photocatalytic reduction of CO_2 by Bi_2WO_6/RGO/g-C_3N_4. Reproduced with permission from ref. 286. Copyright 2018 Elsevier.

the transfer of electrons between semiconductor materials (Fig. 20g). When the content of RGO and Bi_2WO_6 in the material was 1 wt% and 15 wt%, respectively, the yield of CO reached a maximum value of 15.96 μmol g^{-1} h^{-1}, which was 15 times that of pristine g-C_3N_4, and the maximum yield of CH_4 was 2.51 μmol g^{-1} h^{-1} (Fig. 20f).

8. Conclusions and perspectives

Because sufficient clean solar exists to power energy for photocatalysis, further research on the photocatalytic reduction of CO_2 represents a firm grasp of the opportunity that executes solutions to CO_2 pollution and energy issues. Among photocatalysts, 2D materials are a unique category, and have been favored by researchers for their remarkable optoelectronic and structural properties. In this review, recent advances in two-dimensional materials for CO_2 photoreduction and related principles are described in detail. Despite considerable achievements have been made over the past few years, further research is needed to realize the large-scale application of 2D materials in the photocatalytic CO_2 conversion to achieve a sustainable future.

The C atom in CO_2 is in the highest valence state, which means that CO_2 molecules will produce many different

products during the reduction process. There are many factors that affect the product selectivity, including the adsorption and activation of CO_2, photoexcitation properties, the bandgap structure, the reaction sites on the surface, the adsorption and desorption of intermediates, *etc.* The involvement of many factors has led to extremely complicated control of product selectivity. In recent years, many measures have been taken to increase the selectivity of products, but the overall effect has been poor. Lack of a relatively complete product analysis system is a key obstacle to the study of product selectivity. Currently, CO, CH_4, and H_2 are mainly detected in CO_2 reaction products, while some liquid products and multi-carbon products are more difficult to detect, such as CH_3OH, HCOOH, CH_3CH_2OH, CH_3CH_2CHO, *etc.* They are significant for studying the reduction pathways and selectivity. Only by analyzing all the reduced products, including those with a low concentration, can we further explore the mechanism of CO_2 photocatalysis, which is conducive to improving the yield of target products.

In the course of experimental research, the yield of reduced products can generally reach a few μmol g^{-1} h^{-1}, so the yield is difficult to meet the requirements in practical applications. At the same time, there is a gap between the concentration of CO_2 used in many experimental studies and the actual atmosphere.

The concentration of CO_2 in the atmosphere is lower than that in the experiment, so the prepared photocatalyst is generally difficult to achieve the desired effect under the condition of low concentration of CO_2. Therefore, improving the reduction yield of the product should be a continuously pursued goal.

Ultrathin thickness is a typical and distinct feature of 2D materials, reducing the thickness can increase the specific surface area, reduce the migration distance of photogenerated carriers, and increase the elastic strain tolerance. However, the quantum confinement effect of the ultrathin structure will reduce the visible light absorption range and increase the carrier recombination rate. Therefore, the best photocatalytic performance can be obtained only when the thickness of 2D materials is suitable. The experiment of photocatalytic reduction of CO_2 by 2D materials with different thickness is the next step to explore this problem.

The durability and recyclability of 2D materials is important if any wide, realistic application is envisaged. In the laboratory, we can prepare 2D photocatalysts with a certain morphological structure, but in practical commercial or industrial applications, it is very difficult to prepare 2D materials with high purity and controllable uniform morphology and size. At present, chemical vapor deposition (CVD) and high vacuum deposition are two commonly used methods to prepare 2D materials, but both have drawbacks of low yield and high cost. As a relatively new method, liquid phase stripping often results in relatively poor product quality. Therefore, the recycling of materials is an important means to reduce costs, and the research on material preparation method is still a long way.

Some advanced *in situ* and *ex situ* characterization techniques should be applied to the development and application of 2D materials. Through characterization technology, the morphology, defects, and active sites of materials can be effectively analyzed, so as to study the relationship between structure and properties. For example, near atomic scale photocatalysts can be studied by high-angle annular dark field scanning TEM (HAADF-STEM) to investigate the distribution of atoms on 2D material surfaces. X-ray absorption near-edge structure (XANES) can be used to explore the defects and strains of materials. Extended X-ray absorption fine structure (EXAFS) is a common characterization technology for detecting structural information of photocatalytic materials, especially for photocatalysts containing single atoms or clusters. Electron spin resonance (ESR) is a strong method for detection of active free radicals on the surface of photocatalysts. Femtosecond transient absorption (TA) spectroscopy can be used to study the electron–hole recombination kinetics of semiconductors. X-ray photoelectron spectroscopy (XPS) using a synchrotron light source is a powerful tool to inspect the photoinduced carrier transfer. At present, advanced characterization is an effective method to study reaction intermediates, which provides a good method to study reaction mechanism and product selectivity.

In summary, the generation of hydrocarbons from CO_2 by employing the 2D photocatalysts and solar as the energy input will be a promising technology. Progress in synthesis and modification methods for the 2D materials coupled with a more in-depth understanding of CO_2 photoreduction mechanisms has enabled the rational design of photocatalyst with excellent activity and selectivity. But the current research is only at the experimental level, there are still huge challenges to achieve large-scale applications. We are confident that the constant progress in 2D materials synthesis, modification, characterization, and mechanism analysis is laying the groundwork for CO_2 pollution control as well as energy conversion.

Conflicts of interest

There are no conflicts to declare.

Acknowledgements

References

1 K. Li, X. An, K. H. Park, M. Khraisheh and J. Tang, *Catal. Today*, 2014, **224**, 3–12.

2 C. Hepburn, E. Adlen, J. Beddington, E. A. Carter, S. Fuss, N. Mac Dowell, J. C. Minx, P. Smith and C. K. Williams, *Nature*, 2019, **575**, 87–97.

3 C. Zhang, G. Zeng, D. Huang, C. Lai, M. Chen, M. Cheng, W. Tang, L. Tang, H. Dong and B. Huang, *Chem. Eng. J.*, 2019, **373**, 902–922.

4 B. P. Spigarelli and S. K. Kawatra, *J. CO$_2$ Util.*, 2013, **1**, 69–87.

5 J. Wu, Y. Huang, W. Ye and Y. Li, *Adv. Sci.*, 2017, **4**, 1700194.

6 F. M. Mota and D. H. Kim, *Chem. Soc. Rev.*, 2019, **48**, 205–259.

7 Q. Wang, Y. Lei, D. Wang and Y. Li, *Energy Environ. Sci.*, 2019, **12**, 1730–1750.

8 R. M. Evans, B. Siritanaratkul, C. F. Megarity, K. Pandey, T. F. Esterle, S. Badiani and F. A. Armstrong, *Chem. Soc. Rev.*, 2019, **48**, 2039–2052.

9 X. Li, J. Yu, M. Jaroniec and X. Chen, *Chem. Rev.*, 2019, **119**, 3962–4179.

10 J. Shi, Y. Jiang, Z. Jiang, X. Wang, X. Wang, S. Zhang, P. Han and C. Yang, *Chem. Soc. Rev.*, 2015, **44**, 5981–6000.

11 F. P. García de Arquer, C.-T. Dinh, A. Ozden, J. Wicks, C. McCallum, A. R. Kirmani, D.-H. Nam, C. Gabardo, A. Seifitokaldani, X. Wang, Y. C. Li, F. Li, J. Edwards, L. J. Richter, S. J. Thorpe, D. Sinton and E. H. Sargent, *Science*, 2020, **367**, 661–666.

This journal is © The Royal Society of Chemistry 2020

J. Mater. Chem. A, 2020, **8**, 19156–19195 | **19189**

12 M. Liras, M. Barawi and A. Víctor, *Chem. Soc. Rev.*, 2019, **48**, 5454–5487.

13 Y. Zhou, W. Wang, C. Zhang, D. Huang, C. Lai, M. Cheng, L. Qin, Y. Yang, C. Zhou, B. Li, H. Luo and D. He, *Adv. Colloid Interface Sci.*, 2020, **279**, 102144.

14 C. Zhang, C. Lai, G. Zeng, D. Huang, C. Yang, Y. Wang, Y. Zhou and M. Cheng, *Water Res.*, 2016, **95**, 103–112.

15 F. Qin, Y. Peng, G. Song, Q. Fang, R. Wang, C. Zhang, G. Zeng, D. Huang, C. Lai, Y. Zhou, X. Tan, M. Cheng and S. Liu, *J. Hazard. Mater.*, 2020, **398**, 122816.

16 T. Inoue, A. Fujishima, S. Konishi and K. Honda, *Nature*, 1979, **277**, 637–638.

17 A. Meng, L. Zhang, B. Cheng and J. Yu, *Adv. Mater.*, 2019, **31**, 1807660.

18 M. Wang, J. Iocozzia, L. Sun, C. Lin and Z. Lin, *Energy Environ. Sci.*, 2017, **10**, 2041.

19 X. Li, J.-L. Shi, H. Hao and X. Lang, *Appl. Catal., B*, 2018, **232**, 260–267.

20 X. Li, P. Xu, M. Chen, G. Zeng, D. Wang, F. Chen, W. Tang, C. Chen, C. Zhang and X. Tan, *Chem. Eng. J.*, 2019, **366**, 339–357.

21 P. Zhou, Q. Zhang, Z. Xu, Q. Shang, L. Wang, Y. Chao, Y. Li, H. Chen, F. Lv and Q. Zhang, *Adv. Mater.*, 2020, **32**, 1904249.

22 A. Di Mauro, M. Cantarella, G. Nicotra, V. Privitera and G. Impellizzeri, *Appl. Catal., B*, 2016, **196**, 68–76.

23 B. Shao, X. Liu, Z. Liu, G. Zeng, W. Zhang, Q. Liang, Y. Liu, Q. He, X. Yuan and D. Wang, *Chem. Eng. J.*, 2019, **374**, 479–493.

24 K. S. Novoselov, A. K. Geim, S. V. Morozov, D. Jiang, Y. Zhang, S. V. Dubonos, I. V. Grigorieva and A. A. Firsov, *Science*, 2004, **306**, 666–669.

25 Y. Wang, M. Qiu, M. Won, E. Jung, T. Fan, N. Xie, S.-G. Chi, H. Zhang and J. S. Kim, *Coord. Chem. Rev.*, 2019, **400**, 213041.

26 M. D. Stoller, S. Park, Y. Zhu, J. An and R. S. Ruoff, *Nano Lett.*, 2008, **8**, 3498–3502.

27 J. Fu, B. Zhu, C. Jiang, B. Cheng, W. You and J. Yu, *Small*, 2017, **13**, 1603938.

28 G. Liu, C. Zhen, Y. Kang, L. Wang and H.-M. Cheng, *Chem. Soc. Rev.*, 2018, **47**, 6410–6444.

29 J. Pang, R. G. Mendes, A. Bachmatiuk, L. Zhao, H. Q. Ta, T. Gemming, H. Liu, Z. Liu and M. H. Rummeli, *Chem. Soc. Rev.*, 2019, **48**, 72–133.

30 X. Chang, T. Wang and J. Gong, *Energy Environ. Sci.*, 2016, **9**, 2177–2196.

31 J. Xiong, P. Song, J. Di and H. Li, *Appl. Catal., B*, 2019, **256**, 117788.

32 Z. Sun, N. Talreja, H. Tao, J. Texter, M. Muhler, J. Strunk and J. Chen, *Angew. Chem., Int. Ed.*, 2018, **57**, 7610–7627.

33 Y. Chen, G. Jia, Y. Hu, G. Fan, Y. H. Tsang, Z. Li and Z. Zou, *Sustainable Energy Fuels*, 2017, **1**, 1875–1898.

34 M. Marszewski, S. Cao, J. Yu and M. Jaroniec, *Mater. Horiz.*, 2015, **2**, 261–278.

35 P. S. Surdhar, S. P. Mezyk and D. A. Armstrong, *J. Phys. Chem.*, 1989, **93**, 3360–3363.

36 S. Yu, X.-B. Fan, X. Wang, J. Li, Q. Zhang, A. Xia, S. Wei, L.-Z. Wu, Y. Zhou and G. R. Patzke, *Nat. Commun.*, 2018, **9**, 1–10.

37 A. Sandhu, *Nat. Nanotechnol.*, 2006, DOI: 10.1038/nnano.2006.21.

38 M.-P. Jiang, K.-K. Huang, J.-H. Liu, D. Wang, Y. Wang, X. Wang, Z.-D. Li, X.-Y. Wang, Z.-B. Geng, X.-Y. Hou and S.-H. Feng, *Chem*, 2020, **6**, 2335–2346.

39 S.-C. Lin, C.-C. Chang, S.-Y. Chiu, H.-T. Pai, T.-Y. Liao, C.-S. Hsu, W.-H. Chiang, M.-K. Tsai and H. M. Chen, *Nat. Commun.*, 2020, **11**, 3525.

40 S. Xu and E. A. Carter, *Chem. Rev.*, 2018, **119**, 6631–6669.

41 S. Kattel, P. Liu and J. G. Chen, *J. Am. Chem. Soc.*, 2017, **139**, 9739–9754.

42 M. J. L. Ginés, A. J. Marchi and C. R. Apesteguía, *Appl. Catal., A*, 1997, **154**, 155–171.

43 L. K. Rihko-Struckmann, A. Peschel, R. Hanke-Rauschenbach and K. Sundmacher, *Ind. Eng. Chem. Res.*, 2010, **49**, 11073–11078.

44 D. Pakhare and J. Spivey, *Chem. Soc. Rev.*, 2014, **43**, 7813–7837.

45 F. Wang, M. Wei, D. G. Evans and X. Duan, *J. Mater. Chem. A*, 2016, **4**, 5773–5783.

46 M. Khalil, J. Gunlazuardi, T. A. Ivandini and A. Umar, *Renewable Sustainable Energy Rev.*, 2019, **113**, 109246.

47 Y. Wang, D. He, H. Chen and D. Wang, *J. Photochem. Photobiol., C*, 2019, **40**, 117–149.

48 Z. Fu, Q. Yang, Z. Liu, F. Chen, F. Yao, T. Xie, Y. Zhong, D. Wang, J. Li and X. Li, *J. CO_2 Util.*, 2019, **34**, 63–73.

49 W. Fan, Q. Zhang and Y. Wang, *Phys. Chem. Chem. Phys.*, 2013, **15**, 2632–2649.

50 L. Wang, W. Chen, D. Zhang, Y. Du, R. Amal, S. Qiao, J. Wu and Z. Yin, *Chem. Soc. Rev.*, 2019, **48**, 5310–5349.

51 S. H. Yoon, U. Kang, H. Park, A. Abdel-Wahab and D. S. Han, *Catal. Today*, 2019, **335**, 345–353.

52 S. Zhang, P. Kang and T. J. Meyer, *J. Am. Chem. Soc.*, 2014, **136**, 1734–1737.

53 R. Kortlever, J. Shen, K. J. P. Schouten, F. Calle-Vallejo and M. T. Koper, *J. Phys. Chem. Lett.*, 2015, **6**, 4073–4082.

54 M. F. Baruch, J. E. Pander III, J. L. White and A. B. Bocarsly, *ACS Catal.*, 2015, **5**, 3148–3156.

55 Z. Sun, T. Ma, H. Tao, Q. Fan and B. Han, *Chem*, 2017, **3**, 560–587.

56 X. Nie, M. R. Esopi, M. J. Janik and A. Asthagiri, *Angew. Chem., Int. Ed.*, 2013, **52**, 2459–2462.

57 A. A. Peterson, F. Abild-Pedersen, F. Studt, J. Rossmeisl and J. K. Nørskov, *Energy Environ. Sci.*, 2010, **3**, 1311–1315.

58 S. N. Habisreutinger, L. Schmidt-Mende and J. K. Stolarczyk, *Angew. Chem., Int. Ed.*, 2013, **52**, 7372–7408.

59 W. Ju, A. Bagger, X. Wang, Y. Tsai, F. Luo, T. F. Möller, H. Wang, J. Rossmeisl, A. S. Varela and P. Strasser, *ACS Energy Lett.*, 2019, **4**, 1663–1671.

60 X. Li, Y. Sun, J. Xu, Y. Shao, J. Wu, X. Xu, Y. Pan, H. Ju, J. Zhu and Y. Xie, *Nat. Energy*, 2019, **4**, 690–699.

61 A. J. Garza, A. T. Bell and M. Head-Gordon, *ACS Catal.*, 2018, **8**, 1490–1499.

19190 | *J. Mater. Chem. A*, 2020, **8**, 19156–19195

This journal is © The Royal Society of Chemistry 2020

62 Y. Hori, R. Takahashi, Y. Yoshinami and A. Murata, *J. Phys. Chem. B*, 1997, **101**, 7075–7081.

63 K. D. Yang, C. W. Lee, K. Jin, S. W. Im and K. T. Nam, *J. Phys. Chem. Lett.*, 2017, **8**, 538–545.

64 J. Fu, K. Jiang, X. Qiu, J. Yu and M. Liu, *Mater. Today*, 2020, **32**, 222–243.

65 S. Yu, A. J. Wilson, G. Kumari, X. Zhang and P. K. Jain, *ACS Energy Lett.*, 2017, **2**, 2058–2070.

66 S. Yu, A. J. Wilson, J. Heo and P. K. Jain, *Nano Lett.*, 2018, **18**, 2189–2194.

67 S. Zeng, E. Vahidzadeh, C. G. VanEssen, P. Kar, R. Kisslinger, A. Goswami, Y. Zhang, N. Mahdi, S. Riddell, A. E. Kobryn, S. Gusarov, P. Kumar and K. Shankar, *Appl. Catal., B*, 2020, **267**, 118644.

68 A. Li, T. Wang, C. Li, Z. Huang, Z. Luo and J. Gong, *Angew. Chem., Int. Ed.*, 2019, **58**, 3804–3808.

69 M. Xing, Y. Zhou, C. Dong, L. Cai, L. Zeng, B. Shen, L. Pan, C. Dong, Y. Chai, J. Zhang and Y. Yin, *Nano Lett.*, 2018, **18**, 3384–3390.

70 X. Wang, Y. Wang, M. Gao, J. Shen, X. Pu, Z. Zhang, H. Lin and X. Wang, *Appl. Catal., B*, 2020, **270**, 118876.

71 S. Feng, J. Zhao, Y. Bai, X. Liang, T. Wang and C. Wang, *J. CO₂ Util.*, 2020, **38**, 1–9.

72 K. Wang, Z. Fang, X. Huang, W. Feng, Y. Wang, B. Wang and P. Liu, *Chem. Commun.*, 2017, **53**, 9765–9768.

73 L. Zhao, F. Ye, D. Wang, X. Cai, C. Meng, H. Xie, J. Zhang and S. Bai, *ChemSusChem*, 2018, **11**, 3524–3533.

74 Y. Wang, J. Zhao, Y. Li and C. Wang, *Appl. Catal., B*, 2018, **226**, 544–553.

75 A. Li, Q. Cao, G. Zhou, B. V. K. J. Schmidt, W. Zhu, X. Yuan, H. Huo, J. Gong and M. Antonietti, *Angew. Chem., Int. Ed.*, 2019, **58**, 14549–14555.

76 X. Yang, S. Wang, N. Yang, W. Zhou, P. Wang, K. Jiang, S. Li, H. Song, X. Ding, H. Chen and J. Ye, *Appl. Catal., B*, 2019, **259**, 118088.

77 Z. Liu, Z. Wang, S. Qing, N. Xue, S. Jia, L. Zhang, L. Li, N. Li, L. Shi and J. Chen, *Appl. Catal., B*, 2018, **232**, 86–92.

78 L. Tan, S.-M. Xu, Z. Wang, Y. Xu, X. Wang, X. Hao, S. Bai, C. Ning, Y. Wang, W. Zhang, Y. K. Jo, S.-J. Hwang, X. Cao, X. Zheng, H. Yan, Y. Zhao, H. Duan and Y.-F. Song, *Angew. Chem., Int. Ed.*, 2019, **58**, 11860–11867.

79 T. Ouyang, H.-H. Huang, J.-W. Wang, D.-C. Zhong and T.-B. Lu, *Angew. Chem., Int. Ed.*, 2017, **56**, 738–743.

80 P. Hohenberg and W. Kohn, *Phys. Rev.*, 1964, **136**, B864.

81 Y. Wang, Y. Tian, L. Yan and Z. Su, *J. Phys. Chem. C*, 2018, **122**, 7712–7719.

82 X. Yang, S. Wang, N. Yang, W. Zhou, P. Wang, K. Jiang, S. Li, H. Song, X. Ding and H. Chen, *Appl. Catal., B*, 2019, **259**, 118088.

83 W. Chen, B. Han, C. Tian, X. Liu, S. Liang, H. Deng and Z. Lin, *Appl. Catal., B*, 2019, **244**, 996–1003.

84 S. S. Tafreshi, A. Z. Moshfegh and N. H. de Leeuw, *J. Phys. Chem. C*, 2019, **123**, 22191–22201.

85 M. Lu, J. Liu, Q. Li, M. Zhang, M. Liu, J. L. Wang, D. Q. Yuan and Y. Q. Lan, *Angew. Chem., Int. Ed.*, 2019, **131**, 12392–12397.

86 A. Hasani, M. Tekalgne, Q. Van Le, H. W. Jang and S. Y. Kim, *J. Mater. Chem. A*, 2019, **7**, 430–454.

87 M. Naguib, M. Kurtoglu, V. Presser, J. Lu, J. Niu, M. Heon, L. Hultman, Y. Gogotsi and M. W. Barsoum, *Adv. Mater.*, 2011, **23**, 4248–4253.

88 X. Li, C. Wang, Y. Cao and G. Wang, *Chem. – Asian J.*, 2018, **13**, 2742–2757.

89 Y. Yang, Z. Zeng, G. Zeng, D. Huang, R. Xiao, C. Zhang, C. Zhou, W. Xiong, W. Wang and M. Cheng, *Appl. Catal., B*, 2019, **258**, 117956.

90 P. Srivastava, A. Mishra, H. Mizuseki, K.-R. Lee and A. K. Singh, *ACS Appl. Mater. Interfaces*, 2016, **8**, 24256–24264.

91 C. Peng, P. Wei, X. Li, Y. Liu, Y. Cao, H. Wang, H. Yu, F. Peng, L. Zhang and B. Zhang, *Nano energy*, 2018, **53**, 97–107.

92 X. Zhang, Z. Zhang, J. Li, X. Zhao, D. Wu and Z. Zhou, *J. Mater. Chem. A*, 2017, **5**, 12899–12903.

93 T. Cai, L. Wang, Y. Liu, S. Zhang, W. Dong, H. Chen, X. Yi, J. Yuan, X. Xia and C. Liu, *Appl. Catal., B*, 2018, **239**, 545–554.

94 H. Huang, Y. Song, N. Li, D. Chen, Q. Xu, H. Li, J. He and J. Lu, *Appl. Catal., B*, 2019, **251**, 154–161.

95 T. Su, Z. D. Hood, M. Naguib, L. Bai, S. Luo, C. M. Rouleau, I. N. Ivanov, H. Ji, Z. Qin and Z. Wu, *Nanoscale*, 2019, **11**, 8138–8149.

96 B. Wang, A. Zhou, F. Liu, J. Cao, L. Wang and Q. Hu, *J. Adv. Ceram.*, 2018, **7**, 237–245.

97 J. Peng, X. Chen, W.-J. Ong, X. Zhao and N. Li, *Chem*, 2019, **5**, 18–50.

98 B. Wang, M. Y. Wang, F. Y. Liu, Q. Zhang, S. Yao, X. L. Liu and F. Huang, *Angew. Chem., Int. Ed.*, 2020, **59**, 1914–1918.

99 S. Cao, B. Shen, T. Tong, J. Fu and J. Yu, *Adv. Funct. Mater.*, 2018, **28**, 1800136.

100 H. Wang, Y. Wu, T. Xiao, X. Yuan, G. Zeng, W. Tu, S. Wu, H. Y. Lee, Y. Z. Tan and J. W. Chew, *Appl. Catal., B*, 2018, **233**, 213–225.

101 T. Su, R. Peng, Z. D. Hood, M. Naguib, I. N. Ivanov, J. K. Keum, Z. Qin, Z. Guo and Z. Wu, *ChemSusChem*, 2018, **11**, 688–699.

102 M. Ye, X. Wang, E. Liu, J. Ye and D. Wang, *ChemSusChem*, 2018, **11**, 1606–1611.

103 X. Xie, N. Zhang, Z.-R. Tang, M. Anpo and Y.-J. Xu, *Appl. Catal., B*, 2018, **237**, 43–49.

104 W. Feitknecht and M. Gerber, *Helv. Chim. Acta*, 1942, **25**, 131–137.

105 W. v. Feitknecht, *Helv. Chim. Acta*, 1942, **25**, 555–569.

106 X. Zhao, C. Niu, L. Zhang, H. Guo, X. Wen, C. Liang and G. Zeng, *Chemosphere*, 2018, **204**, 11–21.

107 Y. Zhu, R. Zhu, M. Wang, B. Wu, X. He, Y. Qian and S. Wang, *Adv. Sci.*, 2016, **3**, 1600229.

108 M. I. Agnel, S. Grangeon, F. Fauth, E. Elkaïm, F. Claret, M. Roulet, F. Warmont and C. Tournassat, *Environ. Sci. Technol.*, 2020, **54**, 851–861.

109 X. Zhang, L. Yan, J. Li and H. Yu, *J. Colloid Interface Sci.*, 2020, **562**, 149–158.

This journal is © The Royal Society of Chemistry 2020

J. Mater. Chem. A, 2020, **8**, 19156–19195 | **19191**

110 B. Song, Z. Zeng, G. Zeng, J. Gong, R. Xiao, S. Ye, M. Chen, C. Lai, P. Xu and X. Tang, *Adv. Colloid Interface Sci.*, 2019, **272**, 101999.

111 L. Lv, Z. Yang, K. Chen, C. Wang and Y. Xiong, *Adv. Energy Mater.*, 2019, **9**, 1803358.

112 L. Mohapatra and K. Parida, *J. Mater. Chem. A*, 2016, **4**, 10744–10766.

113 S. P. Paredes, M. A. Valenzuela, G. Fetter and S. O. Flores, *J. Phys. Chem. Solids*, 2011, **72**, 914–919.

114 Z.-z. Yang, J.-j. Wei, G.-m. Zeng, H.-q. Zhang, X.-f. Tan, C. Ma, X.-c. Li, Z.-h. Li and C. Zhang, *Coord. Chem. Rev.*, 2019, **386**, 154–182.

115 N. Ahmed, Y. Shibata, T. Taniguchi and Y. Izumi, *J. Catal.*, 2011, **279**, 123–135.

116 K. Wang, L. Zhang, Y. Su, D. Shao, S. Zeng and W. Wang, *J. Mater. Chem. A*, 2018, **6**, 8366–8373.

117 T.-T. Kong, J. Huang, X.-G. Jia, W.-Z. Wang and Y. Zhou, *Sci. Rep.*, 2019, **9**, 5659.

118 X. Xiong, Y. Zhao, R. Shi, W. Yin, Y. Zhao, G. I. N. Waterhouse and T. Zhang, *Sci. Bull.*, 2020, **65**, 987–994.

119 L. A. Wein, H. Zhang, K. Urushidate, M. Miyano and Y. Izumi, *Appl. Surf. Sci.*, 2018, **447**, 687–696.

120 L. Lei, D. Huang, C. Zhou, S. Chen, X. Yan, Z. Li and W. Wang, *Coord. Chem. Rev.*, 2020, **408**, 213177.

121 Y. Zhao, G. Chen, T. Bian, C. Zhou, G. I. N. Waterhouse, L.-Z. Wu, C.-H. Tung, L. J. Smith, D. O'Hare and T. Zhang, *Adv. Mater.*, 2015, **27**, 7824–7831.

122 H. Jiang, K.-i. Katsumata, J. Hong, A. Yamaguchi, K. Nakata, C. Terashima, N. Matsushita, M. Miyauchi and A. Fujishima, *Appl. Catal., B*, 2018, **224**, 783–790.

123 G. Gao, Z. Zhu, J. Zheng, Z. Liu, Q. Wang and Y. Yan, *J. Colloid Interface Sci.*, 2019, **555**, 1–10.

124 M. M.-J. Li, C. Chen, T. c. e. Ayvalı, H. Suo, J. Zheng, I. F. Teixeira, L. Ye, H. Zou, D. O'Hare and S. C. E. Tsang, *ACS Catal.*, 2018, **8**, 4390–4401.

125 G. Chen, R. Gao, Y. Zhao, Z. Li, G. I. Waterhouse, R. Shi, J. Zhao, M. Zhang, L. Shang, G. Sheng, X. Zhang, X. Wen, L. Z. Wu, C. H. Tung and T. Zhang, *Adv. Mater.*, 2018, **30**, 1704663.

126 Z. Wang, S.-M. Xu, L. Tan, G. Liu, T. Shen, C. Yu, H. Wang, Y. Tao, X. Cao, Y. Zhao and Y.-F. Song, *Appl. Catal., B*, 2020, **270**, 118884.

127 Q. Yun, L. Li, Z. Hu, Q. Lu, B. Chen and H. Zhang, *Adv. Mater.*, 2019, **32**, 1903826.

128 X. Chia and M. Pumera, *Chem. Soc. Rev.*, 2018, **47**, 5602–5613.

129 X. Zhang, Z. Lai, Q. Ma and H. Zhang, *Chem. Soc. Rev.*, 2018, **47**, 3301–3338.

130 R. Geioushy, S. El-Sheikh, I. Hegazy, A. Shawky, S. El-Sherbiny and A.-H. T. Kandil, *Mater. Res. Bull.*, 2019, **118**, 110499.

131 R. Wang, Y. Yu, S. Zhou, H. Li, H. Wong, Z. Luo, L. Gan and T. Zhai, *Adv. Funct. Mater.*, 2018, **28**, 1802473.

132 Z. Xia, Y. Tao, Z. Pan and X. Shen, *Results Phys.*, 2019, **12**, 2218–2224.

133 D. Huang, L. Lei, R. Deng, S. Chen, Z. Li, C. Zhang, W. Wang and K. Wang, *J. Catal.*, 2020, **381**, 175–185.

134 L. Lei, D. Huang, G. Zeng, M. Cheng, D. Jiang, C. Zhou, S. Chen and W. Wang, *Coord. Chem. Rev.*, 2019, **399**, 213020.

135 Y. Li, J. Shi, Y. Mi, X. Sui, H. Xu and X. Liu, *J. Mater. Chem. C*, 2019, **7**, 4304–4319.

136 F. Xu, B. Zhu, B. Cheng, J. Yu and J. Xu, *Adv. Opt. Mater.*, 2018, **6**, 1800911.

137 W. Tu, Y. Li, L. Kuai, Y. Zhou, Q. Xu, H. Li, X. Wang, M. Xiao and Z. Zou, *Nanoscale*, 2017, **9**, 9065–9070.

138 H. Jung, K. M. Cho, K. H. Kim, H.-W. Yoo, A. Al-Saggaf, I. Gereige and H.-T. Jung, *ACS Sustainable Chem. Eng.*, 2018, **6**, 5718–5724.

139 L. Zhang, H. Zhang, C. Jiang, J. Yuan, X. Huang, P. Liu and W. Feng, *Appl. Catal., B*, 2019, **259**, 118073.

140 J. Huang, J. Mei, J. Han, H. Liang, W. Wang, B. Dong and L. Cao, *J. Colloid Interface Sci.*, 2019, **556**, 224–231.

141 M. Guo, Z. Xing, T. Zhao, Z. Li, S. Yang and W. Zhou, *Appl. Catal., B*, 2019, **257**, 117913.

142 M. R. U. D. Biswas, A. Ali, K. Y. Cho and W.-C. Oh, *Ultrason. Sonochem.*, 2018, **42**, 738–746.

143 J. R. Dunklin, H. Zhang, Y. Yang, J. Liu and J. van de Lagemaat, *ACS Energy Lett.*, 2018, **3**, 2223–2229.

144 S. Li, Z. Zhao, D. Yu, J.-Z. Zhao, J.-Y. Su, Y. Liu, Y. Lin, W. Liu, H. Xu and Z. Zhang, *Nano Energy*, 2019, **66**, 104083.

145 Y. Lin, D. Han, Y. Li, L. Tan, X. Liu, Z. Cui, X. Yang, Z. Li, Y. Liang and S. Zhu, *ACS Sustainable Chem. Eng.*, 2019, **7**, 14982–14990.

146 R. Kumar, D. Das and A. K. Singh, *J. Catal.*, 2018, **359**, 143–150.

147 M. Wang, J. Ioccozia, L. Sun, C. Lin and Z. Lin, *Energy Environ. Sci.*, 2014, **7**, 2182–2202.

148 J. Liu, P. Wang, W. Qu, H. Li, L. Shi and D. Zhang, *Appl. Catal., B*, 2019, **257**, 117880.

149 J. Wang, Y. Zhang, X. Wang and W. Su, *Appl. Catal., B*, 2019, **268**, 118444.

150 S. Qamar, F. Lei, L. Liang, S. Gao, K. Liu, Y. Sun, W. Ni and Y. Xie, *Nano Energy*, 2016, **26**, 692–698.

151 L. Wei, C. Yu, Q. Zhang, H. Liu and Y. Wang, *J. Mater. Chem. A*, 2018, **6**, 22411–22436.

152 Z. Jiang, W. Miao, X. Zhu, G. Yang, Z. Yuan, J. Chen, X. Ji, F. Kong and B. Huang, *Appl. Catal., B*, 2019, **256**, 117881.

153 Y. Zhao, N. Liu, S. Zhou and J. Zhao, *J. Mater. Chem. A*, 2019, **7**, 16294–16303.

154 H. Wang, Z. Zeng, P. Xu, L. Li, G. Zeng, R. Xiao, Z. Tang, D. Huang, L. Tang and C. Lai, *Chem. Soc. Rev.*, 2019, **48**, 488–516.

155 H. Luo, Z. Zeng, G. Zeng, C. Zhang, R. Xiao, D. Huang, C. Lai, M. Cheng, W. Wang, W. Xiong, Y. Yang, L. Qin, C. Zhou, H. Wang, Y. Zhou and S. Tian, *Chem. Eng. J.*, 2020, **383**, 123196.

156 R. Li, W. Zhang and K. Zhou, *Adv. Mater.*, 2018, **30**, 1705512.

157 I. I. Alkhatib, C. Garlisi, M. Pagliaro, K. Al-Ali and G. Palmisano, *Catal. Today*, 2020, **340**, 209–224.

19192 | *J. Mater. Chem. A*, 2020, **8**, 19156–19195

This journal is © The Royal Society of Chemistry 2020

158 S. Tian, C. Zhang, D. Huang, R. Wang, G. Zeng, M. Yan, W. Xiong, C. Zhou, M. Cheng and W. Xue, *Chem. Eng. J.*, 2020, **389**, 123423.

159 L. Ye, Y. Gao, S. Cao, H. Chen, Y. Yao, J. Hou and L. Sun, *Appl. Catal., B*, 2018, **227**, 54–60.

160 C. Zheng, X. Qiu, J. Han, Y. Wu and S. Liu, *ACS Appl. Mater. Interfaces*, 2019, **11**, 42243–42249.

161 Y. Yang, C. Zhang, C. Lai, G. Zeng, D. Huang, M. Cheng, J. Wang, F. Chen, C. Zhou and W. Xiong, *Adv. Colloid Interface Sci.*, 2018, **254**, 76–93.

162 L. Ye, X. Jin, X. Ji, C. Liu, Y. Su, H. Xie and C. Liu, *Chem. Eng. J.*, 2016, **291**, 39–46.

163 J.-y. Zhu, Y.-p. Li, X.-j. Wang, J. Zhao, Y.-s. Wu and F.-t. Li, *ACS Sustainable Chem. Eng.*, 2019, **7**, 14953–14961.

164 Y. Bai, P. Yang, L. Wang, B. Yang, H. Xie, Y. Zhou and L. Ye, *Chem. Eng. J.*, 2019, **360**, 473–482.

165 Q. Wang, K. Wang, L. Zhang, H. Wang and W. Wang, *Appl. Surf. Sci.*, 2019, **470**, 832–839.

166 X. Wang, K. Maeda, A. Thomas, K. Takanabe, G. Xin, J. M. Carlsson, K. Domen and M. Antonietti, *Nat. Mater.*, 2009, **8**, 76.

167 W. Wang, C. Zhou, Y. Yang, G. Zeng, C. Zhang, Y. Zhou, J. Yang, D. Huang, H. Wang, W. Xiong, X. Li, Y. Fu, Z. Wang, Q. He, M. Jia and H. Luo, *Chem. Eng. J.*, 2021, **404**, 126540.

168 Y. Yang, G. Zeng, D. Huang, C. Zhang, D. He, C. Zhou, W. Wang, W. Xiong, X. Li, B. Li, W. Dong and Y. Zhou, *Appl. Catal., B*, 2020, **272**, 118970.

169 Y. Yang, X. Li, C. Zhou, W. Xiong, G. Zeng, D. Huang, C. Zhang, W. Wang, B. Song, X. Tang, X. Li and H. Guo, *Water Res.*, 2020, **184**, 116200.

170 C. Zhang, Y. Zhou, W. Wang, Y. Yang, C. Zhou, L. Wang, L. Lei, D. He, H. Luo and D. Huang, *Appl. Surf. Sci.*, 2020, **527**, 146757.

171 S. N. Talapaneni, G. Singh, I. Y. Kim, K. AlBahily, A. a. H. Al-Muhtaseb, A. S. Karakoti, E. Tavakkoli and A. Vinu, *Adv. Mater.*, 2020, **32**, 1904635.

172 D. He, C. Zhang, G. Zeng, Y. Yang, D. Huang, L. Wang and H. Wang, *Appl. Catal., B*, 2019, **258**, 117957.

173 Y. Yang, C. Zhang, D. Huang, G. Zeng, J. Huang, C. Lai, C. Zhou, W. Wang, H. Guo and W. Xue, *Appl. Catal., B*, 2019, **245**, 87–99.

174 J. Fu, J. Yu, C. Jiang and B. Cheng, *Adv. Energy Mater.*, 2018, **8**, 1701503.

175 G. Dong and L. Zhang, *J. Mater. Chem.*, 2012, **22**, 1160–1166.

176 W. Wang, P. Xu, M. Chen, G. Zeng, C. Zhang, C. Zhou, Y. Yang, D. Huang, C. Lai and M. Cheng, *ACS Sustainable Chem. Eng.*, 2018, **6**, 15503–15516.

177 S. Tang, X. Yin, G. Wang, X. Lu and T. Lu, *Nano Res.*, 2019, **12**, 457–462.

178 P. Huang, J. Huang, S. A. Pantovich, A. D. Carl, T. G. Fenton, C. A. Caputo, R. L. Grimm, A. I. Frenkel and G. Li, *J. Am. Chem. Soc.*, 2018, **140**, 16042–16047.

179 Z. Mo, X. Zhu, Z. Jiang, Y. Song, D. Liu, H. Li, X. Yang, Y. She, Y. Lei and S. Yuan, *Appl. Catal., B*, 2019, **256**, 117854.

180 Y. Li, J. Ren, S. Ouyang, W. Hou, T. Petit, H. Song, H. Chen, D. Philo, T. Kako and J. Ye, *Appl. Catal., B*, 2019, **259**, 118027.

181 F. Lin, Y. Zihao and X. Wang, *Chem. Commun.*, 2019, **55**, 8235–8237.

182 J. Fu, K. Liu, K. Jiang, H. Li, P. An, W. Li, N. Zhang, H. Li, X. Xu and H. Zhou, *Adv. Sci.*, 2019, **6**, 1900796.

183 S. Samanta, R. Yadav, A. Kumar, A. K. Sinha and R. Srivastava, *Appl. Catal., B*, 2019, **259**, 118054.

184 J. Wu, Y. Feng, D. Li, X. Han and J. Liu, *Energy*, 2019, **178**, 168–175.

185 A. Bafaqeer, M. Tahir and N. A. S. Amin, *Appl. Catal., B*, 2019, **242**, 312–326.

186 A. Hayat, J. Khan, M. U. Rahman, S. B. Mane, W. U. Khan, M. Sohail, N. U. Rahman, N. Shaishta, Z. Chi and M. Wu, *J. Colloid Interface Sci.*, 2019, **548**, 197–205.

187 C. Zhang, W. Wang, A. Duan, G. Zeng, D. Huang, C. Lai, X. Tan, M. Cheng, R. Wang, C. Zhou, W. Xiong and Y. Yang, *Chemosphere*, 2019, **222**, 184–194.

188 C. Han, N. Zhang and Y.-J. Xu, *Nano Today*, 2016, **11**, 351–372.

189 X. Gong, G. Liu, Y. Li, D. Y. W. Yu and W. Y. Teoh, *Chem. Mater.*, 2016, **28**, 8082–8118.

190 J. Yu, H. Feng, L. Tang, Y. Pang, G. Zeng, Y. Lu, H. Dong, J. Wang, Y. Liu and C. Feng, *Prog. Mater. Sci.*, 2020, **111**, 100654.

191 S. Sajjad, S. A. Khan Leghari and A. Iqbal, *ACS Appl. Mater. Interfaces*, 2017, **9**, 43393–43414.

192 T.-F. Yeh, J. Cihlář, C.-Y. Chang, C. Cheng and H. Teng, *Mater. Today*, 2013, **16**, 78–84.

193 Y. Zhu, S. Murali, W. Cai, X. Li, J. W. Suk, J. R. Potts and R. S. Ruoff, *Adv. Mater.*, 2010, **22**, 3906–3924.

194 Y. Liu, B. Sajjadi, W.-Y. Chen and R. Chatterjee, *Fuel*, 2019, **247**, 10–18.

195 C. Bie, B. Zhu, F. Xu, L. Zhang and J. Yu, *Adv. Mater.*, 2019, **31**, 1902868.

196 J. Cai, J. Chen, P. Zeng, Z. Pang and X. Kong, *Chem. Mater.*, 2019, **31**, 3729–3735.

197 S.-H. Liu, J.-S. Lu, Y.-C. Pu and H.-C. Fan, *J. CO₂ Util.*, 2019, **33**, 171–178.

198 J. Meng, Q. Chen, J. Lu and H. Liu, *ACS Appl. Mater. Interfaces*, 2018, **11**, 550–562.

199 X. Wang, Q. Li, C. Zhou, Z. Cao and R. Zhang, *J. Colloid Interface Sci.*, 2019, **554**, 335–343.

200 Y. Zhao, Y. Wei, X. Wu, H. Zheng, Z. Zhao, J. Liu and J. Li, *Appl. Catal., B*, 2018, **226**, 360–372.

201 Y. Tang, X. Hu and C. Liu, *Phys. Chem. Chem. Phys.*, 2014, **16**, 25321–25329.

202 M. Xu, X. Hu, S. Wang, J. Yu, D. Zhu and J. Wang, *J. Catal.*, 2019, **377**, 652–661.

203 D. V. Shtansky, K. L. Firestein and D. V. Golberg, *Nanoscale*, 2018, **10**, 17477–17493.

204 C. Zhou, C. Lai, C. Zhang, G. Zeng, D. Huang, M. Cheng, L. Hu, W. Xiong, M. Chen and J. Wang, *Appl. Catal., B*, 2018, **238**, 6–18.

205 G. Zhao, A. Wang, W. He, Y. Xing and X. Xu, *Adv. Mater. Interfaces*, 2019, **6**, 1900062.

This journal is © The Royal Society of Chemistry 2020

J. Mater. Chem. A, 2020, **8**, 19156–19195 | **19193**

206 S. Chen, P. Li, S. Xu, X. Pan, Q. Fu and X. Bao, *J. Mater. Chem. A*, 2018, **6**, 1832–1839.

207 W. Wang, Q. Niu, G. Zeng, C. Zhang, D. Huang, B. Shao, C. Zhou, Y. Yang, Y. Liu, H. Guo, W. Xiong, L. Lei, S. Liu, H. Yi, S. Chen and X. Tang, *Appl. Catal., B*, 2020, **273**, 119051.

208 V. Tran, R. Soklaski, Y. Liang and L. Yang, *Phys. Rev. B*, 2014, **89**, 235319.

209 B. Li, C. Lai, G. Zeng, D. Huang, L. Qin, M. Zhang, M. Cheng, X. Liu, H. Yi, C. Zhou, F. Huang, S. Liu and Y. Fu, *Small*, 2019, **15**, 1804565.

210 H. U. Lee, S. C. Lee, J. Won, B.-C. Son, S. Choi, Y. Kim, S. Y. Park, H.-S. Kim, Y.-C. Lee and J. Lee, *Sci. Rep.*, 2015, **5**, 8691.

211 Q. Zhang, S. Huang, J. Deng, D. T. Gangadharan, F. Yang, Z. Xu, G. Giorgi, M. Palummo, M. Chaker and D. Ma, *Adv. Funct. Mater.*, 2019, **29**, 1902486.

212 Q. Li, Q. Zhou, L. Shi, Q. Chen and J. Wang, *J. Mater. Chem. A*, 2019, **7**, 4291–4312.

213 G. Zhou, J. Yang, X. Zhu, Q. Li, Q. Yu, W. El-alami, C. Wang, Y. She, J. Qian, H. Xu and H. Li, *J. Energy Chem.*, 2020, **49**, 89–95.

214 J. Li, P. Liu, H. Huang, Y. Li, Y. Tang, D. Mei and C. Zhong, *ACS Sustainable Chem. Eng.*, 2020, **8**, 5175–5183.

215 X. Wang, J. He, J. Li, G. Lu, F. Dong, T. Majima and M. Zhu, *Appl. Catal., B*, 2020, **277**, 119230.

216 X. Zhu, S. Huang, Q. Yu, Y. She, J. Yang, G. Zhou, Q. Li, X. She, J. Deng, H. Li and H. Xu, *Appl. Catal., B*, 2020, **269**, 118760.

217 J. Low, L. Zhang, T. Tong, B. Shen and J. Yu, *J. Catal.*, 2018, **361**, 255–266.

218 S. Iguchi, Y. Hasegawa, K. Teramura, S. Kidera, S. Kikkawa, S. Hosokawa, H. Asakura and T. Tanaka, *Sustainable Energy Fuels*, 2017, **1**, 1740–1747.

219 Y. Yang, J. Wu, T. Xiao, Z. Tang, J. Shen, H. Li, Y. Zhou and Z. Zou, *Appl. Catal., B*, 2019, **255**, 117771.

220 S. Kumar, M. A. Isaacs, R. Trofimovaite, L. Durndell, C. M. Parlett, R. E. Douthwaite, B. Coulson, M. C. Cockett, K. Wilson and A. F. Lee, *Appl. Catal., B*, 2017, **209**, 394–404.

221 S. Tonda, S. Kumar, M. Bhardwaj, P. Yadav and S. Ogale, *ACS Appl. Mater. Interfaces*, 2018, **10**, 2667–2678.

222 Y. Wang, Z. Zhang, L. Zhang, Z. Luo, J. Shen, H. Lin, J. Long, J. C. Wu, X. Fu and X. Wang, *J. Am. Chem. Soc.*, 2018, **140**, 14595–14598.

223 W. Dai, J. Yu, Y. Deng, X. Hu, T. Wang and X. Luo, *Appl. Surf. Sci.*, 2017, **403**, 230–239.

224 H. Shi, S. Long, S. Hu, J. Hou, W. Ni, C. Song, K. Li, G. G. Gurzadyan and X. Guo, *Appl. Catal., B*, 2019, **245**, 760–769.

225 H. Shi, S. Long, J. Hou, L. Ye, Y. Sun, W. Ni, C. Song, K. Li, G. G. Gurzadyan and X. Guo, *Chem.–Eur. J.*, 2019, **25**, 5028–5035.

226 W.-K. Jo, S. Kumar and S. Tonda, *Composites, Part B*, 2019, **176**, 107212.

227 H. Guo, M. Chen, Q. Zhong, Y. Wang, W. Ma and J. Ding, *J. CO₂ Util.*, 2019, **33**, 233–241.

228 N. Ojha, A. Bajpai and S. Kumar, *Catal. Sci. Technol.*, 2019, **9**, 4598–4613.

229 J. Zhou, H. Wu, C.-Y. Sun, C.-Y. Hu, X.-L. Wang, Z.-H. Kang and Z.-M. Su, *J. Mater. Chem. A*, 2018, **6**, 21596–21604.

230 P. Seeharaj, P. Kongmun, P. Paiplod, S. Prakobmit, C. Sriwong, P. Kim-Lohsoontorn and N. Vittayakorn, *Ultrason. Sonochem.*, 2019, **58**, 104657.

231 A. Kumar, G. Sharma, M. Naushad, T. Ahamad, R. C. Veses and F. J. Stadler, *Chem. Eng. J.*, 2019, **370**, 148–165.

232 J. O. Olowoyo, M. Kumar, B. Singh, V. O. Oninla, J. O. Babalola, H. Valdés, A. V. Vorontsov and U. Kumar, *Carbon*, 2019, **147**, 385–397.

233 N. Sadeghi, S. Sharifnia and T.-O. Do, *J. Mater. Chem. A*, 2018, **6**, 18031–18035.

234 Y. Liang, W. Wu, P. Wang, S.-C. Liou, D. Liu and S. H. Ehrman, *Nano Res.*, 2018, **11**, 4049–4061.

235 D. Mateo, J. Albero and H. García, *Appl. Catal., B*, 2018, **224**, 563–571.

236 D. Mateo, J. Albero and H. García, *Energy Environ. Sci.*, 2017, **10**, 2392–2400.

237 J. M. Thomas, R. Raja and D. W. Lewis, *Angew. Chem., Int. Ed.*, 2005, **44**, 6456–6482.

238 B. Qiao, A. Wang, X. Yang, L. F. Allard, Z. Jiang, Y. Cui, J. Liu, J. Li and T. Zhang, *Nat. Chem.*, 2011, **3**, 634.

239 Y. Yang, G. Zeng, D. Huang, C. Zhang, D. He, C. Zhou, W. Wang, W. Xiong, B. Song, H. Yi, S. Ye and X. Ren, *Small*, 2020, **16**, 2001634.

240 S. Ding, M. J. Hülsey, J. Pérez-Ramírez and N. Yan, *Joule*, 2019, **3**, 2897–2929.

241 J. Di, C. Chen, S.-Z. Yang, S. Chen, M. Duan, J. Xiong, C. Zhu, R. Long, W. Hao and Z. Chi, *Nat. Commun.*, 2019, **10**, 1–7.

242 Y. Wang, J. Mao, X. Meng, L. Yu, D. Deng and X. Bao, *Chem. Rev.*, 2018, **119**, 1806–1854.

243 T. Tong, B. Zhu, C. Jiang, B. Cheng and J. Yu, *Appl. Surf. Sci.*, 2018, **433**, 1175–1183.

244 C. Gao, S. Chen, Y. Wang, J. Wang, X. Zheng, J. Zhu, L. Song, W. Zhang and Y. Xiong, *Adv. Mater.*, 2018, **30**, 1704624.

245 P. Zhou, Y. Chao, F. Lv, J. Lai, K. Wang and S. Guo, *Sci. Bull.*, 2020, **65**, 720–725.

246 J. Di, C. Chen, S.-Z. Yang, S. Chen, M. Duan, J. Xiong, C. Zhu, R. Long, W. Hao, Z. Chi, H. Chen, Y.-X. Weng, J. Xia, L. Song, S. Li, H. Li and Z. Liu, *Nat. Commun.*, 2019, **10**, 2840.

247 L. Shi, X. Ren, Q. Wang, Y. Li, F. Ichihara, H. Zhang, Y. Izumi, L. Ren, W. Zhou, Y. Yang and J. Ye, *Small*, 2020, 2002356, DOI: 10.1002/smll.202002356.

248 R. Zhang, P. Li, F. Wang, L. Ye, A. Gaur, Z. Huang, Z. Zhao, Y. Bai and Y. Zhou, *Appl. Catal., B*, 2019, **250**, 273–279.

249 K. Homlamai, T. Maihom, S. Choomwattana, M. Sawangphruk and J. Limtrakul, *Appl. Surf. Sci.*, 2020, **499**, 143928.

250 C. Liu, B. Yang, E. Tyo, S. Seifert, J. DeBartolo, B. von Issendorff, P. Zapol, S. Vajda and L. A. Curtiss, *J. Am. Chem. Soc.*, 2015, **137**, 8676–8679.

19194 | *J. Mater. Chem. A*, 2020, **8**, 19156–19195

This journal is © The Royal Society of Chemistry 2020

251 G. Gao, Y. Jiao, E. R. Waclawik and A. Du, *J. Am. Chem. Soc.*, 2016, **138**, 6292–6297.

252 H. Zhang, J. Wei, J. Dong, G. Liu, L. Shi, P. An, G. Zhao, J. Kong, X. Wang and X. Meng, *Angew. Chem., Int. Ed.*, 2016, **55**, 14310–14314.

253 M. Wang, J. Liu, C. Guo, J. Gao, C. Gong, Y. Wang, B. Liu, X. Li, G. G. Gurzadyan and L. Sun, *J. Mater. Chem. A*, 2018, **6**, 4768–4775.

254 W. Shi, X. Guo, C. Cui, K. Jiang, Z. Li, L. Qu and J.-C. Wang, *Appl. Catal., B*, 2019, **243**, 236–242.

255 W. Tu, Y. Xu, J. Wang, B. Zhang, T. Zhou, S. Yin, S. Wu, C. Li, Y. Huang and Y. Zhou, *ACS Sustainable Chem. Eng.*, 2017, **5**, 7260–7268.

256 J. Di, C. Chen, C. Zhu, P. Song, J. Xiong, M. Ji, J. Zhou, Q. Fu, M. Xu and W. Hao, *ACS Appl. Mater. Interfaces*, 2019, **11**, 30786–30792.

257 M. Tahir, B. Tahir, M. Nawawi, M. Hussain and A. Muhammad, *Appl. Surf. Sci.*, 2019, **485**, 450–461.

258 Y. Xu, F. Ge, Z. Chen, S. Huang, W. Wei, M. Xie, H. Xu and H. Li, *Appl. Surf. Sci.*, 2019, **469**, 739–746.

259 A. Tabib, W. Bouslama, B. Sieber, A. Addad, H. Elhouichet, M. Férid and R. Boukherroub, *Appl. Surf. Sci.*, 2017, **396**, 1528–1538.

260 Y. Wang, S. Zhao, Y. Zhang, J. Fang, Y. Zhou, S. Yuan, C. Zhang and W. Chen, *Appl. Surf. Sci.*, 2018, **440**, 258–265.

261 T. He, C. Zhang, L. Zhang and A. Du, *Nano Res.*, 2019, **12**, 1817–1823.

262 Y. Zheng, J. Dong, C. Huang, L. Xia, Q. Wu, Q. Xu and W. Yao, *Appl. Catal., B*, 2020, **260**, 118220.

263 C. Zhang, C. Lai, G. Zeng, D. Huang, L. Tang, C. Yang, Y. Zhou, L. Qin and M. Cheng, *Biosens. Bioelectron.*, 2016, **81**, 61–67.

264 M. Sun, B. Lei, J. Li, P. Chen, Y. Zhang and F. Dong, *Nanoscale*, 2019, **11**, 20562–20570.

265 F. Li, P. Zhu, S. Wang, X. Xu, Z. Zhou and C. Wu, *RSC Adv.*, 2019, **9**, 20633–20642.

266 C. Yu, H. He, Q. Fan, W. Xie, Z. Liu and H. Ji, *Sci. Total Environ.*, 2019, **694**, 133727.

267 C. Feng, L. Tang, Y. Deng, G. Zeng, J. Wang, Y. Liu, Z. Chen, J. Yu and J. Wang, *Appl. Catal., B*, 2019, **256**, 117827.

268 C. Bie, B. Zhu, F. Xu, L. Zhang and J. Yu, *Adv. Mater.*, 2019, **31**, 1902868.

269 W. Wang, Z. Zeng, G. Zeng, C. Zhang, R. Xiao, C. Zhou, W. Xiong, Y. Yang, L. Lei and Y. Liu, *Chem. Eng. J.*, 2019, **378**, 122132.

270 J. Li, P. Yan, K. Li, J. You, H. Wang, W. Cui, W. Cen, Y. Chu and F. Dong, *J. Mater. Chem. A*, 2019, **7**, 17014–17021.

271 D. Tan, J. Zhang, J. Shi, S. Li, B. Zhang, X. Tan, F. Zhang, L. Liu, D. Shao and B. Han, *ACS Appl. Mater. Interfaces*, 2018, **10**, 24516–24522.

272 C. Huang, C. Chen, M. Zhang, L. Lin, X. Ye, S. Lin, M. Antonietti and X. Wang, *Nat. Commun.*, 2015, **6**, 7698.

273 W. Che, W. Cheng, T. Yao, F. Tang, W. Liu, H. Su, Y. Huang, Q. Liu, J. Liu and F. Hu, *J. Am. Chem. Soc.*, 2017, **139**, 3021–3026.

274 Y. Huang, D. Li, Z. Fang, R. Chen, B. Luo and W. Shi, *Appl. Catal., B*, 2019, **254**, 128–134.

275 K. Wang, J. Fu and Y. Zheng, *Appl. Catal., B*, 2019, **254**, 270–282.

276 A. J. Meier, A. Garg, B. Sutter, J. N. Kuhn and V. R. Bhethanabotla, *ACS Sustainable Chem. Eng.*, 2018, **7**, 265–275.

277 W. Shi, F. Guo, H. Wang, M. Han, H. Li, S. Yuan, H. Huang, Y. Liu and Z. Kang, *Appl. Catal., B*, 2017, **219**, 36–44.

278 A. A. Umar, E. Rahmi, A. Balouch, M. Y. A. Rahman, M. M. Salleh and M. Oyama, *J. Mater. Chem. A*, 2014, **2**, 17655–17665.

279 S. Liu, J. Yu and M. Jaroniec, *Chem. Mater.*, 2011, **23**, 4085–4093.

280 N. Zhang, C. Gao and Y. Xiong, *J. Energy Chem.*, 2019, **37**, 43–57.

281 M. Shen, L. Zhang, M. Wang, J. Tian, X. Jin, L. Guo, L. Wang and J. Shi, *J. Mater. Chem. A*, 2019, **7**, 1556–1563.

282 J. Xiong, J. Di, J. Xia, W. Zhu and H. Li, *Adv. Funct. Mater.*, 2018, **28**, 1801983.

283 J. Di, X. Zhao, C. Lian, M. Ji, J. Xia, J. Xiong, W. Zhou, X. Cao, Y. She and H. Liu, *Nano Energy*, 2019, **61**, 54–59.

284 J. Low, J. Yu, M. Jaroniec, S. Wageh and A. A. Al-Ghamdi, *Adv. Mater.*, 2017, **29**, 1601694.

285 Z. Kong, X. Chen, W.-J. Ong, X. Zhao and N. Li, *Appl. Surf. Sci.*, 2019, **463**, 1148–1153.

286 W.-K. Jo, S. Kumar, S. Eslava and S. Tonda, *Appl. Catal., B*, 2018, **239**, 586–598.

287 J. Sun, H. Zhang, L.-H. Guo and L. Zhao, *ACS Appl. Mater. Interfaces*, 2013, **5**, 13035–13041.

This journal is © The Royal Society of Chemistry 2020

J. Mater. Chem. A, 2020, **8**, 19156–19195 | **19195**